Characterization of aniridia in Pax6-deficient mouse retinas

James Cole
Roanoke, Virginia

B.S., College of William and Mary, 2018

A Dissertation presented to the Graduate Faculty of the University of Virginia in Candidacy for the Degree of Doctor of Philosophy
Neuroscience Graduate Program

University of Virginia
June, 2023

Abstract

Aniridia is a panocular eye disorder associated with heterozygous mutations in the homeobox gene *PAX6*. Characterized by a complete or partial loss of the iris, aniridia is also known to cause many deleterious phenotypes of varying severity, including corneal keratopathy, lens hypoplasia, nystagmus, and cataracts. While most previous investigations have focused on the anterior eye segment, aniridia is also known to disrupt normal retinal development, an area we explore in the following chapters.

Our first chapter describes the relationship between glaucoma, aniridia, and the ongoing challenges facing clinicians and researchers. As retinal deficits represent the most critical impairments to vision, it is important to establish how Pax6-deficiencies disrupt normal retinal formation and how these disruptions are exacerbated in post-natal development.

Chapter 2 discusses our own investigations into the long-term effects of a potential aniridia treatment, the MEK-inhibitor PD0325901. Using a Pax6-deficient *small-eye* mouse model ($Pax6^{Sey\text{-}Neu/+}$) we found a wide-ranging combination of morphological damage and visual impairments in aniridic retinas. Measurements of intraocular pressure (IOP) indicated a glaucomatous phenotype which correlated with a decreased visual acuity in afflicted mice. *Ex vivo* assessments of $Pax6^{Sey\text{-}Neu/+}$ retinas found increased incidence of localized damage we termed “hotspots,” and disruption of retinal ganglion cell (RGC) axon bundles. All these deficits were at least partially mitigated in $Pax6^{Sey\text{-}Neu/+}$ mice treated with PD0325901, suggesting that Pax6-dosage compensation moderately protected against aniridia phenotypes.

Our subsequent studies in Chapter 3 used $Pax6^{Sey}$ mouse models from the C57Bl/6 and 129S/Svlmj backgrounds to demonstrate how IOP and visual acuity decline in aniridic mice in an age-dependent manner. Further studies of retinal of these mice found highly varying retinal

thicknesses and retinal subtype densities in these hotspots. Most interesting, however, was the increased recruitment and activation of microglia and astrocytes in *Pax6*^{Sey} retinas, which suggests a tissue-wide neuroinflammatory response to aniridia.

In Chapter 4, we further discuss the pathogenesis of aniridia, including the disease's relationship to *PAX6* and how disruption of critical developmental pathways leads to tissue hypoplasia. Likewise, we explore the various murine models used to study Pax6-deficiencies, their benefits and complications, and how these models contribute to translational research. We also review the possible causes of retinal damage, and how this damage is reflected in tissue morphology and functional assessments. Finally, we interrogate the current methods for diagnosing, tracking, and treating aniridia, especially the ongoing work in pharmacological interventions, including the dosage-compensation mechanisms we describe in Chapter 2, and some novel formulations of the mutation suppressant ataluren. Collectively, these findings provide the basis for a viable, case-specific approach for study which will better address the highly varied phenotypes of aniridia patients.

Acknowledgements

No endeavor of any academic merit can come to fruition without the aid and input of many esteemed mentors. It may take a village to raise a child, but it takes several departments' worth of academics to foster a new doctoral candidate. If I were to list every person who has helped me along the way I might challenge the limits of my word count, so I will indulge concision instead.

I would first like to thank my supervisor and principal investigator, Dr. Xiaorong Liu, whose tireless guidance in all things academic provided the scaffolding for every project, presentation, publication, and educational experience of my graduate studies. Encouraging, enlightening, and engaging, Dr. Liu's support has been central to my success, and had it not been for her continued mentorship, I would never have managed to produce this dissertation and the attached research.

So too I would like to thank Dr. Ignacio Provencio, a frequent collaborator and model scientist whose expertise was integral to many of the projects herein. His wisdom as an educator and researcher was a frequent source of inspiration over the last five years.

Thank you also to my other committee members, including my Committee Chair, Dr. Mark Beenhakker, who taught me much in my early graduate schooling as a lecturer, and much more in the lead-up to this final dissertation. Thank you also to Dr. Adema Ribic and Dr. Hui Zong, both of whom have shared their knowledge and enthusiasm at many critical points over the years.

I also owe much thanks to members of the Liu and Cang labs. Dr. Mingna Liu, our lab manager, has been a crucial aid over the years, first in training me in our lab techniques, later as an administrator and colleague. I think it's safe to say no one in either lab would be able to do what we do were it not for her tireless efforts. So too I would like to thank our lab technician

John McDaniel for his help in finalizing my research papers. His efforts were instrumental in maintaining my data, colony, writing, and experiments in these tumultuous final months. Thank you also to my fellow lab members, Kara McHaney, Dr. Marta Grannonico, Dr. Pedro Magno, and Dr. Jingyi Gao, for their continued assistance and friendship over the years.

I'd also like to thank my many students who I mentored during their rotations in the Liu lab. Thank you to Carlos Rodriguez and Zuhaad Hameed for their curiosity and diligent work. Their immunohistochemistry was the foundation of much of my second first-author paper, and I wish them all the best in their own graduate studies. Thank you to Joelle Nilak and Ashley Ban, who I supervised in my final two years at UVA. They have been excellent students, and their own data/discoveries were critical in developing my findings. Much of my IHC data was collected and/or confirmed by them. Thank you also to my other students, including Charlotte Zhang, for her skillful and passionate efforts during her training, and to Jason Borst for his continued engagement with research.

Of course, none of this would be possible without the support of the Neuroscience Graduate Program. The department's respected directors, including Dr. Chris Deppman and Dr. Alban Gaultier, likewise provided much guidance over the years. Thank you also to our program coordinators, including Nadia Cempre and Kim Knotts. I would also like to thank all my fellow NGP students, whose own passion and academic excellence has inspired me at countless junctures. I'd especially like to acknowledge Joseph Uweru, Dr. Andrea Merchak, Dr. Sean Cuddy, Joshua Milstein, Dr. Hannah Ennerfelt, Alexander Ball, Thaddeus Weigel, and Lisa Post.

Lastly, I would like to thank my many friends and family who have supported me during the treacherous course of my academic career: my mother and father, Mary and Jim Cole, who

weathered many ramblings both excited and exasperated. Their years of love and support provided me with many of the intellectual and personal skills necessary to reach this point.

Thank you to my friends Chandler McGraw, Thomas Kidd, Tristan Crum, and Joshua Luckenbaugh for surely taking the brunt of my stress on occasion, and the all the folks of WriterHouse, Eunoia, Virginia Writers Club, and Charlottesville Writers/Poetry Critique Circles for providing me much needed outlets when science became too much.

Table of Contents

Abbreviations

ASO: antisense oligonucleotide treatment

Calb: calbindin

ChAT: choline acetyltransferase

DAPI: 4’,6- diamidino-2-phenylindole

ERG: electroretinography

GCL: ganglion cell layer

GFAP: glial fibrillary acidic protein

hs: hotspot

Iba1: ionized calcium binding adaptor molecule 1

I-C: iridocorneal angle

INL: inner nuclear layer

IOP: intraocular pressure

IPL: inner plexiform layer

MEK/MAPK: mitogen-activated protein kinase kinase

OCT: optical coherence tomography

ONH: optic nerve head

ONL: outer nuclear layer

OPL: outer plexiform layer

PAX6/PAX6: human paired-box protein 6 (*gene*/protein)

Pax6/Pax6: mouse paired-box protein 6 (*gene*/protein)

PD: PD0325901 MEK-inhibitor

PTC: premature termination codon

Rbpms: RNA binding protein, mRNA processing factor

RGC: retinal ganglion cell

RNFL: retinal nerve fiber layer

RPC: retinal precursor cell

SC: Schlemm’s canal

Sey: small-eye mouse model

TM: trabecular meshwork

TRID: translational readthrough-inducing drug

Tuj1: beta tubulin III (neuron class specific)

Veh: vehicle-treated group

Vis-OCT: visible light optical coherence tomography

Chapter 1: Neural damage and neuroprotection with glaucoma development in aniridia

James D. Cole[1,2] , Carlos Rodriguez[1], Pedro Norat[1], Jingyi Gao[1], Ignacio Provencio[1,3], Peter A. Netland[3], Xiaorong Liu[1,3,4]

1- *Department of Biology, University of Virginia, Charlottesville, VA*

2- *Neuroscience Graduate Program, University of Virginia, Charlottesville, VA*

3- *Department of Ophthalmology, University of Virginia, Charlottesville, VA*

4- *Department of Psychology, University of Virginia, Charlottesville, VA*

Corresponding author: Xiaorong Liu, xl8n@virginia.edu

Funding information: This work was supported in part by NIH grants R01EY029121, and R01EY026286.

Conflict of Interest: None.

Acknowledgements

We thank Drs. Mingna Liu and Marta Grannonico for their helpful comments.

1.1 Introduction

Aniridia is a rare congenital disorder distinguished by the complete or partial absence of the iris. This panocular condition presents with a range of eye abnormalities, each to differing extents, such as cataract formation, keratopathy, and foveal and/or optic nerve hypoplasia (Hingorani et al., 2012; Samant et al., 2016; Tzoulaki et al., 2005; Yokoi et al., 2016). Common symptoms such as cataract may be clinically addressed by topical medication or surgical intervention. However, there are no treatments available to reverse neural loss, most critical for vision (Axton et al., 1997; Bobilev et al., 2016; Hingorani et al., 2012; Moosajee M, 2018; Prosser and van Heyningen, 1998; Samant et al., 2016). Of particular importance are retinal ganglion cells (RGCs), neurons that project axons to form the optic nerve, and transmit visual information from the eye to central brain structures (Sanes and Masland, 2015). About 90% of aniridia patients have a characteristic disruption of the RGC fiber layer and underdeveloped fovea, the portion of the retina responsible for acute central vision (Samant et al., 2016). Similarly, in a rodent model of aniridia, whole-mounted retinas show one-third fewer Brn3a-expressing RGCs than wildtype controls (Katagiri et al., 2017; Manuel et al., 2008). Optic nerve hypoplasia and associated retinal nerve fiber layer thinning have also been reported in approximately 10% of aniridia patients and may occur independently of foveal hypoplasia (Katagiri et al., 2017; McCulley et al., 2005). In both instances, patients suffer from varying degrees of vision loss (Tremblay et al., 1998).

Approximately 90% of aniridia patients have an underlying heterozygous mutation of the *PAX6* gene located on chromosome 11p13 (Hingorani et al., 2012; Samant et al., 2016). PAX6 is a highly conserved transcriptional regulator crucial for ocular, endocrine, and central nervous system development (Mi et al., 2013; Samant et al., 2016). Two-thirds of aniridia patients inherit an autosomal dominant mutation for the disorder while the disease in the remaining third stems

from sporadic mutations. About fifty percent of these *PAX6* haploinsuffiencies are due to premature termination codons (PTCs) introduced by in-frame nonsense mutations (Bobilev et al., 2016). In mice, homozygous loss of *Pax6* gene is neonatally lethal, whereas heterozygotes are viable but show high phenotypic variability due to individual differences in expression levels (Mi et al., 2013). Despite variation, *Pax6* haploinsufficient *Small eye* (*Sey*) mouse models have similar mutations and exhibit phenotypes like those seen in patients, making them ideal systems to study the mechanisms of retinal malformation in aniridia (Hickmott et al., 2018; Mi et al., 2013) (Fig. 1.1A).

Aniridia's wide range of deleterious symptoms often results in severe vision loss and anterior eye occlusion. Although the neural damage is irreversible, there are several promising treatments being studied to aid proper retinal development in the context of *PAX6*-based aniridia (Bobilev et al., 2016; Cole et al., 2022; Gregory-Evans et al., 2014; Hickmott et al., 2018; Rabiee et al., 2020; Wang et al., 2017). For example, PD0325901, a potent small molecule MEK inhibitor, significantly increases the expression of *PAX6*, which in turn limited the development and progression of the congenital defects in *PAX6* deficient aniridia mice ($Pax6^{Sey\text{-}Neu/+}$) (Cole et al., 2022; Rabiee et al., 2020). Another example is the use of nonsense suppression therapy in the weeks following eye-opening which has presented encouraging evidence for the amelioration of visual deficits and neural health (Gregory-Evans et al., 2014; Wang et al., 2017).

The combination of anterior eye defects and existing retinal damage from ocular hypoplasia contributes to increased RGC loss due to elevated intraocular pressure (IOP). IOP elevation is one of the most potent and damaging risk factors for glaucoma development (Quigley, 1999). Commonly identified by visual field tests and optic disc deformation, glaucoma is prevalent in around 50% of aniridia patients (Netland, 2015; Netland et al., 2011; Quigley, 2005). However,

diagnosis of glaucoma does not typically occur until a mean age of 13.6 years, more than a decade after the initial diagnosis of aniridia (mean 22 months), again emphasizing the importance of early detection and mitigation of neural damage (Netland et al., 2011).

1.2 Mouse models of aniridia

Mammalian models are the most viable for studying ophthalmological conditions, and the diverse range of mutations and backgrounds in aniridic mouse models makes them especially ideal for assessing the wide range of possible genotypic and phenotypic effects of the disease (Chang et al., 2002; Cvekl et al., 2004; Geng et al., 2011; Hickmott et al., 2018). Many murine model have been used, but much recent translational work has focused on the so-called *small-eye* (*Sey*) mouse models, so named for their prevalent microphthalmia (Graw et al., 2005). Subsequent chapters of this work utilize three such *Sey* models representing two types of mutations and three different genetic backgrounds.

Firstly, a $Pax6^{Sey\text{-}Neu/+}$ model from a Balb-c (albino) background (Cole et al., 2022; Rabiee et al., 2020). This model derives from a chemically-induced frameshift mutation (G→T) at the +1 position of the splice donor site. These mice demonstrate moderately severe phenotypes, representing non-nonsense-mutation-mediated instances of aniridia (Cole et al., 2022; Hickmott et al., 2018).

Second, a $Pax6^{Sey+/-}$ model in a C57Bl/6 background. This model has been used in numerous translation studies, particularly those investigating possible aniridic drug interventions (Gregory-Evans et al., 2014; Hickmott et al., 2018; Wang et al., 2017). These mice closely reflect the more severe, late-stage phenotypes of human patients, providing a fitting contrast to milder control phenotypes in experimental paradigms. These mice possess a PTC (Gly→STOP) at

Position 194, consistent with the most common mutation-derived forms of aniridia (Axton et al., 1997; Graw et al., 2005; Gregory-Evans et al., 2014; Tzoulaki et al., 2005). Prior studies using these mice found that they possessed high incidence of glaucomatous symptoms, drastically reduced functional outputs, and severe anterior and posterior segment abnormalities, though the severity of these symptoms varied greatly between individuals (Gregory-Evans et al., 2014; Wang et al., 2017).

Lastly, another *Pax6*$^{Sey+/-}$ mouse model from a 129S/Svlmj background was used. These mice have an Gly→STOP mutation at Position 194 identical to the aforementioned C57Bl/6 model, but, due to the epistatic effects of their background, they exhibit much milder aniridia phenotypes (Hickmott et al., 2018). This more moderate manifestation of aniridia further represents how genetic background can influence severity of the disease. Likewise, they serve as an excellent stand-in for many milder human cases, though they themselves are known to still vary greatly in their phenotypic severity (Hickmott et al., 2018).

1.3 Elevated IOP is a significant contributor to aniridia phenotypes

Glaucoma is a collection of eye diseases characterized by damage to the optic nerve and subsequent loss of retinal ganglion cells, which manifests as gradually worsening vision. One of the most common indicators of ongoing glaucomatous damage is the increase of intraocular pressure (IOP), resulting in neuronal loss (Chen et al., 2019; Netland et al., 2011; Yokoi et al., 2016). Intraocular pressure is established by the balance of aqueous humor production and outflow. Aqueous humor is produced by the ciliary body and is needed to maintain transparency of the lens and to provide nutrients to the avascular cornea and lens (Goel et al., 2010). The balance between aqueous humor formation in the ciliary body (inflow) and drainage through the iridocorneal (I-C)

angle (outflow) is crucial for preservation of a stable and normal IOP. This balance is maintained by drainage tissues such as the trabecular meshwork (TM) and Schlemm's canal (SC) in the I-C angle. Should these become occluded due to developmental malformation in undifferentiated mesenchyme, glaucomatous symptoms are likely to arise and worsen without medical intervention (Lee et al., 2008; Netland et al., 2011; Saenz-Frances et al., 2015).

Monitoring IOP is the most common clinical method to assess glaucoma. In many experimental and clinical settings, researchers have long relied on rebound tonometry to assess IOP. This technique uses a calibrated probe which, when extended to contact the corneal center of a subject's eye, will then rebound and the relative physical resistance can then be used to extrapolate IOP (typically in mmHg). Furthermore, the versatility of rebound tonometry allows IOP to be measured at regular intervals, and its minimal invasiveness makes measurements quick and easy (Netland, 2015).

However, monitoring IOP in aniridia patients can be unreliable due to considerable variations in ocular axial length, curvature, rigidity, and corneal thickness which leads to incorrectly calculated IOP measurements (Wang et al., 2005). Zakrzewska et al. found that even slight increases in central corneal thickness ($\geq$600μm) and curvature could lead to an error in measurement as high as 1.95 mmHg (Zakrzewska et al., 2019). The well-documented severity of anterior eye defects in aniridia patients, most notably corneal opacification/thickening (~691.8μm ± 75.4μm) (Whitson et al., 2005) may lead to a high incidence of erroneous IOP measurements derived by rebound tonometry. Likewise, the reduced eye growth and pronounced nystagmus typical of aniridia-afflicted mice further complicates IOP measurement, as the corneal center (the intended target of the tonometer's probe) is far smaller and in constant motion (Gregory-Evans et al., 2012). *In vivo* methods of imaging might help to better understand these changes, but the very

hindrances that complicate tonometry likewise impair imaging techniques such as optical coherence tomography (OCT).

1.4 Neural damage in aniridia

Although anterior eye defects are the most obvious and well-studied component of aniridia, recent evidence reveals that aniridia's developmental defects extend to the retina. Gregory-Evans and colleagues observed thinning or thickening of the inner and outer plexiform layers of the retina and found severe retinal folding (Gregory-Evans et al., 2014; Gregory-Evans et al., 2012; Wang et al., 2017). These oxbow bends and distended pockets are indicators of lasting neural damage, which surely contribute to permanent visual deficits. This damage, however, is highly variable and a great deal remains unclear about how retinas are directly affected by aniridia (Wang et al., 2017).

It has been well established in prior literature that classical aniridia can induce severe vision loss (Bobilev et al., 2016; Hingorani et al., 2012; McCulley et al., 2005; Moosajee M, 2018; Samant et al., 2016; Tremblay et al., 1998). Existing studies demonstrate that this may be due, in part, to the elevated pressure arising from anterior defects, and thus preexisting retinal damage may be exacerbated. The continued IOP elevation might explain why vision gradually declines with age (Netland et al., 2011; Yokoi et al., 2016). As previously mentioned, this vision loss likely stems from a combination of the disruption of nerve fiber integrity and an estimated 30% loss of RGCs (Manuel et al., 2008). However, due to the variability observed in individuals, the average loss of RGCs might be misleading due to disregarding regional and type-specific loss of RGCs.

One problematic factor in aniridia studies is the wide phenotypic diversity among *Pax6* mutants. $Pax6^{Sey+/-}$ mice, for example, were found to suffer from a broad range of symptoms

(Gregory-Evans et al., 2014; Wang et al., 2017). Experiments using this line found that eye size, IOP, visual acuity, and ocular deformity ranged from near-normal to extreme levels in individual mice. This range in penetrance is seen in other lines, including the *Pax6*^{Sey} 129S/Svlmj mice described by Hickmott et al., and this variation extends to human subjects as well (Hickmott et al., 2018). Case studies of afflicted families have shown that while the presence of certain symptoms seems consistent among subjects with similar genetic background, the severity of these symptoms still varies greatly between individuals (Bobilev et al., 2016; Fischbach et al., 2005; Hall et al., 2019; Netland et al., 2011; Shiple et al., 2015). Such variability is likely due to a combination of individual genetics and environmental factors during early development that influence gene expression. Secondly, studies, including ours, showed that different types of RGCs respond to the glaucomatous insult differently (Chen et al., 2015; Feng et al., 2017; Feng et al., 2013b). It is even less known whether and how different subtypes of RGCs are affected with the development of aniridia.

The variability of phenotype contributes to the difficulty of conducting aniridia studies. The efficacy of treatments and the impact of experimental models can be masked by this symptom variability. Longitudinal *in vivo* studies of individual subjects are one approach to account for the specific severity of aniridia phenotypes. By tracking IOP, visual acuity, eye size, functional retinal output (i.e. ERG), and assessing changes in retinal health as a subject ages, one can accurately evaluate developmental changes without the confounding effects of individual variation.

1.5 Functional consequences of aniridia phenotypes

Disruption of retinal layers impedes the transmission and processing of visual information, so techniques like optical coherence tomography (OCT) have been employed to visualize layers of

the retina *in vivo*. Aniridia patients display an increase in central foveal thickness of around 82 µm whereas surrounding parafoveal layers were significantly diminished, supporting observations of disrupted foveal development and hypoplasia (Pedersen et al., 2020). Electroretinogram tests in mice with diminished *PAX6* show impairment of retinal function with scotopic responses dropping from ~600 µV to nearly 0 µV and photopic responses dropping from ~80µV to ~2µV (Gregory-Evans et al., 2014). The degree to which ERG responses decrease varies between individual patients. Variations also exist when comparing mice and humans (Gregory-Evans et al., 2014; Hickmott et al., 2018; Moosajee M, 2018; Pedersen et al., 2020; Tremblay et al., 1998; Yokoi et al., 2016). When normalized, studies in humans have shown responses with amplitude reductions of only 14% in the scotopic state and 5% in photopic conditions for patients with PTC mutations (Tremblay et al., 1998). This range of variation further emphasizes the importance of pursuing increased translational studies of *PAX6* mutant phenotypes.

The role of Pax6 as a critical transcription factor supports the finding that much of this neuronal dysfunction in patients with aniridia extends beyond the retina to visual processing centers in the brain (Free et al., 2003; Sisodiya et al., 2001). Hypoplasia of the pineal gland and disruption of naturally oscillating genes in the hypothalamus indicate lack of synchrony with day/night patterns critical for circadian rhythms (Chhabra et al., 2020; Ellison-Wright et al., 2004). Using region-of-interest based estimates, insufficient cell proliferation has been linked to a reduction of cells in the occipital lobe with a mean area loss of 1619 mm^2 in patients severely affected by *PAX6* haploinsufficiency (Yogarajah et al., 2016). Increased functional connectivity in the primary visual network of aniridia patients is observed as a compensatory mechanism for the attenuation of regions like the occipital lobe (Pierce et al., 2014; Yogarajah et al., 2016).

Cortical disruptions are also associated with various intellectual disabilities as well as additional sensory deficits including reduced olfaction and hearing impairment (Sisodiya et al., 2001).

At the same time, as retinal ganglion cells project to the higher visual centers, miswiring and disrupted connection may affect the structure and function of post-synaptic neurons in the brain, particularly in instances where axon guidance and fasciculation are impaired (Lalitha et al., 2020). Anterograde transsynaptic degeneration has been well established in patients with glaucoma. Lateral geniculate nuclei of glaucoma patients presented with an approximate 55% reduction in laminar volume after eight weeks of elevated intraocular pressure (Weber et al., 2000). This volumetric loss incorporates reduction of soma size, soma density, and dendritic branching (Weber et al., 2000). Loss of RGC innervation in the superior colliculus produces neurons with diminished responses to visual stimulation and abnormal receptive field properties (Chen et al., 2015). Continued research is needed to further investigate how retinal damage and the brain interact and affect each other in aniridia.

1.6 Ataluren and *PAX6* mutation suppression

Theoretically, treatments for aniridia that permit ribosomal read-through of the premature termination codon (PTC) should promote a full-length Pax6 protein (Dabrowski et al., 2018). Here, we will focus on the translational readthrough-inducing drug (TRIDs) which work by suppressing PTC recognition by the ribosome during the translation process. Aminoglycoside antibiotics, 3-[5-(2-fluorophenyl)-1,2,4-oxadiazol-3-yl] benzoic acid (ataluren), and ataluren oxadiazole analogues are three different classes of drug which act as TRIDs (Ng et al., 2018). Aminoglycosides have been used for decades to treat infection by gram negative bacteria by interfering with the bacterial ribosome (Leubitz et al., 2019). There are several subtypes of

aminoglycosides, but gentamicin has shown the best efficacy in bypassing the PTC (Bidou et al., 2017). However, this class of drug has many side effects such as ototoxicity and neurotoxicity and has a low specificity for the premature termination codon, occasionally reading through the correct termination codon. In contrast, ataluren, a nonsense mutation suppressant originally designed to treat Duchenne muscular dystrophy, has shown promising effects in treating aniridia (Gregory-Evans et al., 2014; Wang et al., 2017; Welch et al., 2007) (Fig. 1.1B). Ataluren (trade name Translarna®) is a member of the oxadiazole drug family, whose members contain aromatic heterocyclic rings, composed of one oxygen and two nitrogen atoms. The arrangement of these atoms in the central five-member ring increases specificity for the PTC (Campofelice et al., 2019). Despite its efficacy in a laboratory setting, the precise mechanism of ataluren remains unclear. Likewise, limitations in drug transport demonstrate some minor application issues (Gregory-Evans et al., 2014). Ataluren is typically taken orally, but this route of administration has shown negligible localization of the drug to posterior eye regions. Similar setbacks have been seen in injection and topical applications (Gregory-Evans et al., 2014; Wang et al., 2017).

Nevertheless, Gregory-Evans et al. have shown near-wildtype levels of rescue in treated *Pax6*$^{Sey+/-}$ mice (Gregory-Evans et al., 2014; Wang et al., 2017). In their 2014 study, two daily doses of their novel topical START formulation (0.9% sodium chloride, 1% Tween 80, 1% powdered ataluren, 1% carboxymethyl-cellulose) were applied daily from P14 to P60. They later discovered that this time frame was critical, as it represents a time when significant *Pax6* expression is still needed for healthy ocular development. Later studies adjusting concentration and start time of their treatment, found that ataluren was most efficacious following eye-opening (P14) until ~P30. Delaying treatment showed reduced rescue effects, and in some cases, induced lens hyperplasia (Wang et al., 2017). In their initial study, they observed a functional recovery of

both scotopic (~600μV, WT: ~620μV) and photopic (~75μV, WT: ~80μV) ERG responses. Likewise, anterior eye defects and retinal layers appear near normal (Gregory-Evans et al., 2014). Likewise, it was observed that post-treatment, these rescued phenotypes remained healthy, further highlighting the importance of early intervention. However, due to their reliance on *in vitro* techniques and comparisons of retinal sections, it remains unclear whether these differences in retinal morphology are due to successful treatment or initial symptomatic variance. Likewise, it remains unclear the degree of morphological rescue, as there is not continuous imaging of individual eyes, but rather comparisons between different, and possibly highly varying, samples.

Despite some gaps in our knowledge of its mechanism, ataluren has been approved for the treatment of patients afflicted with Duchenne muscular dystrophy (Haas et al., 2015). The clinical trial for ataluren's application in cystic fibrosis was discontinued due to "disagreement between criteria-based CF pulmonary exacerbation definitions and clinical assessments provided by study investigators" (VanDevanter et al., 2021). Since 2016 there has been a phase 2 clinical trial, "Study of Ataluren in Participants With Nonsense Mutation Aniridia (STAR)", which recently ended (2019-2022).

1.7 Conclusion

The current rodent models of aniridia (e.g. *Pax6*$^{Sey+/-}$) provide valuable information about the etiology, progression, and drastic phenotypic changes induced by classical aniridia. Their genotypic and phenotypic resemblance to the most common forms of human aniridia make them ideal for studies that seek to understand the underlying relationship between *PAX6*, glaucoma, and subsequent vision loss. However, much more work is needed to account for variable penetrance between subjects and neural damage progression with age. Detailed longitudinal *in vivo* assessments of aniridia phenotypes must be performed regularly throughout early post-natal

development to better characterize how early damage can be compounded by other existing conditions such as glaucoma. Likewise, potential drug therapies, such as ataluren, must be tested in a similar long-term *in vivo* context to establish their most efficacious methods of administration.

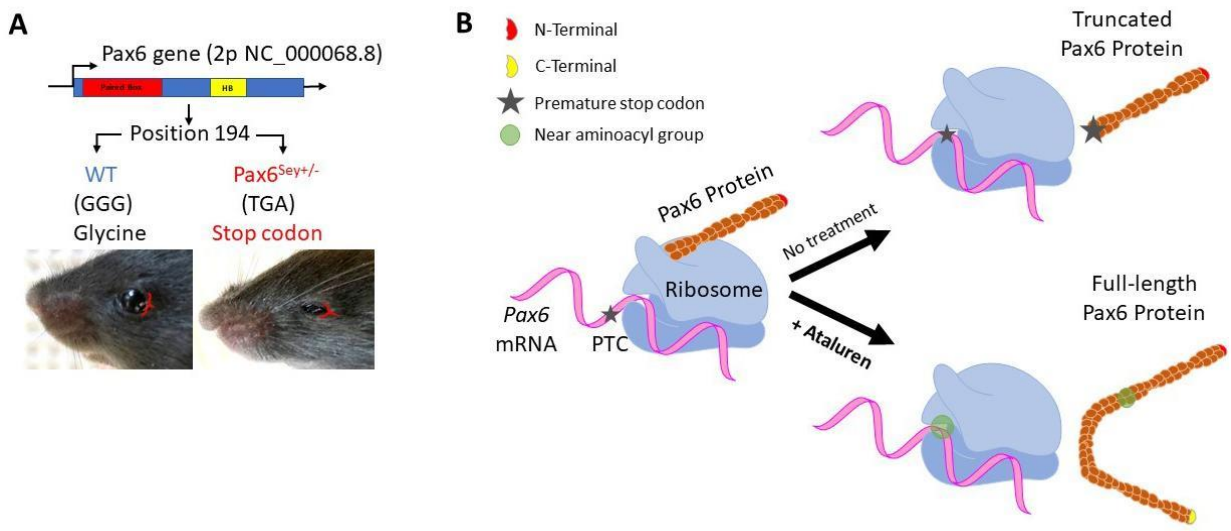

Figure 1.1 Nonsense mutation in *Pax6* produces small-eye aniridia phenotype. (A) Diagram of *Pax6* gene in mice (located 2p NC_000068.8). The $Pax6^{Sey+/-}$ mouse model features a Gly →STOP nonsense mutation, which results in a truncated protein product. Without proper Pax6 dosage, heterozygous mutants are born with a small-eye phenotype. (B) Illustration of the proposed nonsense suppression mechanism of ataluren. When mutant *Pax6* mRNA is undergoing translation, ataluren helps to insert a near aminoacyl group in place of the premature stop codon (PTC), allowing full-length translation of the protein.

Chapter 2: Long-term retinal protection by MEK inhibition in Pax6 haploinsufficiency mice

James Cole[1,2] *, Kara McHaney[2*], Behnam Rabiee[3,4], Ashley Ban[2], Jingyi Gao[2], Carlos Rodriguez[2], David Miller[5], Mingna Liu[2], Marta Grannonico[2], Pedro Norat[2], Hao F. Zhang[5], Ali R. Djalilian[3#], and Xiaorong Liu[2,6,7#]

1- Neuroscience Graduate Program, University of Virginia, Charlottesville, VA, USA

2- Department of Biology, University of Virginia, Charlottesville, VA, USA

3- Department of Ophthalmology and Visual Sciences, University of Illinois at Chicago, IL, USA

4- Department of Opthalmology, Nazareth Hospital, Philadelphia, PA, USA

5- Department of Biomedical Engineering, Northwestern University, Evanston, IL, USA

6- Department of Psychology, University of Virginia, Charlottesville, VA, USA

7- Program in Fundamentals of Neurosciences, University of Virginia, Charlottesvilla, VA, USA

(*) Co-first authors.

(#) Corresponding authors: Xiaorong Liu, xl8n@virginia.edu. Ali Djalilian, alidjalili@uic.edu

Conflict of Interests: None

Acknowledgments: This work was supported by NIH/NEI R01EY024349 (ARD), R01EY026286 and R01EY029121 (XL), and Vision For Tomorrow (ARD).

2.1 Abstract

Aniridia is a panocular condition characterized by impaired eye development and vision, which is mainly due to the haploinsufficiency of the paired-box 6 (*PAX6*) gene. Like what is seen in aniridia patients, Pax6-deficient mice *Pax6*$^{Sey\text{-}Neu/+}$ exhibit a varied degree of ocular damage and impaired vision. Our previous studies showed that these phenotypes were partially rescued by PD0325901, a mitogen-activated protein kinase kinase (MEK or MAP2K) inhibitor. In this study, we assessed the long-term efficacy of PD0325901 treatment in retinal health and visual behavior. At about one year after the post-natal treatment with PD0325901, *Pax6*$^{Sey\text{-}Neu/+}$ mice showed robust improvements in retina size and visual acuity, and the elevated intraocular pressure (IOP) was also alleviated, compared to age-matched mice treated with vehicles only. Moreover, the *Pax6*$^{Sey\text{-}Neu/+}$ eyes showed disorganized retinal ganglion cell (RGC) axon bundles and retinal layers, which we termed as hotspots. We found that the PD treatment reduced the number and size of hotspots in the *Pax6*$^{Sey\text{-}Neu/+}$ retinas. Taken together, our results suggest that PD0325901 may serve as an efficacious intervention in protecting retina and visual function in aniridia-afflicted subjects.

2.2 Introduction

Aniridia is a panocular developmental eye disorder that causes varied visual impairments in young patients (Cole et al., 2022; Glaser et al., 1994; Graw et al., 2005; Gregory-Evans et al., 2014; Hingorani et al., 2012; Lee et al., 2008; Nishina et al., 1999; Simpson and Price, 2002; Yokoi et al., 2016). In about 90% of cases, aniridia is associated with mutations in the *PAX6* gene, which encodes for a transcription factor necessary for regulating eye and brain development, as well as olfactory and pancreatic development (Cvekl et al., 2004; Glaser et al., 1994; Graw et al., 2005; Hingorani et al., 2012; Lima Cunha et al., 2019; Nishina et al., 1999; Samant et al., 2016; Wang et al., 2017). Previous studies suggest that compensation for the loss of Pax6 protein dosage during early development could counteract the potential ocular and systemic abnormalities (Rabiee et al., 2020; Yasue et al., 2017). For example, we recently demonstrated that treatment of newborn Pax6-deficient mice with topical or systemic PD0325901 led to significantly increased corneal Pax6 levels, improved corneal morphology, and enhanced ocular function (Cole et al., 2021; Rabiee et al., 2020).

However, much remains to be characterized about the long-term protective effects this treatment has on retinal health and visual behavior. As retinal damage is one of the primary contributors to visual deficits in aniridia, it is crucial to monitor the retinal morphology and function both during and after PD0325901 treatment. Most, if not all, aniridia patients exhibit varying degrees of foveal hypoplasia, and about 10% of patients have optic nerve hypoplasia (Gregory-Evans et al., 2014; McCulley et al., 2005; Sannan et al., 2017), suggesting uneven or localized damage of varying severity among individual patients. Likewise, an increase in intraocular pressure (IOP) is present in about 50% to 85% of aniridia patients but has not been examined in mice (Cole et al., 2021; Netland et al., 2011). The elevated IOP leads to diminished

vision as subjects age (Cole et al., 2021; Hingorani et al., 2012; Lee et al., 2008; Netland et al., 2011; Samant et al., 2016).

In this study, we characterized the long-term protective effects of PD0325901, a mitogen activated protein kinase kinase inhibitor, on the retina and vision in adult *Pax6*$^{Sey\text{-}Neu/+}$ mice. Previous studies have found that MAPK/ERK signaling regulates the transcription factors involved in early development, including Pax6 (de la Puente et al., 2016; Rabiee et al., 2020; Solberg et al., 2019). We thus sought to determine whether inhibiting MEK pathways via PD0325901 may compensate for the retinal damage induced by the reduced dosages of Pax6 in heterozygous mutants. At one year after the post-natal treatment of PD0325901, we measured IOP, size of the retina, and visual acuity. In addition, we characterized retinal damage in whole-mounted retinas and histological sections and found that topical application of PD0325901 from P5 to P30 provides robust protection against aniridic retinal damage.

2.3 Materials and Methods

2.3.1 Mice and PD0325901 treatments

Pax6$^{Sey\text{-}Neu/+}$ mice with a Balb-c background were used in this study (Rabiee et al., 2020). These mice were bred by crossing heterozygous mutants with wildtype (WT), and pups were genotyped according to the published protocol (Rabiee et al., 2020). The animal protocols were approved by the Committee on the Ethics of Animal Experiments of the University of Illinois at Chicago and the University of Virginia. All procedures were conducted in compliance with the recommendations of the Association for Research in Vision and Ophthalmology (ARVO) and the National Institutes of Health (NIH) guidelines.

Topical administration of PD0325901 (abbreviated as PD) consisted of 1 mM PD0325901, 2% dimethyl sulfoxide (DMSO), and 2% hydroxypropyl methylcellulose in phosphate buffered saline (PBS) (Rabiee et al., 2020). Topical treatment of PD or vehicle was applied once a day to both eyes for 5 days, and this schedule was repeated after a two-day break, starting at post-natal day (P) 5 up to P30 (LoRusso et al., 2010; Rabiee et al., 2020). Formulations were applied directly to the palpebral membrane prior to eye opening, which were able to penetrate this membrane and translocate to the eye (Rabiee et al., 2020). The last PD treatment was at P30, and all the following measurements described below were carried out at 10-14 months of age.

2.3.2 Retina Size, Intraocular Pressure (IOP), and Optomotor Tests

The widths of whole-mounted retinas were measured using the average widths of the superior inferior and nasal-temporal leaflets of each retina. Mice were restrained using plastic sleeves without anesthesia, and the intraocular pressure (IOP) was measured using a TonoLab rebound tonometer (Chen et al., 2015; Cole et al., 2021; Feng et al., 2013a; Feng et al., 2016; Puyang et al., 2016; Yi et al., 2016). Optomotor response was tested using the PhenoSys qOMR system (PhenoSys, GmbH, Berlin, Germany). Because the wildtype mice with albino Balb-c background exhibited a severely reduced visual acuity (Rabiee et al., 2020; Yeritsyan et al., 2012), we counted the number of optomotor responses elicited at a single frequency, one known to induce robust responses in WT Balb-c mice (Rabiee et al., 2020). In brief, mice were adapted to the system for 5 minutes, then gratings were presented for 2 minutes at the frequency of 0.10 cycles/degree rotating clockwise and counterclockwise every 10 seconds (Rabiee et al., 2020; Rangarajan et al., 2011). The number of optomotor responses elicited during this time was tallied

for each mouse. A mouse's response was considered "robust" if it elicited four or more optomotor responses, "moderate" if it elicited a response one to three times, and "none" if the mouse never responded to the gratings (Rabiee et al., 2020). Observers were blind to treatment/genotype groups before and during the experiments for all above procedures. Mouse genotype and treatment were revealed afterwards for data analysis.

2.3.3 Immunohistochemistry and Confocal imaging

Mice were euthanized with Euthasol (15.6 mg/mL; Virbac, Greely, CO, USA) and perfused with 4% paraformaldehyde (PFA), then eyes were dissected and prepared for immunohistochemistry (Feng et al., 2016; Feng et al., 2013b; Miller et al., 2020). Retinal eye cups were cut into a 4-leaf clover shape for whole-mounting (see Fig 2.1C) or prepared for cryo-sectioning at 20 µm thickness. Antibodies include anti-Tuj1 preconjugated with Alexa Fluor-488 (1:1000; BioLegend, San Diego, CA), anti-rbpms (1:250; Abcam, Waltham, MA), anti- (DAPI, VECTASHIELD®, Vector Laboratories)(Feng et al., 2016; Grannonico et al., 2021; Miller et al., 2020). Confocal images were performed using a Zeiss LSM 800 microscope (Carl Zeiss AG, Oberkochen, Germany)(Grannonico et al., 2021; Miller et al., 2020).

2.3.4 Quantification of hotspots, RGC axon bundle morphology, and retinal layer thickness

On whole-mount images, hotspots were defined as areas with disorganized RGC axon bundles. The hotspot was outlined based on local characteristics of the RGC axon bundles and the underlying ganglion cell layer (GCL), including: misaligned or disorganized RGC axon bundles comparing the surrounding axon bundles going straight towards to the optic nerve head (ONH), or that the bundles were displaced around a central bulge, and an abnormal density in the GCL.

To quantify hotspot size, we used the contour measurement tool in Zeiss Zen to trace around regions with disorganized axon bundles and clumped somas in the GCL (also see Fig. 2.4, red outlines). The traced areas were cross-examined independently by two observers.

For all sagittal sections, ONH was used as a landmark. The superior end of the eye was also notched during eye dissection for orientation. Regions within the radius of 600 μm from the ONH were used for quantification of layer thickness, with three measurements being made on each side of the ONH for a total of six per retina, and the average of the six measurements was used as the layer thickness. Similarly, hotspots in sagittal sections were determined based on the following criteria: abnormal layer thicknesses, and/or absences of soma stacking in the INL and ONL, wherein cells are distributed in disorganized fashion. For each retina, the thicknesses of normal and hotspot regions were measured separately.

To examine the overall changes in RGCs, the axon bundle number per retina and axon bundle width was measured using a custom MatLab program (Grannonico et al., 2021; Miller et al., 2020). In brief, we measured the number of axons bundles at 400 μm radius from the ONH (Miller et al., 2020). Individual axon bundles were marked, and bundle width was automatically measured by the program according to the published procedure (Miller et al., 2020).

2.3.5 Statistical analysis

Statistical tests were performed using GraphPad Prism 7.0 (GraphPad Software, San Diego, CA). Multiple samples were compared using one-way ANOVA followed by post-hoc Tukey multiple comparison tests. Chi-square test was used to compare multiple parameters in the optomotor assessments. Results were reported as mean±standard error of mean (SEM) except in the analysis of the axon bundle width distribution where standard deviation was used (SD).

2.4 Results

2.4.1 MEK-inhibitor PD0325901 increases retina size and reduces elevated IOP of Pax6$^{Sey\text{-}Neu/+}$ mice.

Assessment of long-term protective effects by PD0325901 (abbreviated as PD) in *Pax6*$^{Sey\text{-}Neu/+}$ mice (abbreviated as Pax6 mice) began at P200, about 6 months following topical treatments of PD and vehicle controls (Veh) from P5 to P30 (Fig. 2.1A). First, the PD treatment reduced the elevated IOP in the Pax6 mice (Fig. 2.1B). The wild type (WT) mice treated by vehicle (WT-Veh) had a mean IOP of 14.85±0.29 mmHg (N=12), similar to the WT-PD group (15.45±0.70 mmHg, N=12, p=0.91, One-Way ANOVA post hoc Tukey tests, same test applied below). The Pax6 treated with vehicle (Pax6-Veh) exhibited an elevated IOP with a mean of 18.79±0.46 mmHg (N=26, p<0.0001, Fig. 1B), which is consistent with the glaucomatous findings seen in classical aniridia. Application of PD reduced IOP to near WT levels: the mean IOP of the Pax6-PD (N=38) was 15.80±0.37 mmHg, a substantial improvement compared to Pax6-Veh (p<0.0001).

Next, we measured the diameter of the retina using whole-mounts (Fig. 2.1C). The WT-Veh had a mean width of 4.02±0.05 mm (N=5), similar to WT-PD (4.00±0.04 mm, N=5, p>0.99), again suggesting that the vehicle or PD treatment itself did not affect size of the retina. Because the application of the PD treatment on WT mice did not appear to have any adverse effects, maintaining a mean IOP and retinal width as in WT-Veh, we combined the WT-Veh and WT-PD into one control group (Ctrl) in subsequent assessments.

Importantly, the Pax6-Veh group exhibited a significantly smaller retina (3.17±0.11 mm, N=6, p<0.0001), and the PD treatment improved the phenotype of mutant mice (3.82±0.11 mm,

N=6, p<0.0001). The Pax6-PD mice exhibited a width similar to Ctrl (p=0.21), suggesting that PD 186 treatment protected against the microphthalmic phenotype in Pax6-Veh mice.

2.4.2 PD0325901 treatment reduces retinal damage in Pax6$^{Sey\text{-}Neu/+}$ mice.

Confocal images of the cryo-sections of the retina with the ONH at the center were taken to examine the retinal layer morphology (Fig. 2.2). Our results showed that the overall retina morphology for the three groups appeared normal (Fig. 2.2A-C, left), except that some areas showed cell clumping and disorganized layer thickness, which we termed as "hotspots" (Fig. 2.2B-C, right). First, the retinal layer thicknesses of the ONL, outer plexiform layer (OPL) + INL, and inner plexiform layer (IPL) + ganglion cell layer (GCL) were measured separately as illustrated in Fig. 2.2A-C. In most areas the overall thickness of the retina was not altered and were thus labeled as "normal" areas. The total thickness (Fig 2.2D) of the control group's retina was 197.16±3.01 μm (N=5), similar to Pax6-Veh's normal area (209.64±8.41 μm, N=5), and Pax6-PD's normal area (208.79±3.03 μm, N=5). The above three groups showed no statistical significance (Ctrl vs Pax6- 199 Veh: p=0.61, Ctrl vs. Pax6-PD: p=0.68, Pax6-Veh vs Pax6-PD: p>0.99). Similarly, the individual layer structure in the normal area was also comparable. For example, the IPL+GCL thickness (Fig. 2.2G) in the control group was 66.43±2.02 μm (N=5), Pax6-Veh was 69.28±4.94 μm (N=5) and Pax6-PD was 61.88±2.65 μm (N=5, Ctrl vs Pax6-Veh: p=0.99, Ctrl vs Pax6-PD: p=0.98, Pax6-Veh vs Pax6-PD: p=0.90).

Within the Pax6-Veh hotspots, however, the total thickness significantly increased to 267.94±9.58μm (N=5), a far cry from the total thicknesses of the Ctrl (p<0.0001), Pax6-Veh normal areas (p<0.0001), Pax6-PD normal areas (p<0.0001). This aberrant thickness in Pax6-Veh hotspots appears to be the result of thickening in all sublayers. The mean thickness of the

ONL increased from 61.54±2.00 μm in the Ctrl to 77.02±2.05 μm in Pax6-Veh hotspots (p=0.03, Fig. 2.2E), the mean thickness of the OPL+INL increased from 53.73±1.17 μm to 75.7±7.52μm (p=0.003, Fig 2.2F), and the mean thickness of the IPL+GCL increased from 66.43±2.02 μm to 111.2±11.78 μm (p=0.0003, Fig 2G).

The mean total thickness of hotspot areas of Pax6-PD mice was 212.88±2.6 μm (N=5), not significantly different from Ctrl (p=0.39) or Pax6-Veh normal (p=0.99). The hotspot thickening was also reduced in most PD hotspot sublayers. The mean PD hotspot thickness was 63.21±3.0 μm in the ONL (PD hotspot vs Veh hotspot, p=0.053), 55.86±1.79 μm in the OPL+INL (PD hotspot vs Veh hotspot, p=0.008), and 80.91±2.42 μm in the IPL+GCL (PD hotspot vs Veh hotspot, p=0.015). Together these findings indicate that Pax6 mice exhibited localized neural damage with increased thicknesses in the ONL, OPL+INL, and IPL+GCL, and these phenotypes were partially alleviated by PD0325901 treatment.

2.4.3 Immunohistochemistry shows disorganized retinal sublayer structure.

We next examined different cell types in the affected layers with various antibodies (Fig. 2.3). First, rbpms (red) is a marker to label most, if not all, RGCs in the mouse retina (Gao et al., 2022b; Rodriguez et al., 2014). The rbpms stains show highly disorganized cells in the GCL of the hotspots in Pax6-Veh, correlating with the findings in the whole-mounts shown in Fig 2.2. However, the rbpms+ density of the Ctrl group was 8.17±0.45 per 100 μm segment (N=6), not significantly different from the quantification of Pax6-Veh mice in both normal (8.23±0.49 per 100 μm segment, N=6, p=0.99) and hotspot regions (6.70±0.40 per 100μm segment, N=4, p=0.32). The rbpms+ cell quantification for PD mice in both normal (7.24±0.69 per 100μm

segment, N=5, p=0.69) and hotspot regions (6.88±0.42 per 100μm segment, N=5, p=0.39) were also not significantly different from the Ctrl group (Fig. 2.3).

We next examined the inner retina structure. Choline acetyltransferase (ChAT), stains for cholinergic amacrine cells, labeling somas in the INL and the processes that form a characteristic double bands in the IPL (Feng et al., 2013a; Feng et al., 2016; Feng et al., 2013b; Yasuhara et al., 2003). Calbindin is a calcium binding protein expressed in horizontal, amacrine cells, and some RGCs (Feng et al., 2013a; Feng et al., 2016; Feng et al., 2013b; Gao et al., 2022b; Puyang et al., 2016). ChAT staining suggests that cholinergic amacrine cells are largely unaffected between the groups, though the double-bands organization in the IPL was disrupted in the hotspot regions as indicated in Fig 2.3. Calbindin+ somas in the INL in the Pax6-Veh hotspot appeared increased, possibly contributing to the thickening seen in the INL.

Finally, we examined the glial cell populations in the retina. Glial fibrillary acidic protein (GFAP) is highly expressed in the end-feet processes of Müller glia cells, a population which controls maintenance and support throughout the retina (Gallego et al., 2012). The ionized calcium-binding adaptor molecule 1 (Iba1) is a protein expressed in retina microglia (Bosco et al., 2011; Puyang et al., 2016). The GFAP expression seemed upregulated in the somas and processes of the Müller glial cells in Pax6-Veh, and the number of Iba1+ microglia appeared upregulated in the inner retina as well. In the PD-treated mice, staining pattern of both GFAP and Iba1+ microglial cells returned to the baseline level as seen in the Ctrl group.

2.4.4 PD0325901 treatment partially protects the optic nerve head phenotype in Pax6$^{Sey\text{-}Neu/+}$ mice

We examined the ONH morphology of control, Pax6-Veh, and Pax6-PD mice via confocal imaging of whole-mounted retinas. Control mice (N=8) exhibited a well-organized ONH, with axon bundles converging to form the optic nerve at the center. By contrast, Pax6-Veh (N=5) showed a disorganized ONH, wherein bundles tangled and crossed, and the somas in the GCL showed pronounced clumping, like what was seen in hotspots in cryo-sections. The Pax6-PD group (N=6) showed considerable improvement in the ONH organization (Fig. 2.4, right column). Our results suggest that PD0325901 may protect axon bundle organization in the ONH.

2.4.5 PD0325901 treatment partially alleviates hotspot phenotype in the RNFL of Pax6$^{Sey\text{-}Neu/+}$ mice

To further characterize the localized RGC damage and the neuroprotection by PD, we analyzed the whole-mounted retina from all three groups by immunostaining for RGC axons using Tuj1, a monoclonal beta-tubulin antibody (Grannonico et al., 2021; Jiang et al., 2015; Miller et al., 2020). The overall morphology of RGC axon bundles was largely normal, as shown in Fig. 2.5. Again, we noticed damaged axon bundles that overlapped with noticeable clumps of somas displaced from underlying retinal layers (Fig. 2.5A). Hotspots were identified in the regions of the whole-mount within 600 μm radius of the ONH. Regions which met our criteria (see Methods 2.3) were outlined and their areas were quantified. We counted the total number of hotspots in each retina. As shown in Fig. 2.5B, the mean number of hotspots per retina was significantly higher in Pax6-Veh mice, with a mean number of 4.2±0.6 per retina (N=5), compared to control (1.6±0.3, N=8, p=0.0002). Importantly, the mean number of hotspots was reduced in Pax6-PD (2.7±0.2, N=6, p=0.03).

We next measured the area of each hotspot and calculated the total areas from all hotspots of each retina. As shown in Fig. 2.5C, the total area of hotspots in Pax6-Veh retina was (11.2±1.6) × 10^4 μm^2/retina, significantly greater than control ((4.9±1.3) × 10^4 μm^2/retina, p=0.01). Pax6-PD exhibited a reduced hotspot area (5.7±1.1) × 10^4 μm^2 /retina which was significantly smaller than the Pax6-Veh mice (p=0.04), but not significantly larger than those in control mice (p=0.89). Our results thus demonstrated that PD treatment reduced the overall number and size of hotspots.

2.4.6 PD treatment partially preserves the number and size of RGC axon bundles in Pax6$^{Sey\text{-}Neu/+}$ mice

As Figure 2.3 showed that the rbpms+ RGC density was not significantly changed in Pax6-Veh, we next took a different approach to quantify the size and number of RGC axon bundles to get an overall estimation of the changes in RGCs. We counted the total number of axon bundles at the radius of 400 μm from the ONH (Fig. 2.6). The number of RGC axon bundles in the Ctrl group was 81.7±5.5 (N=5), and it was changed to 98.7±11.6 in Pax6-Veh (N=5, p=0.33). The number of axon bundles in Pax6-PD was 71.0±5.6 (N=6), also not significantly different from the Ctrl (p=0.60) and the Pax6-Veh (p=0.06).

The distribution of individual axon bundle width at 400 μm from the ONH was plotted in Fig. 2.6D. Measurements of individual bundles showed the mean width of Pax6-Veh was 7.34±0.16 μm (N=9 retinas, n=440 bundles), ~15% less than the controls (8.68±0.19 μm, N=6 retinas, n=356 bundles, p<0.0001). PD treatment partially diminished the effects on RGC axon bundle size (Pax6-PD: 8.35±0.25μm, N=4 retinas, n=159 bundles), compared to the Pax6-Veh (p=0.0001). There was also a significant difference between the axon bundle widths of control

and Pax6-PD (p=0.0004), suggesting a partial protection by PD treatment. Together these results suggest that axon bundles are smaller in the Pax6-Veh retina, but PD treatment protects against bundle thinning, reinforcing its efficacy as a viable aniridia intervention.

2.4.7 Long-term partial protection of visual acuity by PD0325901 treatment in Pax6$^{Sey\text{-}Neu/+}$ mice

Visual acuity was examined by the optomotor test as described in the Methods (Fig. 2.7). For control mice (N=10), six mice exhibited robust responses, and four exhibited moderate responses. By contrast, seven Pax6-Veh mice (N=9) exhibited no responses at all, and the remaining two only had moderate responses. Not surprisingly, Pax6-PD (N=10) showed predominantly (seven) robust responses, comparable to the control levels of acuity. Chi-square tests concluded that Pax6-Veh mice show a significantly different level of response from both control (p=0.0011) and Pax6-PD (p=0.003). The control and PD groups showed no significant difference in their results (p=0.42) suggesting that PD0325901 treatment partially protected against visual behavior deficits brought on by aniridic damage and maintains that acuity well into adulthood.

2.5. Discussion

2.5.1 PD0325901 provides robust protection against aniridia phenotypes

Our results indicate that treatment with the small molecule MEK inhibitor PD0325901 substantially protects against aniridic damage in *Pax6$^{Sey\text{-}Neu/+}$*. This protection extends not only to the anterior eye segment, but also to the retina and vision into adulthood. Associated aniridic symptoms such as heightened IOP, microphthalmia, and visual deficits show significant reduction in the presence of PD treatments even six-months after drug application. Likewise,

major retinal deficits such as hotspots, which could be a major contributor to visual impairment, are also reduced in both size and number with PD treatment. Abnormal thickening/wrinkling of retinal layers, though still present in Pax6-PD mice, is also remarkably decreased compared to hotspots in Pax6-Veh. While this protection is not perfect, it appears to have likewise partially improved axon bundle health and ONH morphology.

Although PD0325901's protective effects in aniridia phenotypes are clear, there is much optimization needed before treatment can effectively mitigate all aniridia symptoms. Since Pax6 dosage is necessary at many critical developmental stages both pre- and post-natally (Axton et al., 1997; Cvekl et al., 2004; Gregory-Evans et al., 2014; Lalitha et al., 2020; Li and Lu, 2005; Nishina et al., 1999; Rabiee et al., 2020; Remez et al., 2017; Warren et al., 1999; Yasue et al., 2017), potential intervention will likely prove more efficacious if also administered prior to birth. Not only will this remove early post-natal stressors on mothers and pups, but it will likely compensate for earlier damages instigated by haploinsufficiency. It is known that Pax6 is needed to facilitate differentiation and maturation of retinal progenitor cells (RPCs) in early and late-born retinal layer populations, reinforcing the necessity of earlier post-natal treatments (Remez et al., 2017). Our initial topical treatment may compensate for dosage required from P5 to P30, and this protection is demonstrably robust, but persisting damage may arise from complications not compensated either pre-natally, or in other post-natal stages requiring Pax6.

2.5.2 MEK inhibition and treatment parameters.

Previous studies have shown that MEK inhibition can indirectly influence Pax6 expression, and therefore may provide a novel avenue for Pax6 haploinsufficiency intervention (de la Puente et al., 2016; Li and Lu, 2005). This treatment has some potential pitfalls, however, as excessive

MEK inhibition has been linked to retinal detachment and retinal vein occlusion (LoRusso et al., 2010). As an MEK inhibitor, PD0325901's function highlights the significance of proliferation related pathways in the healthy maintenance of ocular phenotypes. It has been employed as an effective anti-aging treatment and has also been shown to assuage myopathic features in mice afflicted with neurofibromatosis type 1 (Castillo-Quan et al., 2019; Summers et al., 2018). Such examples verify the safety and efficacy of PD0325901 at low doses, and combined with the results of this study, demonstrates its capability in maintaining developmental pathways.

In this way, PD0325901 is comparable to another popular aniridia intervention, the nonsense mutation suppressant known as ataluren. Ataluren is purported to target Pax6 mRNA transcripts at the translational level, and it has been shown to have similar protective effects by compensating for decreased Pax6 dosage (Gregory-Evans et al., 2014; Wang et al., 2017). Like PD0325901, ataluren has also been shown to have deleterious effects at higher concentrations, such as lens hyperplasia (Wang et al., 2017). While both provide ample protection against aniridic insults, continued research is needed to further assess both MEK inhibitors and ataluren to determine which is most viable for clinical applications.

2.5.3 Variations in hotspot phenotypes and possible links to visual deficits.

Ongoing *in vivo* assessments of aniridia phenotypes are necessary to develop adequate diagnostic, prognostic, and therapeutic measures to mitigate the disease. This has proven difficult as abnormal aniridia phenotypes vary greatly between mice due to individual genetics (Cole et al., 2021; Netland et al., 2011). We found this to be particularly true of retinal hotspot damage, as the size, shape, and layer characteristics of damaged regions often varied greatly among individual mice. Our data suggests that hotspot size and number are certainly increased in

aniridic mice compared to controls. As experimenters didn't know the genotype or treatment groups when they analyzed the imaging data, it is possible that the small number of hotspots found in control mice could be due to technical issues such as dissection-induced physical damage in the retina. We also believe the disrupted areas in whole-mounts were consistent with the swollen areas seen in cryosections, as DAPI stains reveal clusters of disorganized and displaced somas from underlying layers. In addition, the GCL+IPL layers proved the most obviously affected in mutant retinas. It appears that, while thickness of layers in hotspots is altered, the layers contributing to these abnormalities can differ. Our results suggest that all layers were affected to a varied degree, and future work is thus needed to better understand the underlying mechanisms.

Our quantification of rbpms+ cells found that density of RGCs is not statistically significant between the three groups, though there appears to be a trend toward RGC density reduction in Pax6-Veh hotspots. These results coincide with other findings. For example, Hickmott et al. analyzed the total cell number in the GCLs of both WT and aniridic mice of three different backgrounds: C57Bl/6J, B6129F1, and 129S1/SvlmJ, and found no significant difference in GCL cell density between WT and aniridic mice, nor between any of the backgrounds (Hickmott et al., 2018).

Our results also suggest that other retinal cell populations might be affected (Fig. 2.3). ChAT stains seem largely normal in all three groups, but Calbindin may show a higher density of cells in the INL. This is likely the result of the increased clumping/thickening demonstrated in Fig. 2.2F. While both Ctrl and Pax6-PD maintained the expected Müller glia cells end-feet demarcation stained by GFAP, the Pax6-Veh mice showed more widespread staining in somas and processes. Iba1+ microglial cells might be upregulated in the Pax6-Veh, perhaps because of

an inflammatory response to aniridic damage. This increase in glial recruitment and activation was confirmed in Chapter 3 (Fig. 3.5 and 3.6).

It is unknown whether local damage results in global acuity reduction. For one, it has been well-documented that RGC reduction, such as that commonly seen in glaucomatous eyes (i.e. those with heightened IOP), often accompanies a decline in visual acuity (Chen et al., 2015; Feng et al., 2013b; Hood, 2019; Medeiros et al., 2013; Puyang et al., 2016). It is however important to note that no strict causal relationship has been determined between local RGC loss and the global visual reduction, and some studies have even shown a reduction in the visual field prior to RGC population decline (Hood, 2019). In fact, multiple deficits in retinal functions were detected in aniridia mice. Gregory-Evans et al performed ERG analysis at P60 and found that the scotopic responses were nearly undetectable in aniridic mice, suggesting defects in the inner and outer retina (Gregory-Evans et al., 2014), consistent with our previous findings (Rabiee et al., 2020).

Perhaps more telling is aniridia's disruptive effect on axon bundles, which is evident not only in hotspot regions (Fig 2.5) but also around the ONH (Fig. 2.4/2.6). Lower levels of Pax6 expression have been shown to impair axon fasciculation (Lalitha et al., 2020), consistent with the reduced width measures of bundles of Pax6-Veh mice (Fig. 2.6). More work is needed to understand exactly how axon disorganization/defasciculation contributes to visual deficit (Chen et al., 2015; Medeiros et al., 2013; Miller et al., 2020).

2.5.4 Conclusion

Our studies suggest that MEK inhibitors like PD0325901 provided long-term protection against aniridia-related damage in *Pax6*$^{Sey\text{-}Neu/+}$ mice. Topical application from P5-P30 reliably increased

retina size, reduced IOP elevation, and improved visual acuity. Likewise, isolated regions of retinal damage in different retinal layers saw significant reduction in clumping and disorganization when treated with PD0325901. Altogether, our results indicate that PD0325901 may serve as a reliable protective measure for patients with aniridia.

2.6 Figures

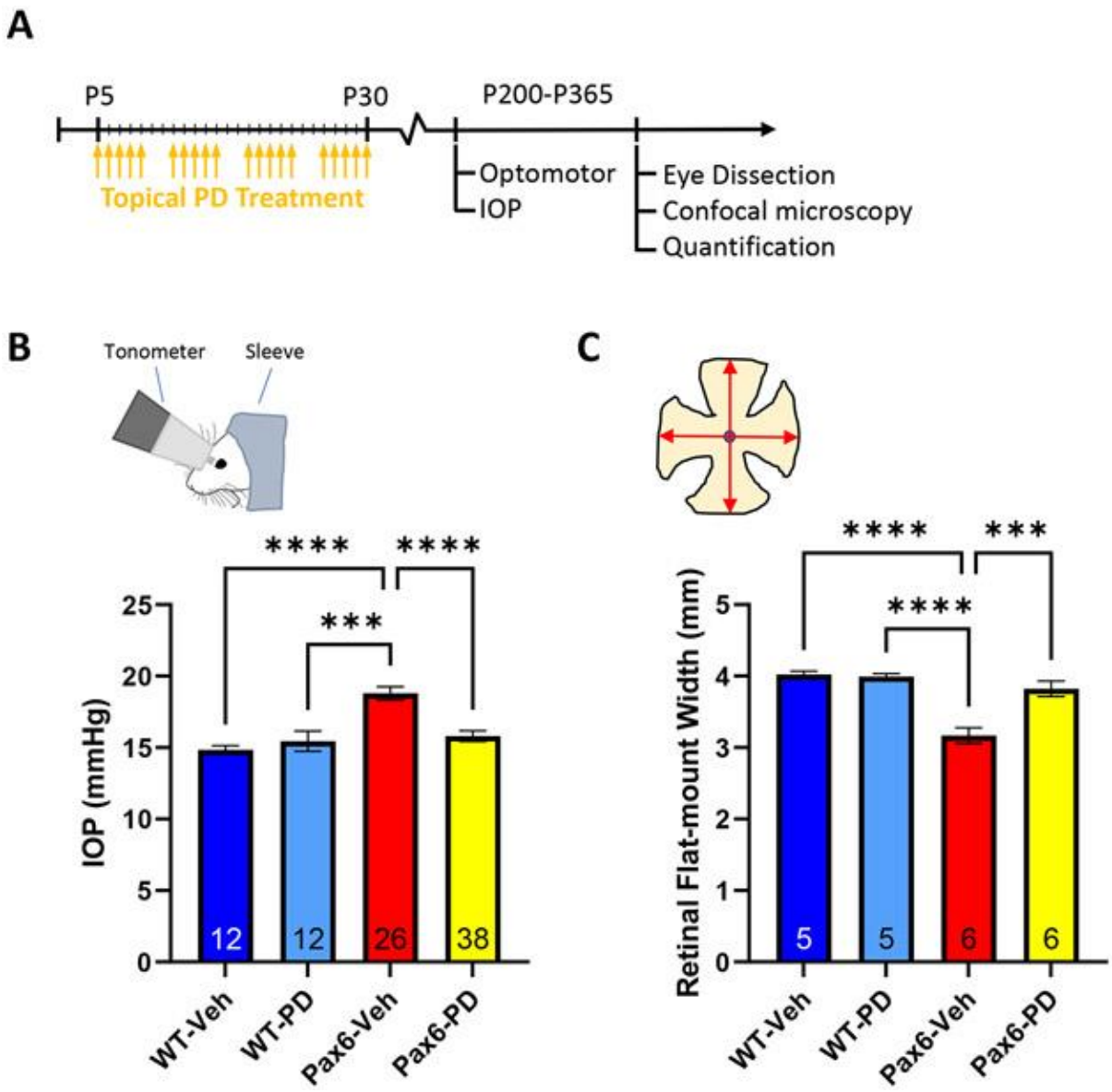

Fig. 2.1 Long-term protective effects by PD treatment on IOP and the size of the retina of *Pax6*$^{Sey\text{-}Neu/+}$ mice. (A) Timeline of experimental procedures. (B) IOP assessments of WT-Veh, WT-PD, Pax6-Veh, and Pax6-PD by a Tonolab tonometer (see inset). *Pax6*$^{Sey\text{-}Neu/+}$ was abbreviated to Pax6, Vehicle group was abbreviated to Veh, and PD0325901-treated was abbreviated as PD. (C) Comparison of retinal whole-mount width as indicated in the inset. Sample numbers labeled at the bottom of each bar. ***: P<0.001; ****: P<0.0001

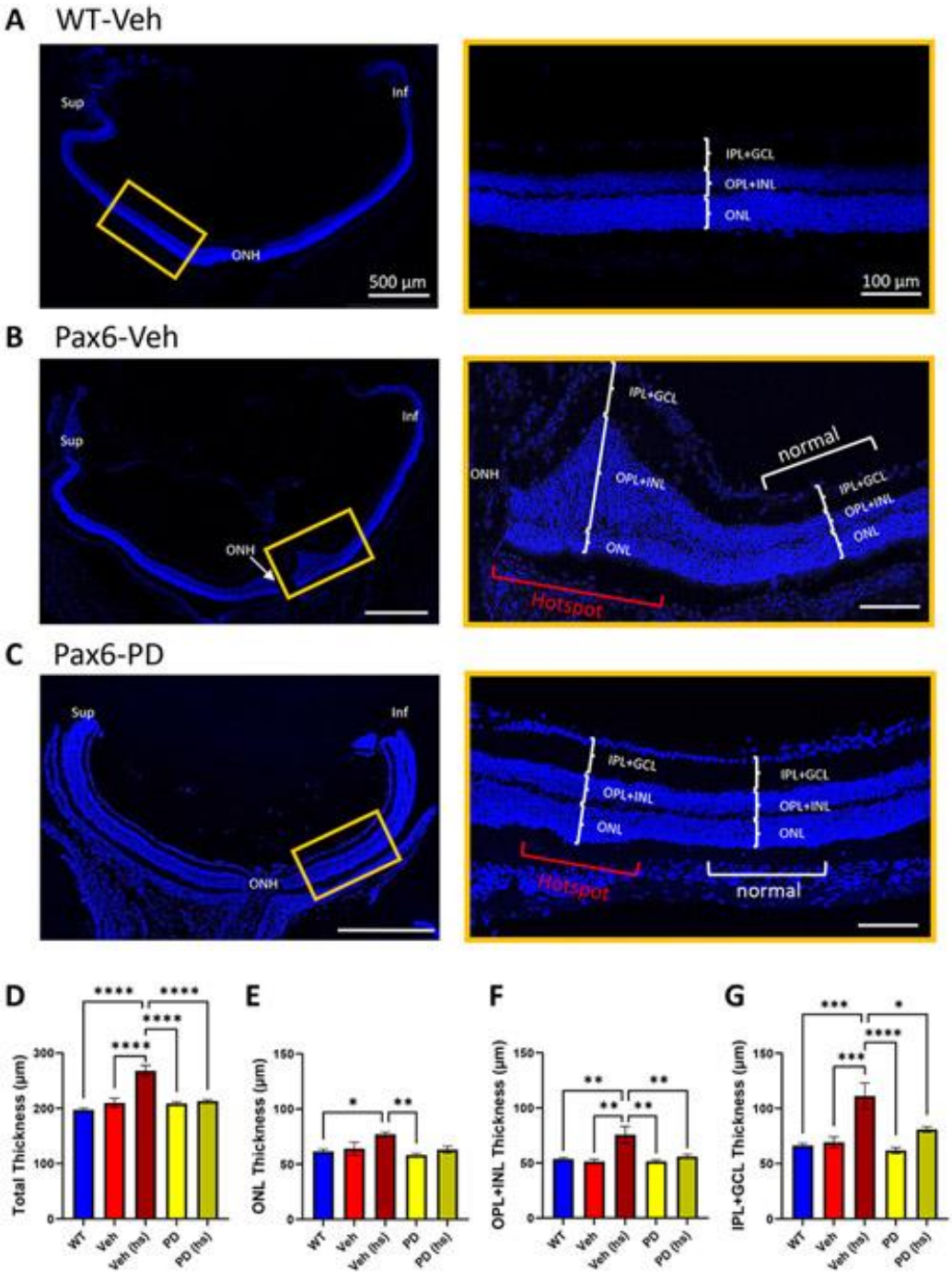

Fig. 2.2 Quantification of retinal layer thickness suggests PD protects against retinal damage in *Pax6*$^{Sey\text{-}Neu/+}$ mice. (A-C) Confocal images of retinal sections stained with DAPI (blue) with optic nerve head (ONH) at the center. Superior end of the eye is one the left in all images. Yellow box shows examples of retinal layers. Red bracket indicates a characteristic

hotspot (hs). Scale bars in A, B, C (left panels) = 500 μm, (right panels) = 100 μm. (D-H) Quantifications of layer thickness. WT-PD and WT-Veh were combined into one control group (labeled as Ctrl). *: P<0.05; **: P<0.01; ***: P<0.001; ****: P<0.0001

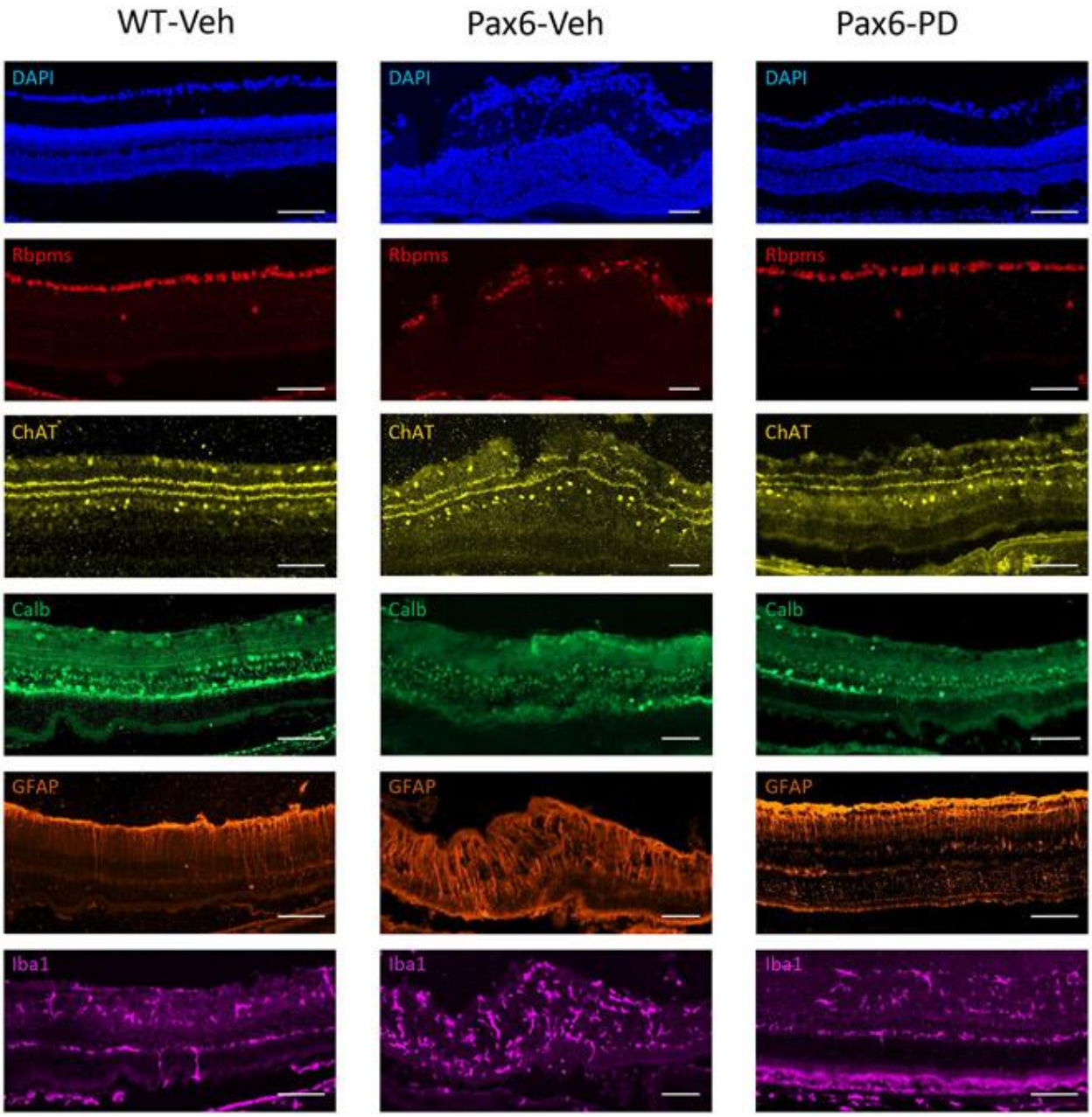

Fig. 2.3 Disorganization of different types of retina cells in hotspots. The left column shows normal retinal regions from a WT-Veh mouse as compared to the hotspots (hs) in Pax6-Veh (middle column) and Pax6-PD (right column). From top to bottom rows: DAPI, Rbpms, ChAT, Calbindin, GFAP, and Iba1, which were also labeled on the left corner. See details in the Results. Scale bar = 100 μm.

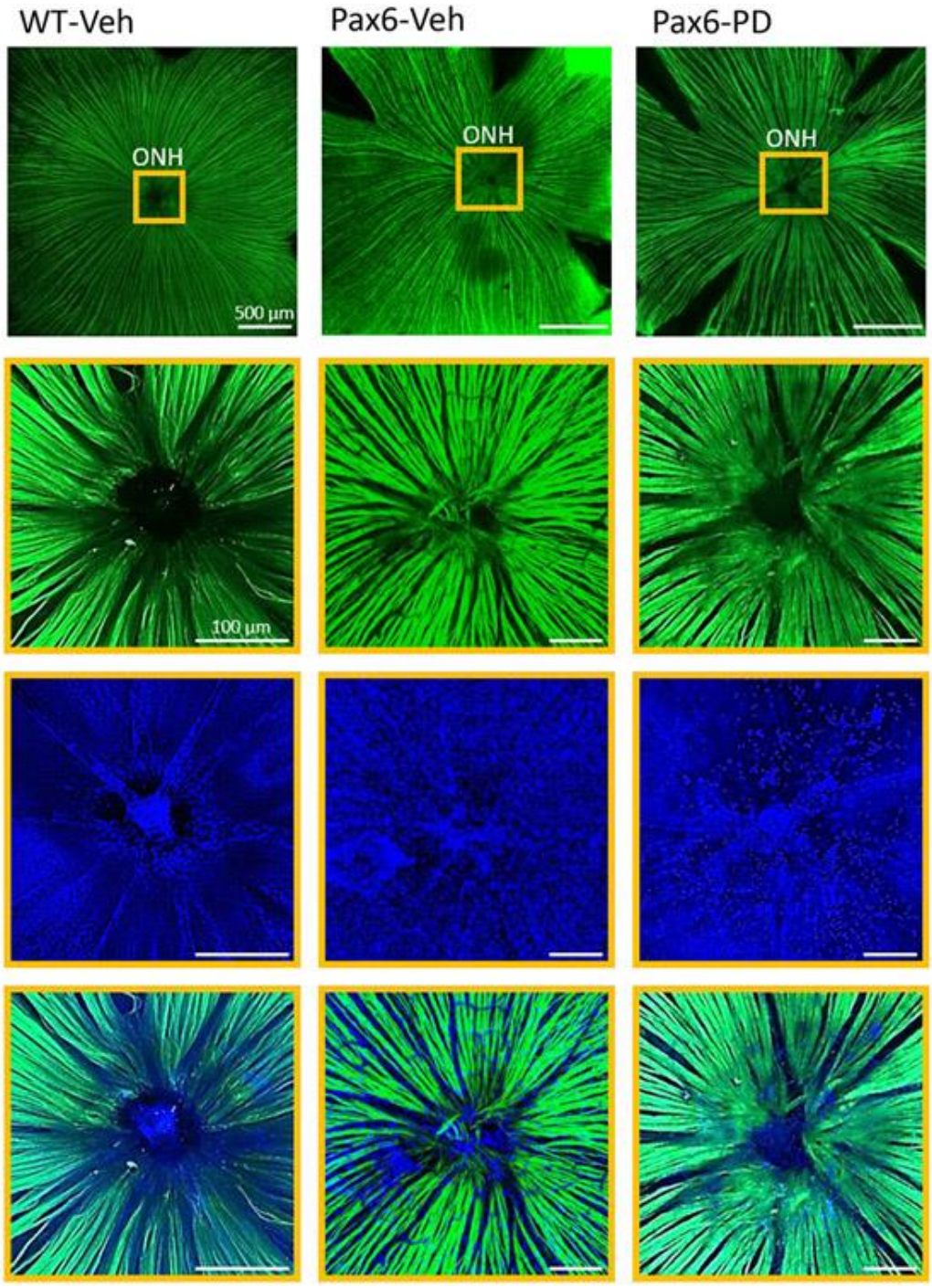

Fig. 2.4 PD treatment rescued the optic nerve head phenotype in *Pax6*$^{Sey\text{-}Neu/+}$ mice. (A) Confocal images of whole-mounted retinas immunostained by Tuj1-488 (green) for RGC axon bundles and DAPI (blue) in control, Pax6-Veh, and Pax6-PD mice. Yellow box shows the optic nerve head (ONH), where axon bundles converge to form the optic nerve as they leave the retina.

Pax6-Veh exhibited axon bundle disruption while the PD treatment partially protected the normal phenotype. DAPI stain (blue) shows increased disorganization and displacement of somas around the ONH of Pax6-Veh, while PD treatment appears to have reduced this phenotype. Scale bar in top row = 500 μm. Scale bar in bottom three rows = 100 μm.

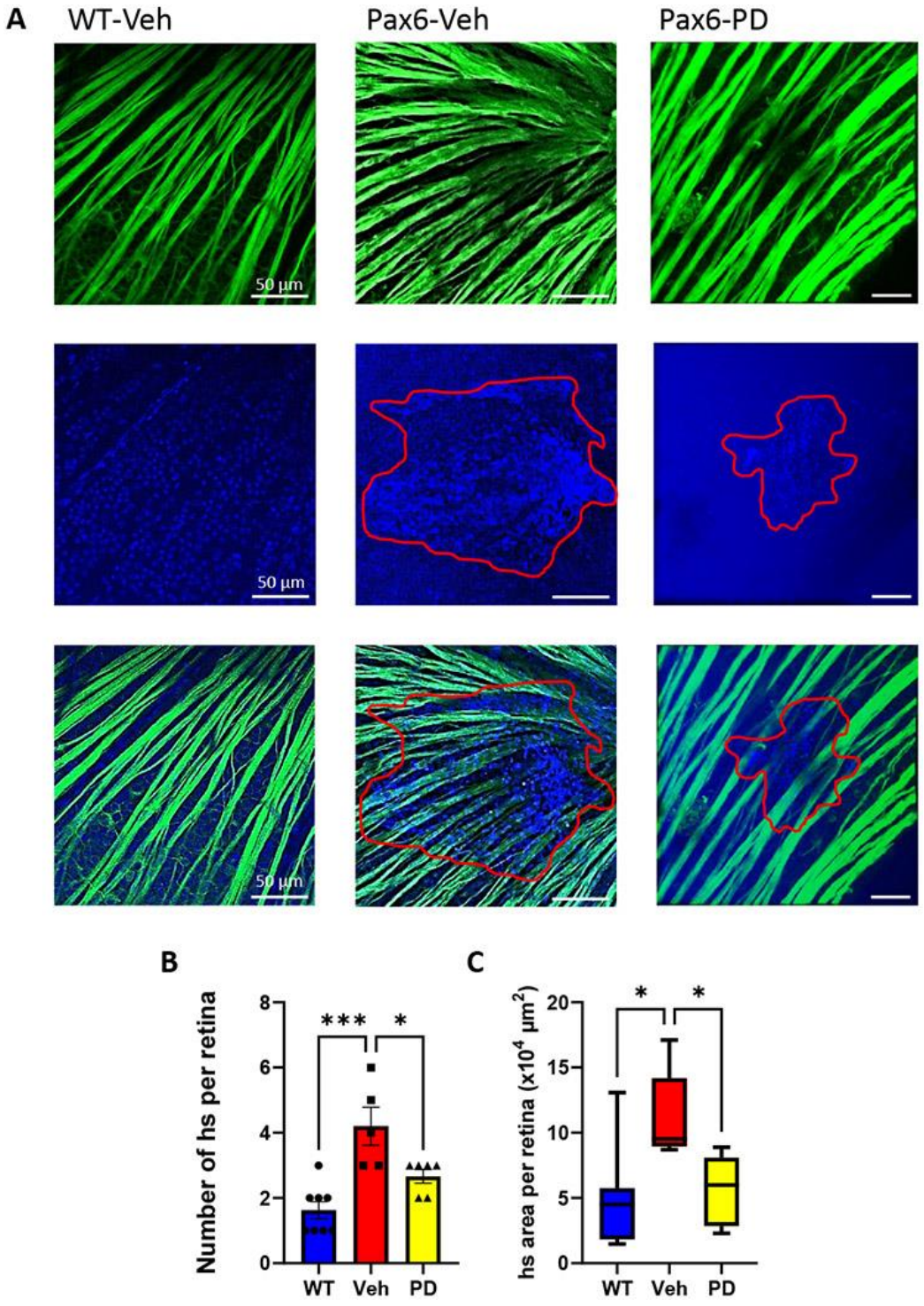

Fig. 2.5 PD treatment partially alleviated the local retinal damage in *Pax6*$^{Sey\text{-}Neu/+}$ mice. (A) Confocal images of whole-mounted retinas immunostained by Tuj1-488 (green) and DAPI (blue). Pax6-Veh and Pax6-PD showed bundle disorganization (top) and displacement of somas

from underlying layers (middle). Red outlines one hotspot in Pax6-Veh and Pax6-PD, respectively. Scale bars = 50 μm (B) Quantification of the number of hotspots per retina. (C) Box plot of the total area of hotspots per retina. Mid-lines of boxes represent median, lower and upper bounds of the box represent 25th and 75th percentiles, respectively. Ends of whiskers represent the minimum and maximum values of the data set. *: $P<0.05$; ***: $P<0.001$

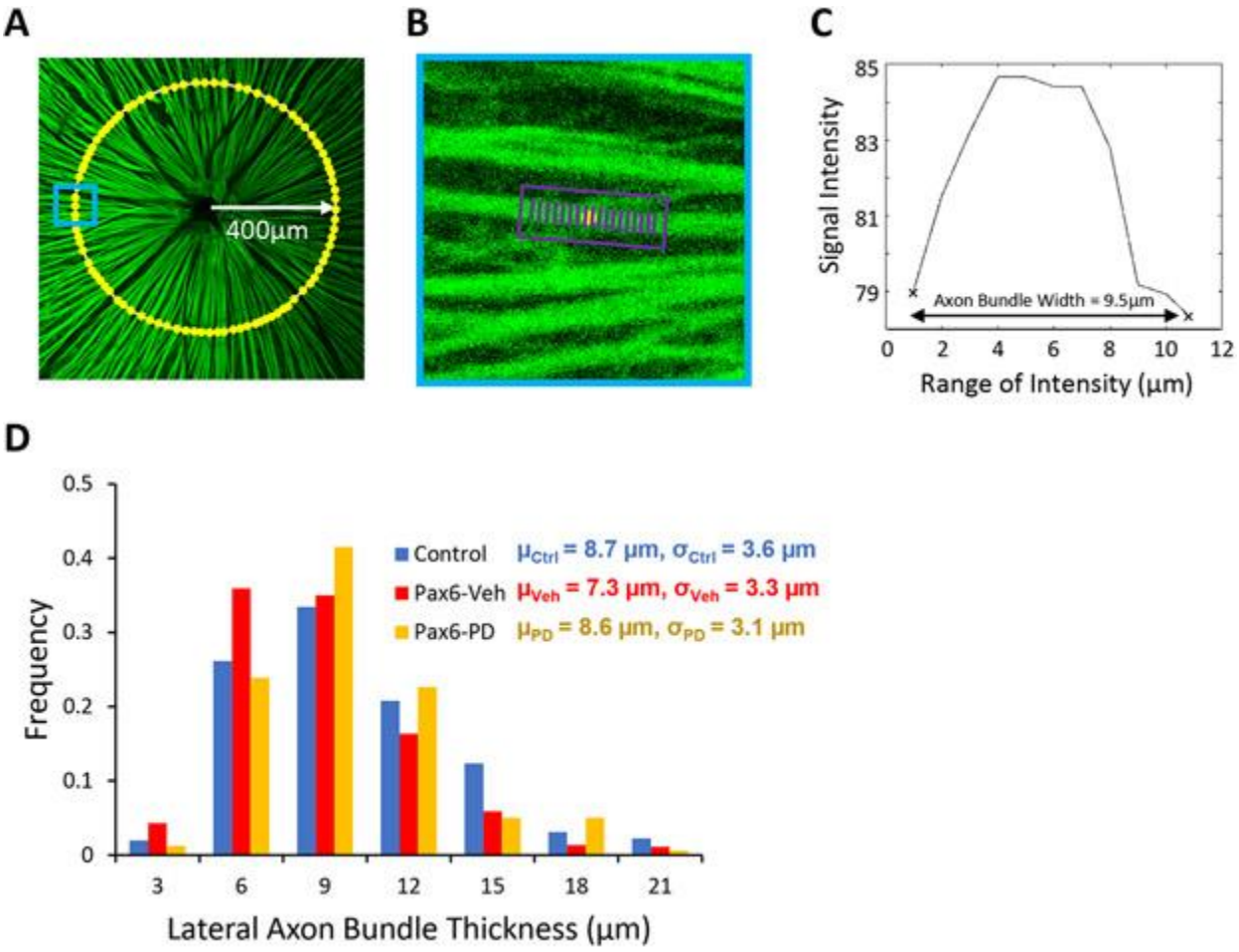

Fig. 2.6 PD treatment partially protected RGC axon bundles in *Pax6*$^{Sey\text{-}Neu/+}$ mice. (A) Schematic showing bundle assessment at 400 µm radius from ONH. Yellow dots correspond to axon bundles. (B-C) Blue box shows the close-up of an individual axon bundle marked by a yellow dot. Purple box represents width measurement based on signal intensity in MatLab (see details in 2.3 Methods). (D) Histogram of axon widths in control, Pax6-Veh, and Pax6-PD mice, means and standard deviations of each distribution indicated in top right.

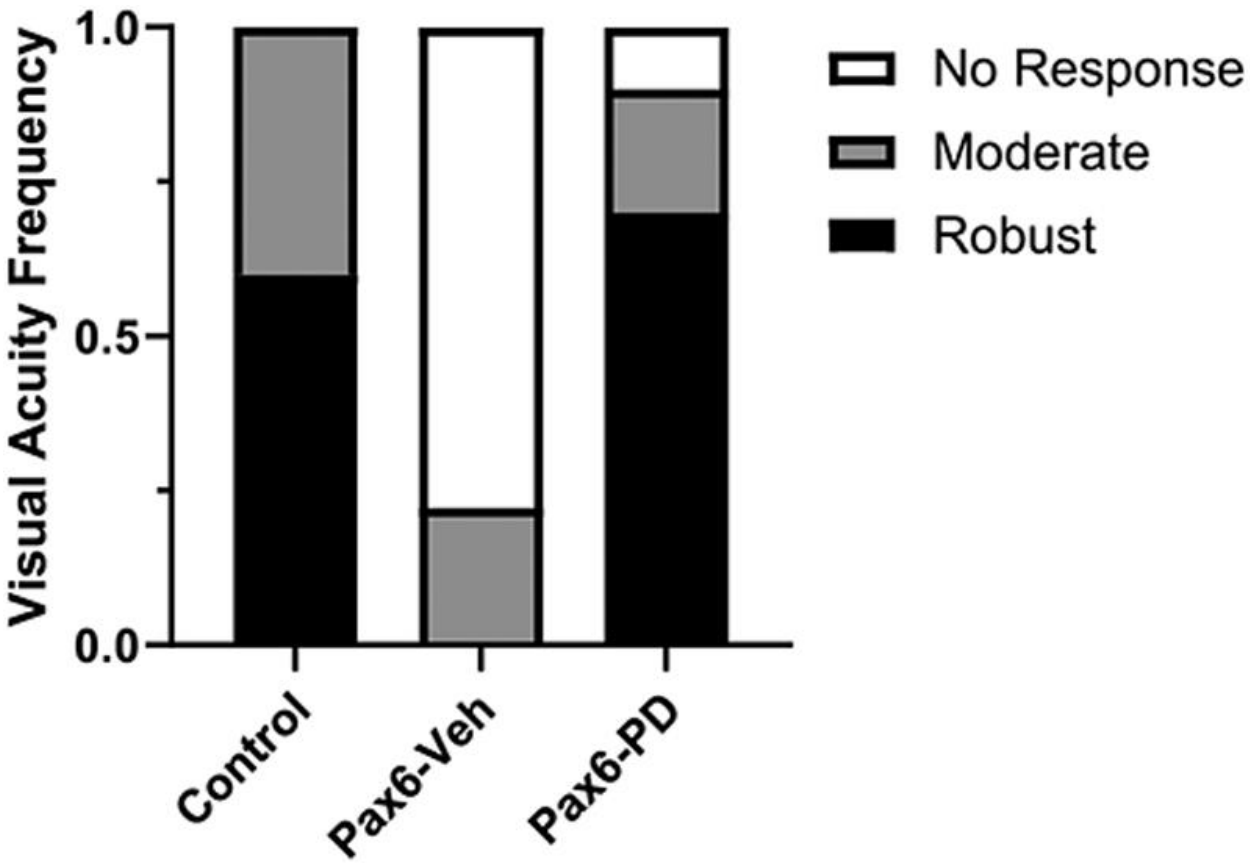

Fig. 2.7. Long-term protection of vision by PD treatment in *Pax6*$^{Sey\text{-}Neu/+}$ mice. Optomotor responses were counted for each mouse and their response was deemed robust if they responded four or more times, moderate if they responded one to three times, or none if they showed no optomotor response (see details in 2.3 Methods). Pax6-PD showed predominately robust responses similar to control mice, while Pax6-Veh largely did not respond. **: $P < 0.01$ by Chi squared test.

Chapter 3. Characterization of neural damage and neuroinflammation in Pax6 *small-eye* mice

James Cole[1,2] *, John A. McDaniel[2] *, Joelle Nilak[2], Ashley Ban[2], Carlos Rodriguez[2], Zuhaad Hameed[2], Marta Grannonico[2], Mingna Liu[2], Peter A. Netland[3], Hu Yang[4], Ignacio Provencio[2, 3, 5], and Xiaorong Liu[2, 3, 5, 6 #]

1- Neuroscience Graduate Program, University of Virginia, Charlottesville, VA, USA

2- Department of Biology, University of Virginia, Charlottesville, VA, USA

3- Department of Ophthalmology, University of Virginia, Charlottesville, VA, USA

4- Linda and Bipin Doshi Department of Chemical and Biochemical Engineering, Missouri University of Science and Technology, Rolla, MO, USA

5- Program for Fundamentals of Neuroscience, University of Virginia, Charlottesville, VA, USA

6- Department of Psychology, University of Virginia, Charlottesville, VA, USA

(*) Co-first authors.

(#) Corresponding author: Xiaorong Liu, xl8n@virginia.edu.

Conflict of Interests: None

Acknowledgments: Glaucoma Research Foundation Shaffer Grant, 4-CA Cavalier Collaborative Award, Knights Templar Pediatric Award, R01EY029121, and R01EY035088.

3.1 Abstract

Aniridia is a panocular condition characterized by a partial or complete loss of the iris. It manifests various developmental deficits in both the anterior and posterior segments of the eye, leading to a progressive vision loss. The homeobox gene *PAX6* plays an important role in ocular development and mutations of PAX6 have been the main causative factors for aniridia. In this study, we assessed how *Pax6*-haploinsufficiency affects retinal morphology and vision of $Pax6^{Sey}$ mice after eye opening using *in vivo* and *ex vivo* metrics. We used mice of C57Bl/6 and 129S1/Svlmj genetic backgrounds to examine the variable severity of symptoms as reflected in human aniridia patients. Elevated intraocular pressure (IOP) was observed in $Pax6^{Sey}$ mice starting from post-natal day 20 (P20). Correspondingly, visual acuity showed a steady age-dependent decline in $Pax6^{Sey}$ mice, though these phenotypes were less severe in the 129S1/Svlmj mice. Local retinal damage with layer disorganization was assessed at P30 and P80 in the $Pax6^{Sey}$ mice. Interestingly, we also observed a greater number of activated Iba1+ microglia and GFAP+ astrocytes in the $Pax6^{Sey}$ mice relative to controls, suggesting a possible neuroinflammatory response to Pax6 deficiencies.

3.2 Introduction

Aniridia is a panocular disorder characterized by the partial or complete loss of the iris (Glaser et al., 1994; Hingorani et al., 2012; Moosajee M, 2018; Pedersen et al., 2020; Prosser and van Heyningen, 1998; Tzoulaki et al., 2005). Most cases result from heterozygous mutations in the *PAX6* homeobox gene located on chromosome 11p13, which account for approximately 90% of genetic aniridia cases (Daruich et al., 2022; Moosajee M, 2018; Prosser and van Heyningen, 1998; Simpson and Price, 2002; Tzoulaki et al., 2005; Warren et al., 1999; Wawrocka and Krawczynski, 2018; Yasue et al., 2017; Yokoi et al., 2016). *PAX6* itself is a highly conserved transcription factor critical for the regulation of ocular, olfactory, brain, and endocrine development (Daruich et al., 2022; Mi et al., 2013; Samant et al., 2016). In aniridia, *PAX6* deficiency is associated with noticeable hypoplasia or absence of anterior eye regions, but its effects in retinal tissue are subtler and require further investigation (Axton et al., 1997; Bobilev et al., 2016; Glaser et al., 1994; Lee et al., 2008; Lima Cunha et al., 2019; Whitson et al., 2005). Previous studies demonstrate that *PAX6* is necessary for the differentiation and maturation of retinal precursor cells (RPCs) and without its normal expression levels, many RPCs fail to develop into the various retinal subpopulations (Nishina et al., 1999; Remez et al., 2017). Critically, this dosage is required at key stages of pre- and post-natal development, suggesting that misregulation of protein levels at these timepoints may underly a significant amount of developmental damage.

Nevertheless, the effects of *PAX6* mutations on visual health and behavior do not always become apparent until later in life (Cole et al., 2022; Rabiee et al., 2020; Samant et al., 2016). We showed that most of these visual deficits are noticeable even immediately after eye-opening and tend to worsen with age (Cole et al., 2022; Rabiee et al., 2020). This is likely due to the exacerbating effects of glaucoma, such corneal keratopathy, and iris hypoplasia, which often

develop in parallel with severe aniridic symptoms (Cole et al., 2021; Daruich et al., 2022; Netland et al., 2011). A glaucoma diagnosis in human aniridia patients occurs, on average, at 13.6 years of age, well after the usual age of diagnosis for aniridia (mean approx. 22 months) (Netland et al., 2011). During that interval, early elevation in IOP may begin to aggravate existing damage in the retina, further reinforcing the need for early detection, tracking, and mitigation of aniridia phenotypes.

Our previous studies have identified areas of localized damage in the retina and generalized defasciculation of nerve fiber bundles across the retinal surface (Cole et al., 2022; Rabiee et al., 2020). In this study, we aimed to further characterize the defects in retinal structure and vision during postnatal development. Furthermore, we examined the neuroinflammatory response in Pax6-deficient mice.

3.3 Methods and Materials

3.3.1 Mice

For this study we used a small-eye mouse model (*Pax6*^{Sey}) on two different backgrounds: C57Bl/6 (a gift from James D. Lauderdale at University of Georgia to Rob Grainger at UVA), and 129S1/Svlmj1/Svlmj (MMRRC, # 050624-MU) (Hickmott et al., 2018). Heterozygous mutant *Pax6*^{Sey} males were bred with wildtype females to produce litters, which were genotyped according to our published protocol (Cole et al., 2022; Hickmott et al., 2018; Rabiee et al., 2020). All procedures were approved by the UVA Institutional Animal Care and Use Committee and complied with the guidelines of the National Institutes of Health (NIH).

3.3.2 Intraocular Pressure and Visual Acuity

IOP and visual acuity were assessed using our previously published protocols (Chen et al., 2015; Cole et al., 2022; Feng et al., 2013a; Feng et al., 2016; Feng et al., 2013b; Gao et al., 2022a; Rabiee et al., 2020). IOP and acuity were assessed during post-natal days P20-P24 (denoted as P20), P30-P34 (P30), P60-P70 (P60), and P90-P120 (P90).

Briefly, mice were restrained in a plastic sleeve, and a TonoLab rebound tonometer was used to measure the IOP of each eye, with the mean of three measurements per eye being recorded. Visual acuity was assessed using the PhenoSys qOMR system (PhenoSys, GmbH, Berlin, Germany). Mice were adapted to the testing chamber for 2 minutes and then presented with visual gratings at frequencies of 0.05 cyc/deg to 0.5 cyc/deg, increasing in increments of 0.05 cyc/deg. The gratings would regularly alternate between clockwise (left eye driven) and counterclockwise (right eye driven) rotations to account for the acuity of both eyes. The highest frequency that elicited an optomotor response was recorded as the acuity for each eye.

3.3.3 Immunohistochemistry and Confocal Microscopy

Retinas were processed for immunohistochemistry and confocal microscopy according to our previously published protocols (Beckmann et al., 2021; Cole et al., 2022; Grannonico et al., 2021). The first time points (P20 & P30) were combined into one group and referred to as P30, and the last two time points (P60 & P90) were combined and labeled P80 for *ex vivo* analysis. Mice were euthanized (Euthasol; 15.6 mg/mL; Virbac, Greely, CO, USA), and perfused with 4% paraformaldehyde (PFA).

Retinas were whole-mounted or eyes cryo-sectioned at 20 µm thickness prior to processing (Cole et al., 2022; Grannonico et al., 2021). Only sections within 60 µm of the optic

nerve head (ONH) were used for analysis, with the ONH serving as a landmark. For whole-mounts, retinal eye cups were cut into 4 leaflets and cover slipped (Beckmann et al., 2021).

Primary antibodies included anti-RNA binding protein, mRNA processing factor (rbpms, 1:250; Abcam, Waltham, MA), anti-choline acetyltransferase (ChAT,1:250; ThermoFisher Scientific, Waltham, MA), anti-AP2 (1:200, DSHB, Iowa City, IA) anti-glial fibrillary acidic protein (GFAP, 1:200; Abcam, Waltham, MA), anti-ionized calcium binding adaptor molecule 1 (Iba1, 1:250; Abcam, Waltham, MA). 4′ ,6-diamidino-2-phenylindole (DAPI, VECTASHIELD®, Vector Laboratories) was used as a contrast stain to visualize cell nuclei. Sections were imaged using a Zeiss LSM 800 microscope (Carl Zeiss AG, Oberkochen, Germany) (Cole et al., 2022; Gao et al., 2022b; Grannonico et al., 2021).

3.3.4 Quantification

For retinal whole-mounts, the lengths from superior to inferior and nasal to temporal aspects were measured and averaged for each eye (Figure 1B/C). For sagittal thickness measurements, three regions with normal layering were selected within 1000 µm on both sides of the optic nerve head (ONH), for a total of six per retina. The thicknesses of individual sublayers of the retina were measured, including outer nuclear layer (ONL), inner nuclear layer + outer plexiform layer (INL+OPL), and the inner plexiform layer + ganglion cell layer (IPL+GCL). Total thickness was likewise measured from the base of the ONL to the top of the GCL. The means of these six measurements were recorded for each retina.

We identified regions in sagittal retinal sections of distended retinal layers which we termed “hotspots.” These hotspots were defined by aberrant layer thicknesses, and/or rampant disruption of normal soma stacking/organization in INL and ONL. For all retina, hotspots and

normal regions were measured separately (Cole et al., 2022). The hotspot layer thickness measurements were performed as described above and labeled as “hotspot” (hs) regions.

To quantify immunolabeled cells in sagittal sections, two segments of 300 µm length were selected on both sides of the ONH for a total of four segments per retina. Rbpms+ cells (retinal ganglion cells) were counted in GCL+IPL for each segment. ChAT+ cells (cholinergic amacrine) and AP-2+ cells (amacrine) were separately counted in the INL and GCL of each segment.

Quantifications of Iba1+ (microglia) and GFAP+ (astrocytes) in the whole-mounted retina were performed by demarcating three 30,000 μm^2 squares in each leaflet. The three squares were spread between the peripheral, middle, and inner portions of the leaflet (Fig. 6 & 7). The Iba1+ and GFAP+ were counted for each square and the mean of all four leaflets was recorded as the measurement per retina. The mean is reported as cells/mm^2.

3.3.5 Statistical Analysis

Statistical tests were performed using GraphPad Prism 7.0 (Graph Pad Software, San Diego, CA). Multiple samples were compared using one-way ANOVA followed by post-hoc Tukey multiple comparison tests. Results were reported as mean ± standard error of mean (SEM).

3.4 Results

3.4.1 Pax6^{Sey} mice have smaller retinas with increased intraocular pressure.

As shown in Figure 3.1A, *Pax6^{Sey}* mice exhibit a *small-eye* phenotype, which we confirmed by measuring retinal size using whole-mounts (Figure 3.1B). Retinal widths show a significant reduction in eye size among the C57Bl/6 *Pax6^{Sey}* (n=6) with mean P90 widths of 3663.5±309.9 µm as compared to the mean age-matched WT (n=7) widths of 4557.5±125.4 µm ($p<0.01$) (Figure 3.1C). The 129S1/Svlmj strain shows significant differences in eye width as well (WT: 4777.9±77.6 µm, *Pax6^{Sey}*: 4080.9±124.1µm, $p<0.05$, One-way ANOVA with Tukey post-hoc test).

IOP was measured at (Methods 3.3.2) P20, P30, P60 and P90 (Figure 3.2A). C57Bl/6 *Pax6^{Sey}* mice showed significantly higher IOP at P30 with a mean of 19.0±0.5 mmHg (n=32) as compared to a WT mean of 14.5±0.2 mmHg (n=32) ($p<0.0001$, One-way ANOVA with Tukey post-hoc test). IOP elevation is maintained into adulthood, with the *Pax6^{Sey}* genotype of this strain showing a mean IOP of 22.1±0.7 mmHg (n=15) at P90, and P90 WT controls showing a mean of 16.7±0.2 mmHg (n=26, $p<0.0001$). 129S1/Svlmj *Pax6^{Sey}* do not show a difference at P20 (15.3±0.96 mmHg, n=20) or P30 (15.3±0.3 mmHg, n=18) compared to WT controls (P20: 14.8±0.5 mmHg, n=8, p=0.63. P30: 15.0±0.2 mmHg, n=22, p=0.92). At P60, the IOP of 129S1/Svlmj *Pax6^{Sey}* becomes significantly elevated with a mean of 17.7±0.9 mmHg (n=12) and WT controls of the same strain showing a mean IOP of 14.7±0.3 mmHg (n=16, $p<0.05$). The significance becomes greater at P90 in the 129S1/Svlmj *Pax6^{Sey}* with a mean of 18.8±0.5 mmHg (n=15) compared to a WT mean of 14.83±0.3 mmHg (n=12, $p<0.0001$). Our data suggests that C57Bl/6 *Pax6^{Sey}* exhibit higher IOP by P30 while 129S1/Svlmj *Pax6^{Sey}* take until P60 to show a significant increase in IOP.

3.4.2 Visual acuity loss with age in Pax6-deficient mice

Visual acuity was assessed at the same ages as IOP (Figure 3.2B). At P20, C57Bl/6 WT show a mean response of 0.35±0.01 cyc/deg (n=26) which is significantly higher than C57Bl/6 *Pax6*^{Sey} whose mean response was 0.15±0.02 cyc/deg (n=25, $p<0.0001$, One-way ANOVA with Tukey post-hoc test). This deficit is maintained well into adulthood. The 129S1/Svlmj strain also shows a significant deficit by P20, with 129S1/Svlmj WT controls having a mean acuity of 0.41±0.01 cyc/deg (n=18) and 129S1/Svlmj *Pax6*^{Sey} at 0.32±0.01 cyc/deg (n=21, $p<0.0001$). Both C57Bl/6 and 129S1/Svlmj *Pax6*^{Sey} show dramatic deficits in visual behavior at the onset P20 and maintain these deficits with a high degree of variance.

IOP and visual acuity were plotted against each other (Figure 3.2C). When comparing the two, clusters begin to form based on genotype and background. C57Bl/6 WT and 129S1/Svlmj WT both cluster near each other even into adulthood (P90). C57Bl/6 *Pax6*^{Sey} most notably have lower acuity and higher IOP than the other groups. 129S1/Svlmj *Pax6*^{Sey} sits in between these groups, exemplifying milder aniridia phenotypes.

Further investigation of this visual decline was done by following a WT and *Pax6*^{Sey} mouse from both backgrounds from P15 to P120 with regular visual acuity measurements (Supp. 3.1A). These measurements demonstrate a sharp decline in visual acuity for the *Pax6*^{Sey} C57Bl/6 mouse but a more gradual decline for the *Pax6*^{Sey} 129S1/Svlmj when compared to their WT counterparts. Together our results showed that IOP elevation is correlated with the decline of visual acuity with age in *Pax6*^{Sey} mice from both 129S1/Svlmj and C57Bl/6 backgrounds.

3.4.3 Varied Retinal Layer thickness in Pax6-deficient mice.

For the following studies, the first time points (P20 & P30) were combined into one group and referred to as P30, and the last two time points (P60 & P90) were combined and labeled P80. Thickness was measured for each sublayer including the ONL, OPL+INL, IPL+GCL, and total retinal thickness. Overall, we found no significant difference in retinal thickness in *Pax6*^{Sey} mice. However, we observed unevenness of the retinal layer thickness as shown in our previous study showed (Cole et al 2022). Again, we called these local damaged areas hotspots, which exhibited abnormal thickening, curling, and disruption of normal soma density (Supp. 3.2 & Figure 3.3A). At P80, *Pax6*^{Sey} C57Bl/6 mice (n=6) show a mean total hotspot thickness of 312.0±42.4 µm as compared to normal regions (210.3±17.7 µm, n=6, p=0.053, One-way ANOVA with Tukey post-hoc test), while WT hotspots (n=3) have a mean total thickness of 246.1±4.3 µm as compared to their normal regions (245.4±9.1 µm, n=6, p>0.99). The 129S1/Svlmj strain shows similar trends in hotspots, with their *Pax6*^{Sey} (n=5) hotspot mean thicknesses at 236.8±29.0 µm as compared to their normal (n=6) regions (206.6±11.4 µm, p=0.97), and the WT hotspot (n=5) mean thicknesses at 235.2±11.3 µm and their normal WT thicknesses (230.8±6.9 µm, p>0.99). Overall, we observed a high variability of retinal layer thickness with higher standard error (SEM), though the overall changes were not statistically significant.

3.4.4 Neuronal cell-type population density shows high variance in Pax6-deficient mice.

Specific neuronal populations were stained and quantified to assess damage in diseased retinas. Retinal ganglion cells were stained by anti-rbpms as an indicator for RGC health (Figure 3.4, left). C57Bl/6 *Pax6*^{Sey} (n=28) show an insignificant decrease of 21.4±1.4 cells per 300 µm segment as compared to C57Bl/6 WT (n=36), which show an average of 25.9±1.3 cells per 300 µm segment (Supp. 3.3A, p=0.22, One-way ANOVA with Tukey post-hoc test). The 129S1/Svlmj mice do not demonstrate a significant decrease in rbpms-positive cells either but

also appear to trend toward a significant decrease, with 129S1/Svlmj *Pax6*^{Sey} (n=20) and WT (n=20) averaging 20.8±1.3 and 27.7±1.5 cells per 300 µm segment, respectively (p=0.57).

Anti-ChAT was used to stain cholinergic amacrine cells (Figure 3.4, center). Labeled cells were quantified in two separate layers, the INL and the GCL (Supp. 3.3B). C57Bl/6 WT mice (n=24) show an average of 10.4±0.6 and 9.6±0.7 cells per 300 µm segment in the INL and GCL, respectively. C57Bl/6 *Pax6*^{Sey} (n=22) show little difference from the WT controls with 9.7±0.7 and 8.8±0.7 cells per 300 µm segments in the INL and GCL (INL: p=0.99, GCL: p=0.99). 129S1/Svlmj WT mice (n=8) shows an average of 5.8±0.6 cells per 300 µm segment in the INL and 129S1/Svlmj *Pax6*^{Sey} (n=12) have a mean of 10.5±0.8 per 300 µm segment in the INL ($p<0.05$). In the GCL 129S1/Svlmj WT has a mean of 6.1±1.0 per 300 µm segment and 129S1/Svlmj *Pax6*^{Sey} has a mean of 9.0±0.6 per 300 µm segment (p=0.48).

The anti-AP2 antibody was used as a general amacrine marker (Figure 3.4, right). Like the ChAT quantifications, the AP-2 quantification was done independently in the INL and GCL (Supp. 3.3C). Initial counts of INL in the WT C57Bl/6 mice (n=20) yielded a mean of 51.3±3.6 per 300 µm segment, and a GCL mean of 22±1.1 per µm. This does not differ significantly from the normal regions of C57Bl/6 *Pax6*^{Sey} (n=12) mice, whose INL mean was 52.4±3.4 per 300 µm segment ($p>0.99$) and GCL mean was 30.1±1.9 per 300 µm segment ($p>0.99$). The hotspots of *Pax6*^{Sey} did not yield significantly higher AP-2 counts when compared with their normal regions, with an INL mean of 58.4±8.2 per 300 µm segment (p=0.81) and a GCL mean of 57.6±9.2 per 300 µm segment (p=0.99). For 129S1/Svlmj, the INL mean of 129S1/Svlmj WT mice (n=8) was 48.4±3.0 cell per 300 µm segment while 129S1/Svlmj *Pax6*^{Sey} (n=12) has a mean of 39.1±5.0 per 300 µm segment (p=0.98). 129S1/Svlmj WT control GCL mean was 17.1±1.5 per 300 µm

segment while the 129S1/Svlmj *Pax6*^{Sey} has a GCL mean of 18.3±1.7 per 300 µm segment (p=0.88).

Together our analysis of neuronal populations showed that specific cell types did not differ greatly in the *Pax6*^{Sey} mice of both strains compared to their respective controls.

3.4.5 Neuroinflammation was upregulated in Pax6-deficient mice

Two types of glial cells were examined, microglia and astrocytes. Activated microglia density was quantified using the anti-Iba1 antibody (Figure 3.5). For C57Bl/6 WT mice, the Iba1+ density remains consistent across P30 (n=5) and P80 (n=5) age groups at 231.7±5.3 cells/mm^2 and 224.4±6.4 cells/mm^2 (p=0.99). P30 *Pax6*^{Sey} mice (n=5, 315.0±7.8 cells/mm^2) are significantly higher than P30 WTs (p<0.05). The difference in density in P80 C57Bl/6 *Pax6*^{Sey} (n=5) is even greater when compared to WT counterparts (363.9±14.0 cells/mm^2, p<0.001).

Anti-GFAP stains of whole-mounted retinas likewise show a higher density of astrocytes in the inner layers of the retina by adulthood (Figure 3.6). At P30, C57Bl/6 WT mice (n=4) had a mean density of 954.2±35.5 cells/mm^2. C57Bl/6 *Pax6*^{Sey} mice (n=4) were not significantly different from WT controls with a density of 1187.5±45.9 cells/mm^2 (p=0.31). P80 leaflet quantification found that C57Bl/6 *Pax6*^{Sey} retinas (n=2) have a mean density of 1611.1±49.5 cells/mm^2 while WT retinas (n=4) show a mean density of 881.3±27.7 cells/mm^2 (p<0.01).

GFAP+ labeling in Müller glia as seen in sagittal sections also appeared abnormal, suggesting a disruption of normal Müller glia (Supp. 3.4). Together our results showed a greater density of microglia and astrocytes in the RNFL in the *Pax6*^{Sey} mice. These glial cells appeared activated in *Pax6*^{Sey} retinas suggesting inducement of a neuroinflammatory immune response.

3.5 Discussion

3.5.1 Pax6-deficiency impairs ocular development via glaucomatous phenotypes and reduced visual behavior.

Many previous studies identified distinct aniridic deficits in anterior and posterior regions of the eye (Ahmed N R M, 2014; Axton et al., 1997; Bobilev et al., 2016; Chang et al., 2014; Free et al., 2003; Glaser et al., 1994; Hill et al., 1991; Lima Cunha et al., 2019; Shiple et al., 2015; Whitson et al., 2005). As Pax6 is required for normal eye development, these impairments emphasize the necessity of normal protein dosage in maturing tissues (Cole et al., 2022; Daruich et al., 2022; Klimova and Kozmik, 2014; Remez et al., 2017; Simpson and Price, 2002). Limited dosage, therefore, leads to underdeveloped tissues, which manifest the many deleterious symptoms associated with the retina and anterior segment, many of which will impair normal visual health.

Our own findings demonstrate an increased prevalence of glaucomatous damage, presumably from an elevated IOP, a phenotype that appears to manifest following eye opening (approximately P14) and intensifies later in life. More severe aniridia cases such as those in our C57Bl/6 background show pathology as early as P30, while the milder 129S1/Svlmj only showed significant glaucomatous effects as adults (P60). Iris and lens hypoplasias are likely the chief cause of these IOP elevations, which may explain why *Pax6*^{Sey} 129S1/Svlmj mice are slower to manifest, as their anterior segments are noticeably less disrupted than their C57Bl/6 counterparts (Chang et al., 2014; Chen et al., 2011; Feng et al., 2013a; Feng et al., 2013b; Goel et al., 2010).

Heightened IOP has been linked to decreases in visual behavior (Chang et al., 2002; Chen et al., 2011; Cole et al., 2021; Feng et al., 2013a; Feng et al., 2013b; Hood, 2019; Medeiros et al.,

2013; Savinova et al., 2001). This was initially believed to result from reductions in RGC populations, though recent studies show that the relationship between visual acuity and RGCs is not so clear (Cole et al., 2022; Hood, 2019; Medeiros et al., 2013). Still, prolonged exposure to glaucomatous damage does appear to worsen visual acuity beyond the already reduced baseline in subjects suffering from aniridia. Our own previous studies suggest that prolonged exposure to glaucomatous pressures may exacerbate existing damage in retina, thereby explaining the gradual decline in visual acuity (Cole et al., 2022; Cole et al., 2021). The exact relationship between acuity and IOP is not well understood, however, as our current study shows severe acuity deficits in *Pax6*^{Sey} C57Bl/6 mice as early as P20 (Figure 3.3). Most aniridic damage appears well before eye opening, and therefore may alter vision so severely that glaucomatous exacerbation becomes redundant (Ahmed N R M, 2014; Cole et al., 2022; Cole et al., 2021; Glaser et al., 1994; Hill et al., 1991; McCulley et al., 2005; Pedersen et al., 2020).

When observing individual aniridia cases with less initial deficits (Supp. 3.1) the rate of visual decline during post-natal maturation becomes more evident. This reinforces the importance of longitudinal *in vivo* assessments of aniridic symptoms, which is a necessary dimension for future studies and potential therapeutics in patients. The high degree of variance in aniridia phenotypes, even among littermates, may otherwise confound future aniridia studies, especially if reliant to single-timepoint measures or comparisons (Axton et al., 1997; Bobilev et al., 2016; Chang et al., 2014; Fischbach et al., 2005; Glaser et al., 1994; Lima Cunha et al., 2019; Netland et al., 2011; Sannan et al., 2017; Shiple et al., 2015).

3.5.2 Pax6-deficiency leads to upregulated neuroinflammation.

Investigations into aniridia's effect on retinal health have looked primarily on broader morphology, functionality, and retinal nerve fiber layer distribution (Cole et al., 2022; Gregory-Evans et al., 2014; Hickmott et al., 2018; Pedersen et al., 2020; Tremblay et al., 1998). Both sagittal and whole-mount assessments of aniridic retinas have shown areas swollen hotspot damage, which may suggest the presence of a neuroimmune response not unlike that seen in other conditions such as diabetic retinopathy (Bosco et al., 2011; Dixon et al., 2021; Gallego et al., 2012; Kinuthia et al., 2020; Rashid et al., 2019; Tao et al., 2022; Zeng et al., 2005). As there is a clear deficit in visual behavior (Figure 3.2B) and an obvious recruitment of both astrocytes and reactive microglia (Figures 3.5 and 3.6), it can be surmised that *Pax6*-related malformation of the retina leads to a subsequent neuroinflammatory responses.

It is well-established that chronic retinal degeneration is due, in part, to pro-inflammatory cytokines and the recruitment of reactive microglia in the diseased retina (Kumari et al., 2022; Rashid et al., 2019). A higher density of these cells will result in a greater release of cytotoxic compounds that will further degenerate surrounding retinal tissue. In recent years, the role of microglia in neurogenesis and development has also been the subject of many studies (Bosco et al., 2011; Dixon et al., 2021; Gallego et al., 2012; Puyang et al., 2016; Rashid et al., 2019; Tao et al., 2022). Microglia are now known to be an integral part of healthy retinal development and maturation, particularly in the regulation of apoptosis through control of caspase cascades (Dixon et al., 2021). Their role in programmed death and neural refinement would therefore be disrupted when other critical developmental pathways are impaired, such as those involving Pax6 and its targets. The disruption seen in aniridia represents a multitude of development failures not only in retinal maturation but in their possible interactions with microglia.

Astrocyte activation is yet another known component of gliosis in degenerating retina and has been cited as a critical detriment to retinal health in many chronic conditions such as retinitis pigmentosa and retinal injury (Fernández-Sánchez et al., 2015; Luna et al., 2010). With both macroglia and microglia activation in aniridia models, it is no wonder, then, that normal retinal function is severely impaired in cases where layering and retinal morphology is especially disrupted.

Much remains unclear in the relationship between retinal glia and Pax6-deficiencies. Whether their recruitment is a common phenomenon expected from any retinal insult, or that some more immediate, intrinsic link exists between *Pax6* expression and glia recruitment, and activation remains to be seen.

3.5.3 Conclusion

Our findings suggest that genetic cases of aniridia in a *Pax6*^{Sey} mouse model exhibit a wide range of phenotypes, not just between genetic strains but also within genetic strains. In many cases retinal layering is disrupted in localized areas with intense retinal disorganization and greatly varied retinal cell subtype densities. What is consistent, however, is the pronounced recruitment of retinal astrocytes and microglia throughout afflicted retina. Further study is needed to understand the relationship between Pax6 deficiency and gliosis, which will provide avenues for possible therapeutics and interventions.

.

3.6 Figures

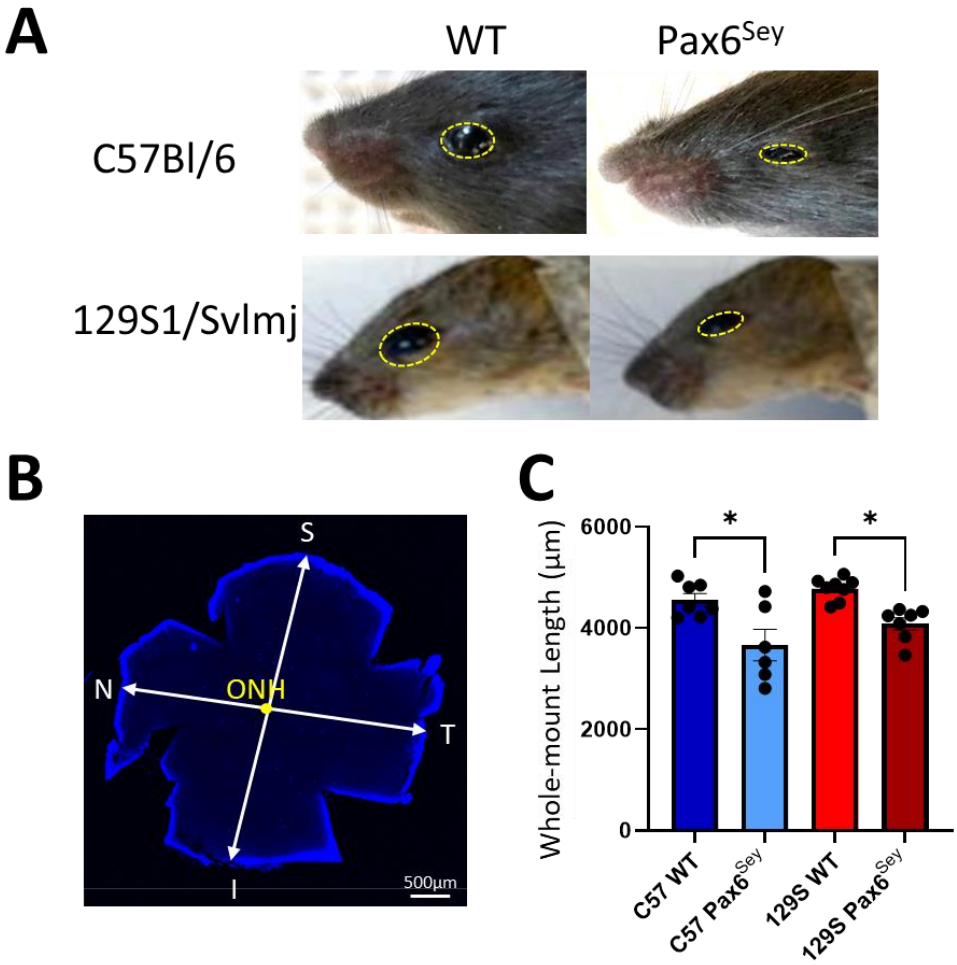

Figure 3.1 *Pax6*^{Sey} phenotype results in smaller retinas.

A) *Pax6*^{Sey} in both 129S1/Svlmj and C57Bl/6 exhibit *small-eye* phenotypes. Yellow dashed lines highlight the ocular anatomy. B) Example of whole-mounted retina stained with DAPI showing the retinal length measurements along the nasal-temporal and superior-inferior directions (white arrowheads) (S: superior, T: temporal, I: inferior, N: nasal). C) *Pax6*^{Sey} mice in both backgrounds show significantly smaller whole-mount lengths compared to their WT counterparts. *: $P < 0.05$ in one-way ANOVA post-hoc Tukey's test.

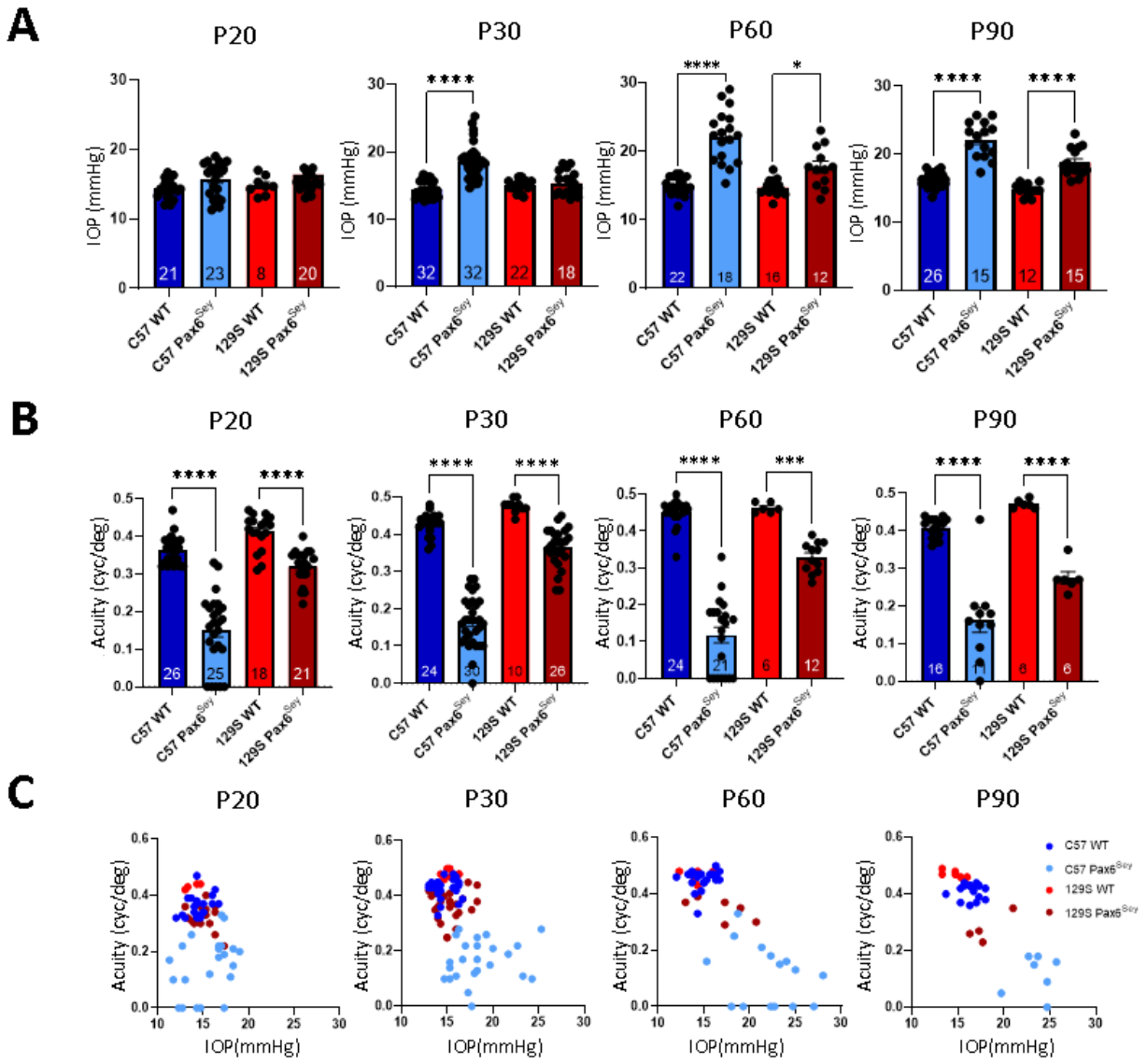

Figure 2. Intraocular pressure (IOP) increases, and visual acuity decreases significantly with age in *Pax6*^{Sey} mice. A) *Pax6*^{Sey} C57Bl/6 mice show a significant increase of IOP by P30; *Pax6*^{Sey} 129S1/Svlmj mice show a significant IOP increase by P60. B) Visual acuity was significantly decreased in *Pax6*^{Sey} of both C57Bl/6 and 129S1/Svlmj backgrounds at P20. C) Plots of acuity versus IOP. *: $P < 0.05$, ***: $P < 0.001$; ****: $P < 0.0001$ in one-way ANOVA post-hoc Tukey's test.

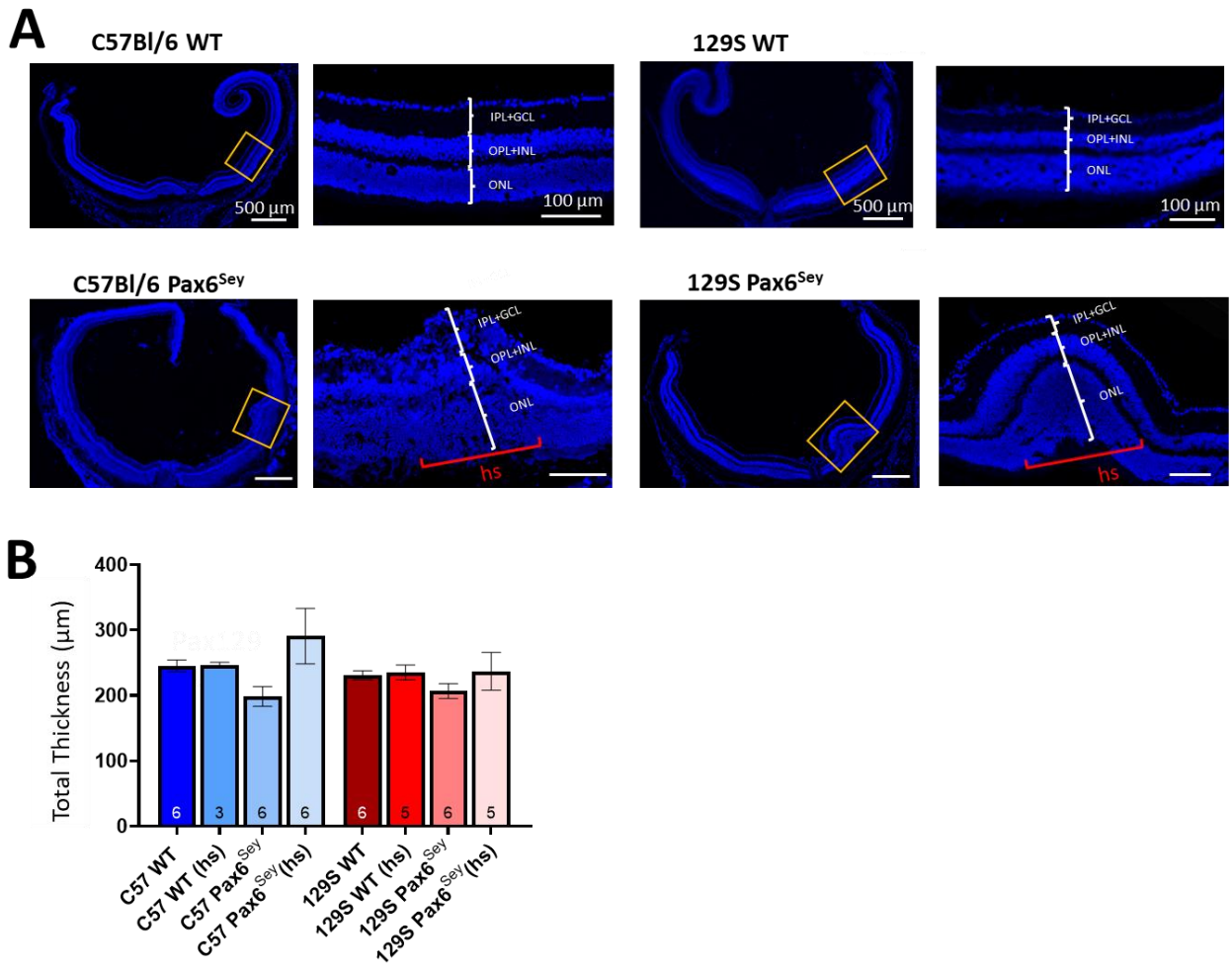

Figure 3. Abnormal layer organization in *Pax6*^{Sey} mouse retinas. A) Layer disorganization was present in *Pax6*^{Sey} mice of both genetic backgrounds. Full sagittal retina sections are shown as well as high magnification of normal regions and hotspots, the localized damages. B) Quantification of total retinal thickness. One-way ANOVA with Tukey post-hoc tests showed no statistically significant changes among different groups. Sample numbers are shown within the bars.

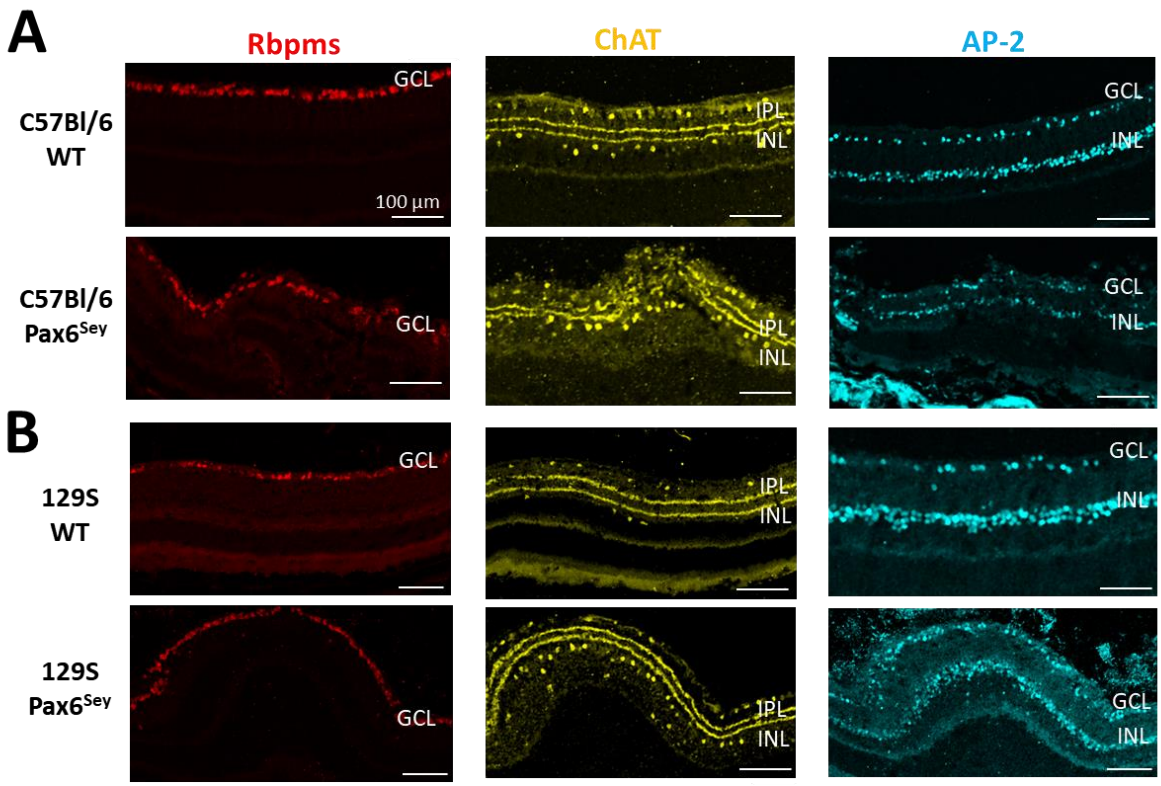

Figure 3.4 Retinal subpopulations show varied density in *Pax6*^{Sey} mice. A) Confocal imaging of retinal neuronal cell-type markers Rbpms, ChAT, and AP-2 in C57Bl/6. B) Confocal imaging of neuronal cell-type markers Rbpms, ChAT, and AP-2 in 129S1/Svlmj1/Svlmj.

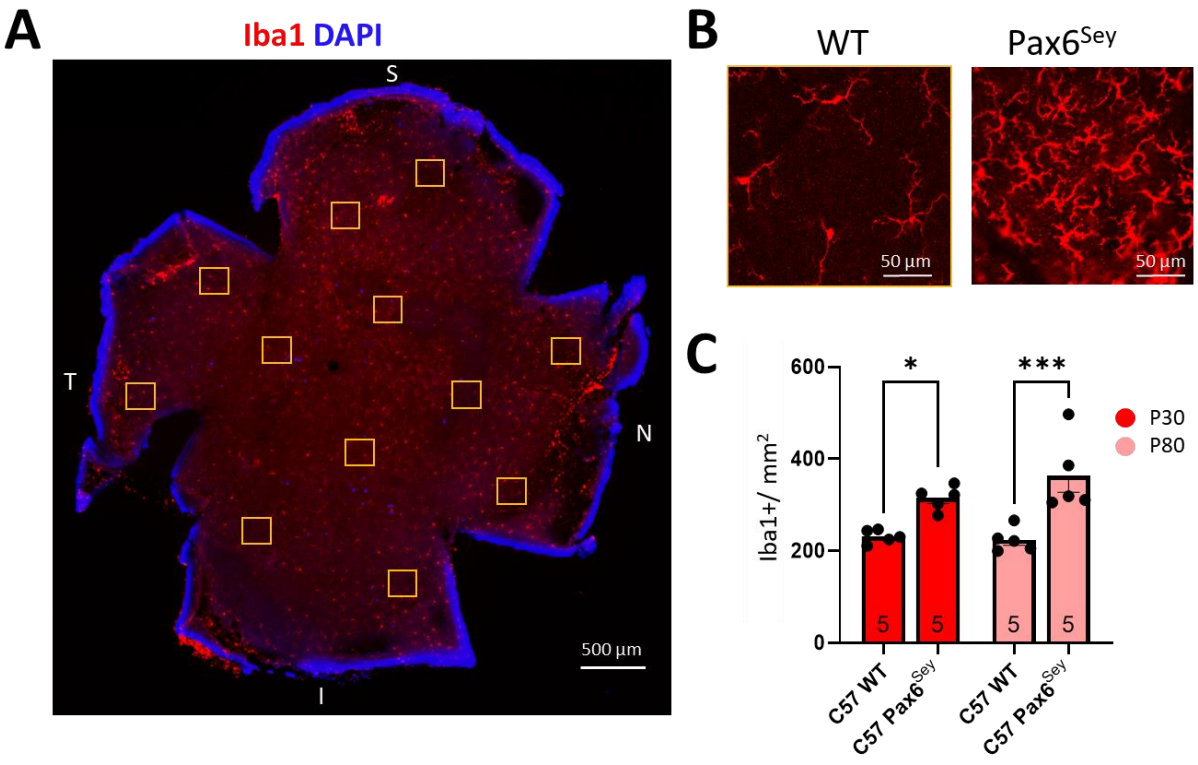

Figure 5. C57Bl/6 *Pax6*^{Sey} mice exhibit increased density of activated (Iba1+) microglial cells.

A) Confocal imaging of a whole-mounted retina immuno-stained with Iba1 (red) and DAPI (blue). S: superior, T: temporal, I: inferior, N: nasal. B) Magnified areas of quantification show an increased density of Iba1+ cells in C57Bl/6 *Pax6*^{Sey} mice compared to WT. C) Quantification of cells with Iba1+ staining at P30 (dark red) and P80 (light red). Each point represents one eye for each mouse. *: $P < 0.05$, ***: $P < 0.001$ in one-way ANOVA post-hoc Tukey's test.

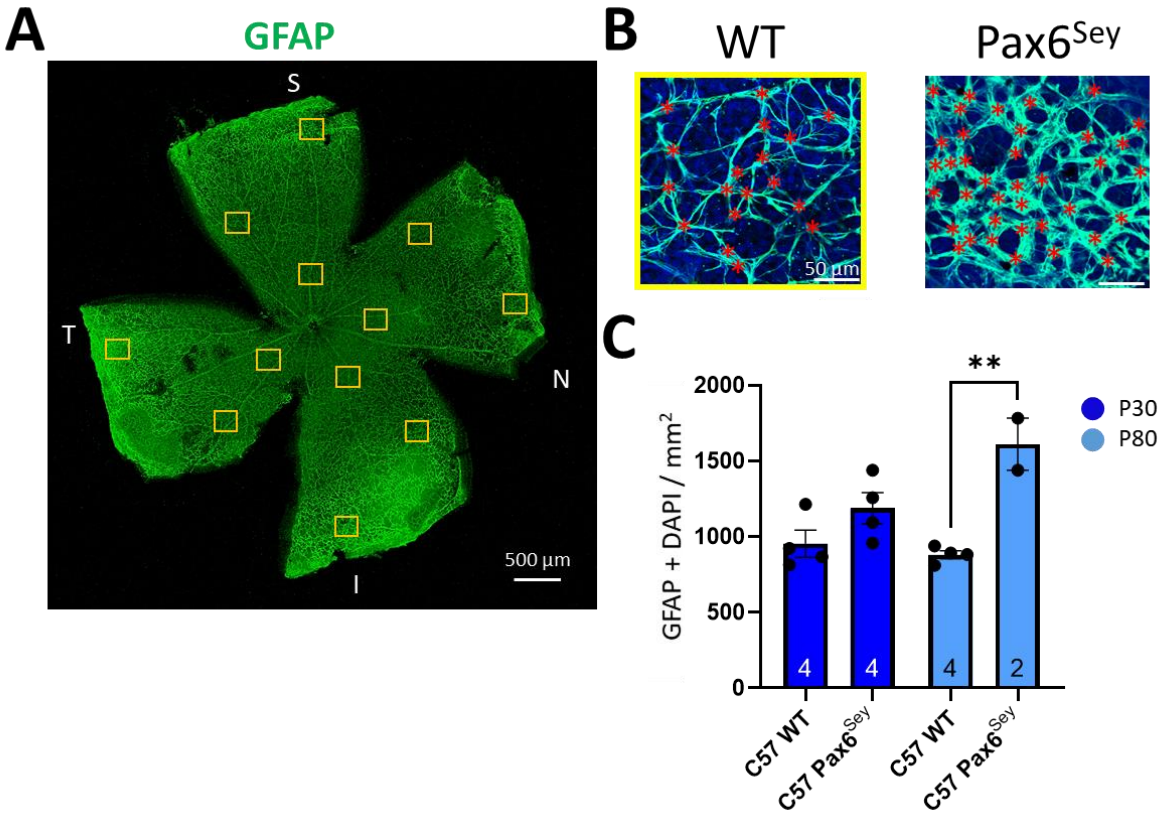

Figure 6. C57Bl/6 *Pax6*^{Sey} mice also exhibit an increased density of astrocytes. A) Confocal imaging of whole-mounted retina immuno-stained with GFAP (green), a marker for astrocytes in the superficial layer of the retina. S: superior, T: temporal, I: inferior, N: nasal. B) Two magnified images have an area of 30,000 µm^2 used for cell counting. C) Quantification of cells with GFAP+ staining above the GCL at P30 (dark blue) and P80 (light blue). Each point represents one eye for each mouse. **: $P < 0.01$ in one-way ANOVA post-hoc Tukey's test.

3.7 Supplemental Figures

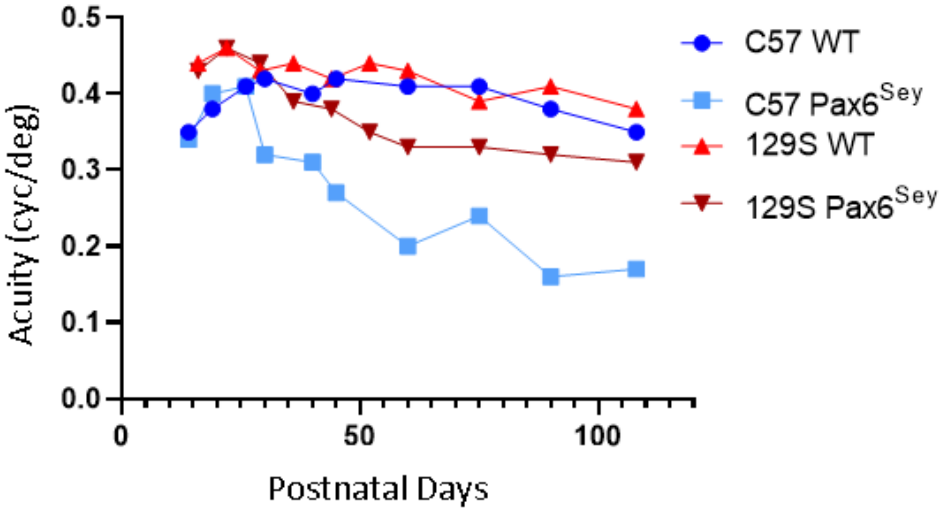

Supplemental 3.1. Longitudinal assessment of acuity shows varying rates of decline in *Pax6*^{Sey} mice of different backgrounds. Graph of individual mice from each of our experimental backgrounds from P20 to P120. C57Bl/6 *Pax6*^{Sey} shows sharpest decline at ~P30. 129S1/Svlmj *Pax6*^{Sey} shows more gradual decline compared to WT controls.

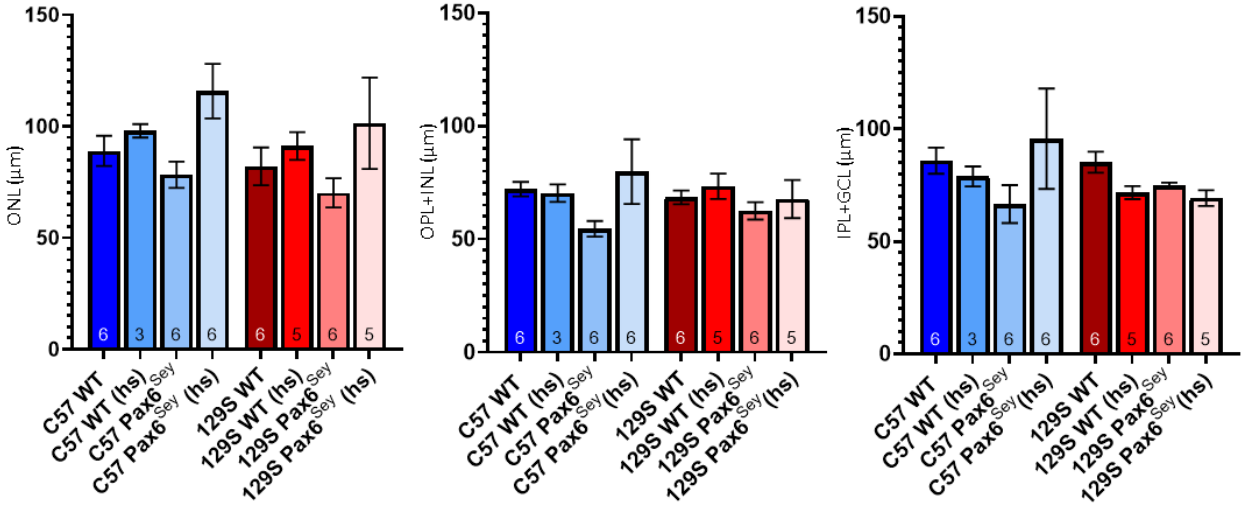

Supplemental 3.2. Individual layer thicknesses of *Pax6*^{Sey} mice show pronounced variability. Measures of outer nuclear layer (ONL), outer plexiform layer + inner nuclear layer (OPL+INL), and inner plexiform layer + ganglion cell layer (IPL+GCL). Layer thickness variability is so high, especially in hotspots (hs), that no significant differences in thickness could be determined.

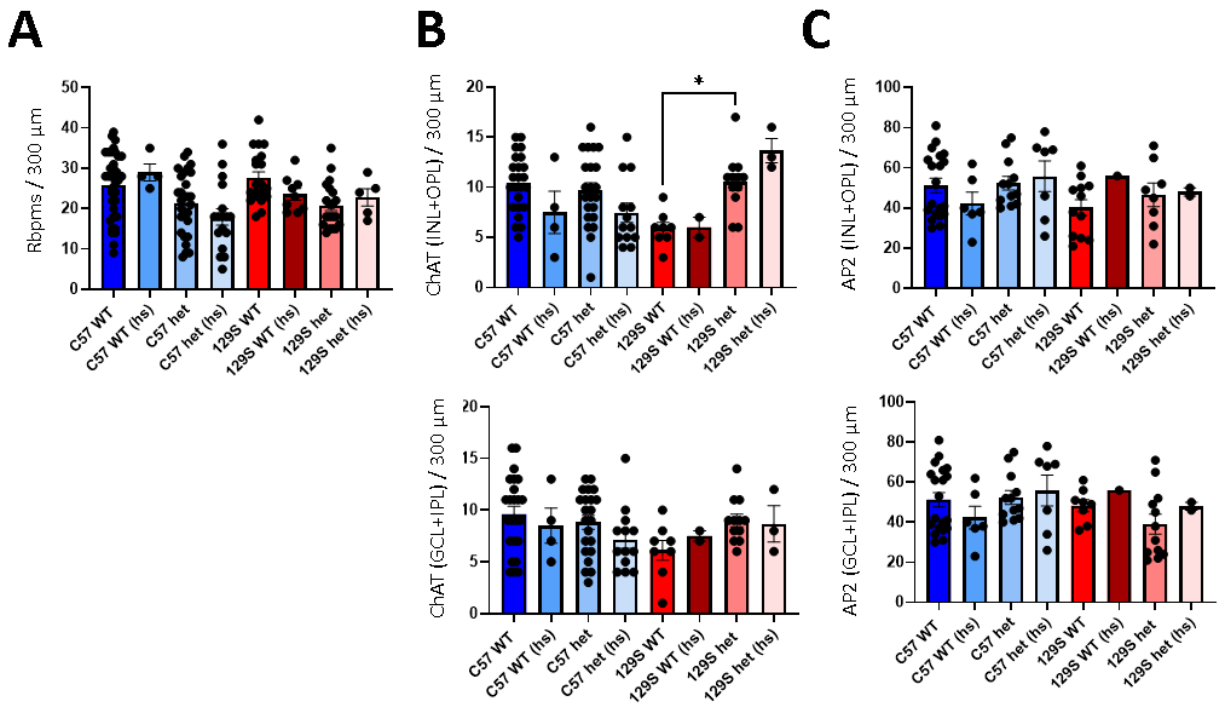

Supplemental 3.3. Cell density in 300 µm segments shows high variability in retinal subtypes. A) Quantification of sagittal anti-rbpms stainings in all four experimental groups, including hotspots (hs), high variability yielded no significant differences in RGC density. B) Quantification of anti-ChAT labeled cholinergic amacrine cells in both INL+OPL, and GCL+IPL. Only significant difference found between normal regions of 129S1/Svlmj WT and 129S1/Svlmj *Pax6*^{Sey} in INL+OPL. C) Quantification of anti-AP-2 labeled amacrine cells in INL+OPL and GCL+IPL found no significant difference in cell density. *: P<0.05

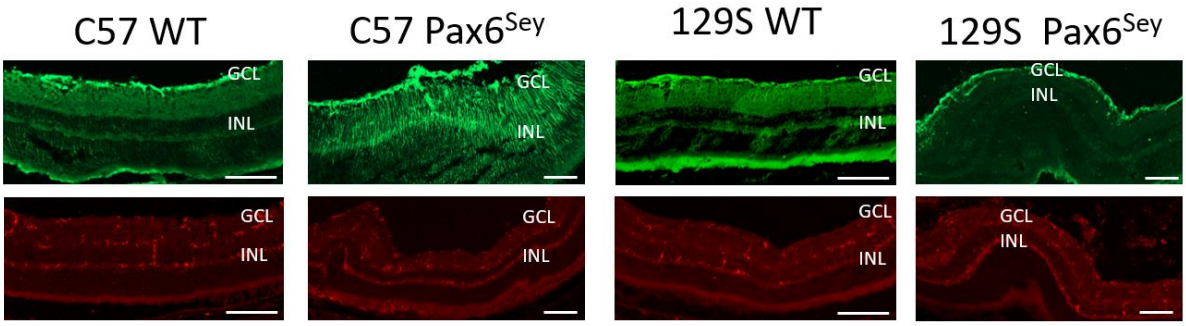

Supplemental 3.4. Sagittal view of Iba1+ and GFAP+ cells in *Pax6*^{Sey} retina shows further evidence of tissue dysfunction. Top row shows GFAP+ labeled end-feet of Müller glia. *Pax6*^{Sey} retina shows more diffuse labelling, possibly due to citrinullation, another indicator of retinal disruption. Bottom row shows Iba1+ microglia like those shown in Figure 3.5.

Chapter 4. Deficient Pax6-dosage in developing eyes leads to varying retinal abnormalities.

4.1 Introduction

Aniridia is a challenging developmental eye disorders to treat, as its reliance on normal Pax6-dosage during pre-natal and post-natal stages of development introduces many obstacles to drug and genetic therapies (Bobilev et al., 2016; Cole et al., 2022; Cvekl et al., 2004; Gregory-Evans et al., 2014; Rabiee et al., 2020; Sannan et al., 2017). It is well-established that many of the retinal defects caused by mutations in the *PAX6/Pax6* gene are present at birth, and even immediate post-eye-opening drug application cannot fully reverse this damage (Cole et al., 2022; Gregory-Evans et al., 2014; Rabiee et al., 2020; Wang et al., 2017). This is further complicated by a highly variable set of phenotypes, which can range from near-normal eye development to complete anophthalmia (Axton et al., 1997; Bobilev et al., 2016; Cole et al., 2022; Ellison-Wright et al., 2004; Glaser et al., 1994; Tzoulaki et al., 2005). The subtle cellular and genetic dictations of these variations are not well-understood and will likely remain the focus of much ongoing study for years to come. It is important to understand how the disease interferes with normal development, and how these various factors can be subsequently addressed in novel therapies.

Debate over the etiopathogenesis of the disease revolves around three primary hypotheses: 1) aniridia is a severe manifestation of iris coloboma, 2) aniridia arises to disruption in the optic vesicle rim development of the neuroectoderm between weeks 12 and 14 of gestation, 3) aniridia arises from failed migration of mesenchymal elements during the second month of gestation (Beauchamp and Meisler, 1986; Nelson et al., 1984). Beauchamp et al. also believed that iris and other ocular hypoplasias could result from irregularities in apoptosis and

tissue remodeling (Beauchamp and Meisler, 1986). These theories all point to very early stages of development, well-before the eye formation, wherein numerous epistatic factors could disrupt tissue formation in the nascent eye cup, compounding and accruing dysplastic phenotypes that result in the highly variable symptoms observed in patients (Beauchamp and Meisler, 1986; Chang et al., 2014; Cole et al., 2021; Cvekl et al., 2004; Klimova and Kozmik, 2014; Lima Cunha et al., 2019; Nishina et al., 1999; Pedersen et al., 2020). The timing of diagnosis and treatment is therefore critical in clinical cases, and to better define those dynamics, we must ensure that proper methods and models are used in our translational research.

4.2 *Pax6* expression in developing eyes

Investigations into *Pax6* in developing murine tissues showed ample expression in the optic sulcus, optic vesicle, neuroectoderm, and later in the inner cup, lens, and cornea (Nishina et al., 1999; Walther and Gruss, 1991). This correlates with post-natal *ex vivo* findings of regions most disrupted in heterozygous *Pax6*^{Sey} mutants (Cole et al., 2022; Cole et al., 2021; Gregory-Evans et al., 2014; Hickmott et al., 2018; Hill et al., 1991; Rabiee et al., 2020; Wang et al., 2017). Ocular organogenesis begins around day 22 of gestation with the formation of the optic sulcus, which is pushed laterally to form the optic vesicle. It is here where *PAX6* show anterior-posterior gradient of expression, with its highest concentrations in the optic vesicles and surrounding neuroectoderm, thus defining the central nervous system alongside other necessary txn factors. Subsequent activation of genes in the invaginated neuroectoderm include those responsible for significant eye factors like crystalline, r-cadherin, and rhodopsin, among others (Cvekl et al., 2004; Sheng et al., 1997; Stoykova et al., 1997). Later, optical vesicles are brought closer to the lens placode, allowing for integration of lens development within the eye itself, a process that

requires much PAX6 to ensure normal lens growth and later separation from surrounding surfaces. It at this stage that the hypoplasia of the lens is most likely to occur, and thus becomes a defining component of the mouse *Pax6*^{Sey} models (Daruich et al., 2022). It is also during this stage that aberrant lens stalks form cornea, preventing complete separation of the lens from both the retina and cornea (Hanson, 2003; Hanson et al., 1994). Nishina et al. found similar expression levels in the proliferating regions of the developing conjunctival epithelia, lens, and eye cup (Nishina et al., 1999). Disruption of retinal morphology appears linked to mitotically active inner layers of developing eyes, particularly retinal generation of RPCs (Nishina et al., 1999) and functions alongside *Mitf* at the fringes of the outer retina to induce development of retinal pigment epithelium (Raviv et al., 2014). Reduced levels of PAX6 results in abnormal patterning and migration of these early cells, particularly into the different cell types that will later form the layers of the inner and outer retina (Shaham et al., 2012). What remains unclear, however, is precisely how this stunted maturation leads to the aberrant morphology seen in severely aniridic retina (Fig 2.2 and Fig 3.3). This may arise from mechanical pressures of other underdeveloped regions, especially the anterior segment. Evidence indicates that PAX6 is necessary for lens separation from the surface ectoderm (Ashery-Padan et al., 2000; Daruich et al., 2022). This may cause the reported retinal detachment and hypoplasia of the optic nerve head, as these tissues are physically pulled from the eye cup by the attached lens in the absence of PAX6's promotion of separating factors (Cole et al., 2022; Gregory-Evans et al., 2014; Katagiri et al., 2017; Nishina et al., 1999).

Aniridia has also shown to inhibit proper differentiation of anterior tissues necessary for trabecular meshwork and corneal stroma from the migrating neural crest cells (Churchill and Booth, 1996; Glaser et al., 1994; Hickmott et al., 2018; Lee et al., 2008; Nishina et al., 1999;

Samant et al., 2016). PAX6's presence in developing mesenchymal tissue is also evident, particularly in the activation of adhesion molecules such as N-CAM (Holst et al., 1997; Tyas et al., 2003). But the degree to which these contribute to later neural/retinal disruption remains unclear, particularly in later stages of cell maintenance, pruning, maturation, and renewal. This effect is much more evident in self-repairing tissues such as cornea and lens and may explain why current anti-aniridic drug therapies show greatest efficacy in mitigating anterior eye defects such as their reduction of aberrant corneal thickness (Cvekl et al., 2004; Rabiee et al., 2020; Shaham et al., 2012; Wang et al., 2018; Yasue et al., 2017).

Though *PAX6* is expressed in both inner and outer neuroblastic layers early in development, Nishina et al. found its expression isolated to the ganglion cell layer and inner nuclear layer at 21-22 weeks (Nishina et al., 1999). Our own work demonstrates the high variation of the RGC and amacrine cell populations of aniridic mice in these regions, suggesting a possible disruption of the migration and specification of RPCs (Cole et al., 2022). Arresting Pax6-dosage may therefore cause high-density masses of undifferentiated cells acting as nucleating points of unmatured RPCs, which then accumulate. These could be the so-called "hotspots" we've described previously (Chapters 2/3). This might also explain why certain markers for amacrine and retinal ganglion cells do not show significantly higher or lower counts in retinal *Pax6*^{Sey} retinal tissue, as many of the amassed somas are actually undifferentiated RPCs that do not express the relevant subtype-specific markers necessary for labeling (Fig 2.3 and 3.4). Future retinal stains using RPC markers such as anti-Rx1, anti-Lhx2, or anti-Sox2 might provide insights into this theory (Agathocleous and Harris, 2009).

How these various developmental pathways are disrupted with reduced *PAX6* expression remains unclear. PAX6 has hundreds of known targets in the eye alone, meaning that its impact

on subsequent, downstream pathways may magnify many times over if its normal dosage is disrupted (Lima Cunha et al., 2019). Other homeobox genes are almost certainly involved in these pathways, both as regulators and targets of *PAX6*. Most notable of these components are other members of the paired box (*PAX*) and the *SRY*-related HMG-box (*SOX*) families (Fischbach et al., 2005; Hall et al., 2019; Lee et al., 2008; Netland et al., 2011). Azuma et al., for example, found that reduction in transcriptional targeting of *PAX6* led to upregulation of *PAX2*, a known repressor of *PAX6*, which increased overall aniridic symptoms, including optic nerve malformations (Azuma et al., 2003). It should also be noted that *PAX6* is a self-regulating gene, and thus, limited dosage further compounds its reduced expression (Lima Cunha et al., 2019). These are but two examples of the complex, interconnected regulatory pathways of *PAX6* and its concert genes. Mapping of these pathways would provide a more comprehensive framework for understanding aniridia's genetic causes, and how the interactions of *PAX6* and its downstream pathways impact normal and diseased retinal development.

4.3 Mouse Models of Aniridia

Various models have been employed to study the origins and progression of aniridia. While most early genetic studies relied on a combination of rodent, xenopus, and Drosophila, the field has largely shifted to solely mammalian systems as these better reflect the disease in humans (Cole et al., 2022; Hickmott et al., 2018; Nishina et al., 1999; Sheng et al., 1997). Human subjects offer the most consistently translational basis of study, but mouse models allow for a larger, more easily manipulated sample of aniridia cases that can be studied in a variety of experimental settings (Beckmann et al., 2021; Feng et al., 2016; Graw et al., 2005; Hickmott et al., 2018). Mice are not a perfect system, however. For one, mouse vision is quite inferior to humans, and

there are many differences in ocular anatomy between the two. Perhaps most notable is that mice lack a fovea, an area commonly affected in human patients (Lee et al., 2008; Lima Cunha et al., 2019; Netland et al., 2011; Prosser and van Heyningen, 1998; Yokoi et al., 2016). Similarly, mouse lenses take up a substantially larger volume of the eye than in humans (Geng et al., 2011). This may contribute to the higher incidence of microphthalmia in the popular *small-eye* mouse models of aniridia (Cole et al., 2022; Graw et al., 2005; Gregory-Evans et al., 2014; Hickmott et al., 2018; Rabiee et al., 2020; Wang et al., 2017). Though microphthalmia has been reported in human cases, it does not show nearly as high of incidence as in aniridic mice (Henderson et al., 2007; Lima Cunha et al., 2019). While lens hypoplasia is common in both organisms, reduction of mouse lens size is likely to have a greater impact on their overall ocular size, whereas this reduction is almost negligible in humans (Henderson et al., 2007; Tzoulaki et al., 2005).

When considering the range of mutations responsible for aniridia in humans, it is likewise important to induce similar missense, frameshift, or nonsense mutations in mouse models (Cole et al., 2022; Gregory-Evans et al., 2014; Hickmott et al., 2018; Pedersen et al., 2020; Rabiee et al., 2020; Wang et al., 2017). Heterozygous mutant small-eye models (Pax6Sey) have been a particular favorite among researchers for their relatively close reflection of severe, late-stage human aniridia phenotypes, including heightened IOP, lowered visual acuity, dampened functional activity, and severe malformation of anterior and posterior regions (Cole et al., 2021; Hickmott et al., 2018). This model has presented some challenges, as those mutants with a C57Bl/6 background are known to exhibit more extreme, highly variable phenotypes, some of which confound measurements of the aforementioned parameters (Cole et al., 2021). Hypoplasias in these mice varies even among littermates and is often asymmetric in individual mice with some subjects exhibiting total anophthalmia in one or both eyes (Cole et al., 2021;

Hickmott et al., 2018). In these cases, only the mice with moderate phenotypes can be used for both *in vivo* and *ex vivo* studies (see Chapters 2 and 3).

The intensity of these phenotypes, however, are not governed solely by single-point or frameshift mutations. Hickmott et al. showed that *Pax6*^{Sey} mice of different genetic backgrounds such as 129S/Svlmj, C57Bl/6, and a hybrid B6129F1 showed varying degrees of eye weight, IOP, visual acuity, retinal/corneal thickness, and Pax6 mRNA levels despite these mice containing identical nonsense mutations (Hickmott et al., 2018). These differences, they theorized, likely arise from background-specific phenotypes reinforced by inbreeding. Homozygous loci are retained consistently across all breeding pairs, thereby eliminating the genetic diversity in free-breeding environments that might dampen associated phenotypes (Hickmott et al., 2018; Keane et al., 2011). 129S/Svlmj, for example, exhibits far milder aniridia phenotypes than their C57Bl/6 counterparts (See Chapter 3). 129S/Svlmj are known to show higher visual acuity than C57Bl/6 in normal conditions, so it makes sense that they might not show as pronounced visual deficits when suffering from aniridia (Abdeljalil et al., 2005). The hybrid B6129F1 mice naturally showed phenotypic severity between that of the C57Bl/6 and 129S/Svlmj backgrounds from which they are derived. Balb-c albino mice, meanwhile, are known to have significantly worse vision than other backgrounds, a fact that can be further exacerbated by glaucoma and anterior segment defects (Cole et al., 2022; Rabiee et al., 2020). Handling, rearing, and other environmental factors likely also contribute to the diversity of phenotypes, though these are relatively minor when compared to the epistatic influences and other intragenomic regulations of PAX6 pathways (Hickmott et al., 2018).

4.4 Aniridia pathology, epidemiology, and prognosis

As a dominant autosomal genetic disorder, classical aniridia poses a great risk to visual health in families where at least one parent carries a heterozygous *PAX6* mutation (Ahmed N R M, 2014; Bobilev et al., 2016; Hingorani et al., 2012; Moosajee M, 2018; Nelson et al., 1984; Samant et al., 2016). While the disease may arise sporadically through missense, frameshift, or other mutations, its incidence is chiefly heightened via familial inheritance and shows complete penetrance (Axton et al., 1997; Bobilev et al., 2016; Glaser et al., 1994; Hingorani et al., 2012; Netland et al., 2011; Sannan et al., 2017). Currently, the disease arises in approximately 1 in every 100,000 individuals, and is typically seen in one of three diagnostic settings: 1) lone aniridia cases, 2) WAGR syndrome, 3) Gillespie syndrome (Daruich et al., 2022; Fischbach et al., 2005; Hall et al., 2019; Nelson et al., 1984). The latter two diseases involve larger deletions or disruptions on chromosome 11 and may involve the loss of function of numerous genes (Nelson et al., 1984; Prosser and van Heyningen, 1998; Samant et al., 2016; Tzoulaki et al., 2005; Yokoi et al., 2016). In the latter two conditions, aniridia is often accompanied by conditions in the urinary system (Wilms tumor, genitourinary abnormalities), motor dysfunction, and mental retardation (Fischbach et al., 2005; Hall et al., 2019; Lee et al., 2008). Isolated cases of aniridia have also been linked to higher incidence of obesity (Netland et al., 2011), and recent comparisons of lone aniridia cases and WAGR syndrome have found the latter to exhibit significantly lower visual acuity (Krause et al., 2023). It can be concluded that broader genetic disruptions also compound aniridia phenotypes, further complicating potential research and therapies.

Diagnosis of aniridia is typically perfunctory, as iris hypoplasia is usually a clear indicator of the condition, allowing for an early mean age of 22 months for diagnosis (Netland et al., 2011). Elements of the iris are, however, often still present, even if in a more rudimentary,

unmatured form. Other common indicators of aniridia include Peter's anomaly, an opaque occlusion at the center of the cornea, as well as various corneal keratopathies, though these only become noticeable later in life (Chang et al., 2014; Hanson et al., 1994; Lee et al., 2008; Netland et al., 2011; Shiple et al., 2015). Vasculature and ciliary bodies are often still present, and the angle leading to Schlemm's canal can be alternately uninhibited or blocked, the latter possibly contributing to later pathogenesis of glaucoma (Beauchamp and Meisler, 1986; Bobilev et al., 2016; Hill et al., 1991; Hingorani et al., 2012; Lee et al., 2008; Lima Cunha et al., 2019; Samant et al., 2016; Yokoi et al., 2016). Ultrasound evidence of irregular strands from the iris stroma sticking to the angle walls and obscuring trabecular meshwork further supports this notion (Okamoto et al., 2004).

More recently, classical aniridia cases have been clinically defined by the presence of foveal hypoplasia, as this it arises very early in childhood, often before other major symptoms (Daruich et al., 2022). This, in addition to observed hotspots, retinal detachment, and layer disorganization indicates a pronounced, permanent detriment to visual health that will worsen with age (Axton et al., 1997; Bosco et al., 2011; Cole et al., 2022; Gregory-Evans et al., 2014; Hickmott et al., 2018; Rabiee et al., 2020). Identification of these foveal disruptions must rely on viable, non-invasive retinal imaging techniques such as optical coherence tomography (Holmström et al., 2010). OCT has become a mainstay in ophthalmological diagnostics over the last few decades. Most notably, the novel Visible Light OCT (Vis-OCT) is especially adept at imaging retinal layers and fovea, providing a far greater resolution than previous infrared-based devices (Beckmann et al., 2021; Grannonico et al., 2021; Miller et al., 2020). Human foveal hypoplasia can more easily be recognized by Vis-OCT, as it is able to image at a substantially higher resolution than the more common infrared form (IR-OCT) (Beckmann et al., 2021;

Grannonico et al., 2021; Miller et al., 2020). Additionally, recent techniques in Vis-OCT fibergram compositing can produce reliable reconstructions of the RNFL. This could provide a much-needed *in vivo* route for diagnosing and tracking the reported thinning of RGC axon bundles in aniridic retina (Cole et al., 2022; Grannonico et al., 2021). There are some potential caveats, though. As with any *in vivo* retinal imaging technique, visualization requires clear access through the cornea and lens, both of which are commonly obscured in aniridia.

Our own attempts to use Vis-OCT on C57Bl/6 *Pax6*^{Sey} mice proved inconclusive as their severe anterior and posterior segment defects prevented adequate imaging, both via obstructions in the anterior segment and the rampant curling/distending of retina. Without a relatively smooth retinal surface in the eye cup, the Vis-OCT laser was unable to digitally reconstruct the retinal layers. When using the milder 129S/Svlmj *Pax6*^{Sey} we were faced with different problems, namely a pronounced nystagmus effect, which, though common in aniridic mice, was not previously reported in this strain (Hickmott et al., 2018). The constant shaking of the eye was not dampened by our anesthesia (ketamine, 100 mg/kg, Kataset, Zoetis; NADA no. 043-304, and xylazine, 8 mg/kg, AnaSed, Akorn; NADA no. 139-236) (Grannonico et al., 2021). As such, Vis-OCT needs further optimization before it can be employed to diagnose and track foveal hypoplasia, and RNFL disruption in aniridia cases. Current development of the human Vis-OCT may yield better results, particularly in human subjects where anterior and posterior deficits are not as severe (Grannonico et al., 2021; Miller et al., 2020; Shu et al., 2017).

In all studies, however, the precise prognosis and progression of the disease is highly dependent on individual factors. Treatment, therefore, requires highly specific parameters for individuals to best mitigate the progressing symptoms and their contributions to visual decline.

4.5 Retinal damage in Pax6-deficient eyes

Recent interest in aniridia's retinal effects has led to several interesting discoveries, namely in retinal morphology, functional outputs, and neuroimmune response (Cole et al., 2022; Gregory-Evans et al., 2014; Rabiee et al., 2020; Wang et al., 2017). In trying to understand these effects, it is important to understand the relevant experimental methods. Prior investigations have already correlated *Pax6* expression levels with the mitotically active regions of the retina (Nishina et al., 1999; Tao et al., 2020; Yasue et al., 2017). Coupled with the fact that *PAX6* is a known regulator of proliferation and maturation for various neural and glial-defined cells, altered dosages of PAX6 protein will fundamentally disrupt normal development of retina (Nishina et al., 1999; Remez et al., 2017). Meng et al. found that suppression of *PAX6* led to unhindered proliferation and inhibited apoptosis in retinoblastomas, further enforcing *PAX6*'s necessity as regulator of cell populations in developing retina (Meng et al., 2014). This function has led to some concerns of oncogenic potential (Maulbecker and Gruss, 1993).

Sagittal views of retina clearly show the distended, curling, often highly disorganized regions in what we call hotspots (Cole et al., 2022). Somas in the INL and ONL of WT mice tend to stack in even, highly organized columns (Fig. 2.2 and 3.3). Hotspots of *Pax6*^{Sey} retinas lose this organization completely, instead clumping somas together in sporadic, densely packed masses (Fig. 2.2 and 3.3). Thickness of these layers also appears to increase substantially in these hotspots, a fact we initially confirmed in our total thickness measures of Balb-c *Pax6*$^{Sey\text{-}Neu/+}$ (Fig. 2.2) (Cole et al., 2022). This was novel, as Hickmott et al. found that background, but not *Pax6* genotype, significantly altered retinal thickness, though it should be noted that in their study, Hickmott et al. only measured relatively normal areas and did not identify and separately quantify hotspots (Hickmott et al., 2018). Our measurements in C57Bl/6 and 129S/Svlmj

Pax6^{Sey} proved more inconsistent, however, as high variations in hotspot regions introduces limited statistical significance when compared to normal retinal regions (Fig 3.3).

Clearly, hotspots show a higher density of cells in layers that are disorganized or altogether absent. It is unclear what cells most contribute to these hotspots, and our quantification of known retinal subtypes in these most affected layers has found no significant increases or decreases in RGCs or amacrine cells (Supp. 3.3). This also matches some of the findings of Hickmott et al., who did not find a significant change in the cell densities of GCL, INL, or ONL components, though once again they did not separately quantify the hotspots regions (Cole et al., 2022; Hickmott et al., 2018). This might suggest another, yet unlabeled population makes up the bulk of these hotspots, possibly undifferentiated RPCs, though further immunohistochemical studies would need to confirm this.

We found some success quantifying the size and number of hotspots in Balb-c *Pax6*$^{Sey\text{-}Neu/+}$ mice (Fig. 2.5) (Cole et al., 2022). This does confirm that Pax6-deficiency correlates with larger, more numerous loci of retinal damage. However, it is unclear whether these hotspots can form or increase in size later in adulthood. It has been established that these morphological disruptions are often present at birth, and the degree to which they worsen in size and number requires confirmation in future studies (Cole et al., 2022; Gregory-Evans et al., 2014; Rabiee et al., 2020; Wang et al., 2017). We have previously cited glaucoma as a possible exacerbating factor, but other anterior defects may likely contribute (Cole et al., 2022; Cole et al., 2021). Microphthalmia, for one, is a major component in these mouse models and it is possible that hypoplasia of the lens may lead to subsequent compaction or detachment of retina from RPE. Similarly, hotspot like accumulations have been describe in other models of retinal degeneration, including retinitis pigmentosa, though these dystrophies appear more dramatic in the OS, rather

than the inner retina (Fernández-Sánchez et al., 2015). Some of these hotspots, especially the "oxbow" types, are likewise reminiscent of macular edemas, a swelling of the retina characterized by a build-up of proteins and fluid in the rear of the retina, often resulting in pockets of detachment (Daruich et al., 2018). This can be caused by disruptions in fluid balance mediated by outer-retinal blood barriers and compounded by disruptions in the retinal layering. This may explain some of the especially distended, curled pockets, as abnormal layering caused by Pax6-deficits, and pan-retinal swelling, might combine with an edema to create the more even, oxbow hotspots seen in some retina, though this requires further study.

Nerve fiber layer thinning is another known component of retinodegenerative diseases like glaucoma, and, when imaged with *in vivo* methods such as OCT, this phenotype can provide one the most clinically reliable methods for monitoring retinal health in human patients (Grannonico et al., 2021; Katagiri et al., 2017; Miller et al., 2020; Yi et al., 2016). The nerve fiber layers of aniridic mice show disruption, possibly from underlying retinal disorganization and hotspots (Cole et al., 2022). This, coupled with the abnormal axon bundle morphology and defasciculation, may further contribute to declines in vision (Cole et al., 2022; Lalitha et al., 2020). In Cole et al., we found that aniridic mice treated with a Pax6-dosage-compensating drug showed improved RGC axon bundling and ONH morphology which correlated with improved visual acuity (Cole et al., 2022). Thus, RGC axon morphology provides yet another viable assessment of aniridic damage in retina, and may provide the basis for future prognostics using *in vivo* imaging methods like Vis-OCT.

Electroretinography is also a standardized approach for assessing visual heath in degenerative retinal diseases and has been used as a metric of functional deficits in aniridia (Tremblay et al., 1998; Wang et al., 2017). Early ERG assessments of aniridia in humans found

that approximately 73% of cases showed irregular a- and b-waveforms, as well as reduced oscillatory potentials, indicating a disruption of rods, cones, bipolar cells, and amacrine cells (Wu et al., 1991). Gregory-Evans et al. found similar ERG deficits in *small-eye* mice, with mean amplitudes of both scotopic and photopic b-wave and a-wave responses at nearly 0 µV as compared to the WT mean b-wave amplitude of about 600 µV and mean a-wave amplitude of about 80 µV (Gregory-Evans et al., 2014). Very similar results were found in their follow-up study (Wang et al., 2017). These functional deficits could arise from many of the aforementioned defects in aniridia. For one, anterior segment occlusion likely prevents light from reaching photoreceptors, thereby reducing visual inputs to the inner retina. Likewise, retinal layer disorganization and possible RPC dysplasia would likely impair normal synaptogenesis in various strata of the retinal layers (Wu, 2010).

Another common method of assessing aniridia's effect on visual behavior is to measure visual acuity via the optomotor or optokinetic response (Abdeljalil et al., 2005; Chang et al., 2014; Cole et al., 2022; Krause et al., 2023). Previously thought to serve as a behavioral correlate for RGC loss, it is now believed that declines in optomotor responses are the result of a combination of retina-impairing factors (Hood, 2019). Variability in phenotypes, especially in eye size and potential anophthalmia can severely limit comparisons and assessments in experimental settings. Likewise, anterior defects can again impair light from reaching photoreceptors, thus reducing visual behavior (Cole et al., 2022; Cole et al., 2021). Recent work has shown that genetic landscape does play a further role in reduced visual acuity of aniridia subjects. Krause et al. found that patients suffering from larger chromosome 11 deletions such as those in WAGR syndrome exhibited lower mean visual acuity than patients suffering from a nonsense-mutation-mediated form of aniridia. This suggests that broader deletions in multiple

genes will compound the visual deficits of patients more so than a classical form of aniridia (Krause et al., 2023).

Our recent discovery of increased glial recruitment and activation in aniridic retina (Fig. 3.5 and 3.6) also presents interesting new insights into the retina-wide effects of the disease. Gliosis is a known indicator of neuroinflammatory responses to various degenerative diseases, including retinitis pigmentosa, diabetic retinopathy, and glaucoma (Fernández-Sánchez et al., 2015; Kinuthia et al., 2020; Kumari et al., 2022). Chief contributors are activated microglia which release cytokines that further degenerates surrounding tissue (Bosco et al., 2011; Dixon et al., 2021; Kumari et al., 2022). While our previous findings relegated retinal damage to discrete loci (hotspots), our discovery of higher densities of activacted microglia in *Pax6*^{Sey} retinas indicates more ubiquitous tissue damage (Fig. 3.5). The density of active microglia in adult (P80) *Pax6*^{Sey} mice was significantly higher than in WT mice and this significance increased from that of P30 *Pax6*^{Sey} vs. WT mice. This suggests an increased cytotoxic environment likely contributing to further retinal attenuation in later adulthood. Neuroinflammation can also trigger reactive gliosis in which astrocytes, which are normally responsible for retina homeostasis, rapidly migrate and become hypertrophic, often recruiting more cytoskeletal components like GFAP (de Hoz et al., 2016). These immunoreactive astrocytes initiate many neuroprotective cascades, including metabolic stimulants and cell stabilizing factors. These astrocytes tend to increase in density the later stages of retinodegenerative conditions such retinitis pigmentosa and glaucoma, an effect we saw in our own comparisons of P30 and P80 *Pax6*^{Sey} retinas (Chapter 3) (de Hoz et al., 2016; Gallego et al., 2012).

4.6 Drug treatment and future approaches to aniridia intervention

There are no medical interventions that can completely treat aniridia, though ongoing work has found several candidate therapies that might stem the disease's progression and improve overall quality of life for patients (2019-2022; Cole et al., 2022; Daruich et al., 2022; Gregory-Evans et al., 2014; Rabiee et al., 2020; Wang et al., 2017). Current methods aim to reduce the severity of individual symptoms, including cataracts, keratopathy, iris hypoplasia, and glaucoma (Daruich et al., 2022).

For subjects with aniridia, underdeveloped or missing irises prevent normal regulation of light inputs into the eye. Most of these patients mitigate photophobic effects through specialized sunglasses, but more robust methods such as iris prosthetics provide long-term solutions to this issue (Daruich et al., 2022; Samant et al., 2016). The implanting of these devices is risky, though, and may hinder vision with post-operative complications. Lens-fixed diaphragms, for example, are large, rigid, and brittle, with upwards of 30% patients having reported secondary glaucoma following intraocular implantation (Daruich et al., 2022; Reinhard et al., 2000). Artificial irises cause fewer post-operative problems and have become a popular alternative, though other congenital aniridia defects, such as lens and ciliary deformation, are known to interfere with their implementation (Mayer et al., 2020).

Cataract surgery is another common intervention. Cataracts tend to form even in young patients and thus present one of the earliest visual occlusions in aniridia (Chang et al., 2002; Glaser et al., 1994; Prosser and van Heyningen, 1998). Such surgeries are rarely permanent solutions, as lens defects tend to give rise to new cataracts, especially later in life. This can be counteracted with lens implantation, though, like iris surgeries, post-operative complications can result in other unwanted effects (Daruich et al., 2022; Mayer et al., 2020).

While these treatments may account for anterior segment defects, clinicians face more challenges in reducing retinal damage, particularly those arising from glaucoma (Cole et al., 2021; Lee et al., 2008; Nelson et al., 1984; Netland, 2015). Topical glaucoma treatments meant to control IOP such as prostaglandin analogs and beta-blockers are most common (Daruich et al., 2022). These provide some relief but are less effective than surgical interventions such as trabeculotomies and goniotomies (Cole et al., 2021; Lee et al., 2008; Netland, 2015; Walton, 1986). Still, if surgical or topical treatments fail to regulate IOP, angle drainage devices may become necessary to moderate late-stage glaucomatous damage (Landsend et al., 2021). In particular, the Ahmed drainage implant is reported to have the highest rate of success, with a 100% reported efficacy six months after insertion, and 88% after a year (Almousa and Lake, 2014).

Even with these approaches, it is now known that retinal damage exists prior to glaucoma development (Cole et al., 2022; Daruich et al., 2022; Hickmott et al., 2018; Rabiee et al., 2020; Wang et al., 2017). As neuronal damage is irreversible, earlier, perhaps pre-natal interventions are needed to prevent hotspots, RNFL disruptions, and foveal hypoplasia. This has led many researchers to focus their efforts on novel gene therapies and drug applications that will target maturing eye tissues that require peri-natal dosages of Pax6 (Cole et al., 2022; Cole et al., 2021; Daruich et al., 2022; Mohanna et al., 2020; Rabiee et al., 2020).

Gene therapy could provide the most well-rounded treatment, especially if said therapies can rescue normal *PAX6* expression levels. Reaching this precise expression level is critical however, as overcompensation of Pax6 dosage has also been linked to irregularities in tissue formation, and even some hyperplasias (Li and Lu, 2005; Manuel et al., 2008; Remez et al., 2017; Wang et al., 2017). Novel gene-editing via CRISPR/Cas9 systems have shown partial

success in ameliorating *Pax6*^{Sey} mice through germline correction, though this therapy still requires much optimization (Mohanna et al., 2020). Antisense oligonucleotide (ASO) treatments have also been proposed, but current theories propose aniridia's haploinsufficiency results from degradation of mRNA, which would render ASO ineffective (Daruich et al., 2022). Meanwhile, recent work by Latta et al. found that miRNAs and mRNAs are dysregulated in the conjunctiva of aniridic subjects, with many cells in these regions persisting in a proliferative state. This could provide a practical avenue of intervention across mutant subjects, as this effect appears to manifest in a mutation-independent manner (Latta et al., 2021). In general, genetic approaches are relatively new in aniridia treatment but have the potential to generate the most permanent therapeutic results.

Drug interventions have been focus of study over the last decade, as they have demonstrated the most immediate, cost-effective, and least invasive methods in aniridia mitigation (Cole et al., 2022; Gregory-Evans et al., 2014; Rabiee et al., 2020; Wang et al., 2017). The most promising pharmacological approaches come in the form of mutation suppressants, particularly TRIDs (Campofelice et al., 2019; Gregory-Evans et al., 2014; Haas et al., 2015; Wang et al., 2017). Among these drugs, aminoglycosides and oxadiozoles show the most promising early results. Initially, the aminoglycoside gentamicin, traditionally used to counteract gram-negative bacteria, was purported to be the most effective drug candidate (Campofelice et al., 2019; Daruich et al., 2022). Despite early success, its cytotoxic effects and tendency to induce read-through of normal STOP codons has led researchers to reconsider its feasibility (Leubitz et al., 2019). More recent investigations have favored the mutation suppressant ataluren, which is currently used to treat Duchenne Muscular Dystrophy. Ataluren is theorized to function via a mechanism of near-aminoacyl insertion at the site of PTCs, particularly UGA (Fig 1.1).

This function derives from a heightened PTC affinity managed by a five-member, oxygen-nitrogen-nitrogen aromatic ring (Campofelice et al., 2019). Interestingly, this proposed mechanism does bring the nonsense-mediated decay theory of aniridia's haploinsufficiency into question. If ataluren functions at a translational level, then a significant number of mutant gene transcripts must be reaching ribosomes. Either way, the exact mechanism of ataluren's function is not well understood and requires further study (Cole et al., 2021; Gregory-Evans et al., 2014; Wang et al., 2017).

Despite this uncertain mechanism, experimenters used it to successfully reduce aniridic phenotypes, including those in the retina (Gregory-Evans et al., 2014; Wang et al., 2017). These results were promising enough for early approval by the FDA, though a recent clinical trial of an orally-delivered form of ataluren (trademarked as Translarna™) was not successful (2019-2022). This is likely the result of sample patients who were solely of an advanced age, and therefore presented late-stage phenotypes that were more resistant to treatment. Similarly, oral administration of ataluren has shown limited localization to the posterior portions of the eye, hampering its potential effects in the retina (Gregory-Evans et al., 2014; Wang et al., 2017). Ideally, a novel method of drug delivery would maximize ataluren's effectiveness, possibly protecting against many advanced aniridic phenotypes. Even administration to pregnant subjects may help to reduce the pre-natal defects, though the potential for other gestational disruptions is high (Rabiee et al., 2020). One possible drug delivery method is the novel dendrimer microgel developed by Dr. Yang Hu (Wang et al., 2021). This method would suspend the drug in gel particles which would increase bioavailability following topical application. Coupled with a dendrimer-mediated localization to target tissues, this innovation would maximize ataluren concentration to both anterior and posterior eye regions. This formulation has already shown

great success in delivering anti-glaucoma drugs such as brimonidine tartrate and timolol maleate (Wang et al., 2021). Our collaboration with Dr. Yang Hu's lab is ongoing and aims to produce an ataluren microgel preparation more efficacious that previous topical formulations.

Other pharmacological methods aimed at Pax6 dosage compensation have also shown moderate success at reducing aniridia phenotypes (Li and Lu, 2005; Meng et al., 2014; Ouyang et al., 2006; Simpson and Price, 2002; Warren et al., 1999). Most promising are drugs involved in the MEK-ERK pathway, which is known to function opposite that of the *PAX6* pathway. This has led some researchers to conclude that suppression of the former will lead to upregulation of *PAX6* (de la Puente et al., 2016). Use of topical MEK-inhibitors such as PD0325901 has been shown to protect against aniridia phenotypes in both the anterior and posterior segments of the eye, an effect that was maintained well into adulthood (Cole et al., 2022; Rabiee et al., 2020). Still, topical application may not have localized PD0325901 fully to the retina, and our initial results indicated only a partial protection of retina (Cole et al., 2022). Since retina cannot self-repair, unlike corneal or lens tissue, PD0325901's partial protection of anterior regions likely helped prevent more extreme aniridia phenotypes from developing in the retina tissue rather than rescuing pre-natal damage. For a more complete rescue, PD0325901 may be needed to initiate Pax6-dosage compensation during pre-natal ocular development, though such treatments may produce other embryonic side-effects (Cole et al., 2022; Rabiee et al., 2020). Our collaborators in Dr. Ali Djalilian's lab continue to study this approach.

Regardless of the method, further investigation is required to better understand the appropriate therapies, timing, and delivery best suited for aniridia. Post-natal methods have shown limited success and short-term-efficacy, especially in the retina, a region where damage prevention/protection is most necessary. Until a reliable genetic, mutation-suppressing, or

dosage-compensating mechanism is discovered, patients are best managed with a combination of symptom-specific treatments (Bobilev et al., 2016; Cole et al., 2021; Netland, 2015; Shiple et al., 2015).

4.7 Conclusion

Despite decades of clinical and experimental aniridia research, many questions yet remain about the origins, development, and mediation of the disease. While most translational studies have focused on its effects in the anterior regions of the eye, many new discoveries on its retinal impact provide novel insights into *PAX6*'s role in developing neural tissues. As the *PAX6* pathway is so diverse, with many targets, functions, and age-dependent expression levels, it can be difficult to isolate any one route by which retina is malformed. Likewise, the levels and severity of this dosage-dependence leads to such high phenotypic variance that a singular method for diagnosis and treatment is difficult. Rather, more nuanced, case-dependent approaches must be employed to better counteract the disease. Current methods are limited in efficacy but show much promise for future clinical applications. Our own discoveries in the retina provide new insights into the retina-wide recruitment of reactive glia, suggesting a neuroimmune response which likely contributes to late-stage visual decline. Altogether, retinal deficits in aniridia represent a complex array of developmental pathways and cellular interactions which require further study.

References

2019-2022. Study of Ataluren in Participants with Nonsense Mutation Aniridia (STAR). US National Library of Medicine NIHMSID: NCT02647359.

Abdeljalil, J., Hamid, M., Abdel-Mouttalib, O., Stéphane, R., Raymond, R., Johan, A., José, S., Pierre, C., Serge, P., 2005. The optomotor response: a robust first-line visual screening method for mice. Vision Res 45, 1439-1446.

Agathocleous, M., Harris, W.A., 2009. From Progenitors to Differentiated Cells in the Vertebrate Retina. Annual Review of Cell and Developmental Biology 25, 45-69.

Ahmed N R M, T.R., Vanathi M, 2014. Diagnosis and Management of Aniridia. American Academy of Opthalmology, Eye Net Magazine.

Almousa, R., Lake, D.B., 2014. Intraocular pressure control with Ahmed glaucoma drainage device in patients with cicatricial ocular surface disease-associated or aniridia-related glaucoma. Int Ophthalmol 34, 753-760.

Ashery-Padan, R., Marquardt, T., Zhou, X., Gruss, P., 2000. Pax6 activity in the lens primordium is required for lens formation and for correct placement of a single retina in the eye. Genes Dev 14, 2701-2711.

Axton, R., Hanson, I., Danes, S., Sellar, G., van Heyningen, V., Prosser, J., 1997. The incidence of PAX6 mutation in patients with simple aniridia: an evaluation of mutation detection in 12 cases. J Med Genet 34, 279-286.

Azuma, N., Yamaguchi, Y., Handa, H., Tadokoro, K., Asaka, A., Kawase, E., Yamada, M., 2003. Mutations of the PAX6 gene detected in patients with a variety of optic-nerve malformations. Am J Hum Genet 72, 1565-1570.

Beauchamp, G.R., Meisler, D.M., 1986. An alternative hypothesis for iris maldevelopment (aniridia). J Pediatr Ophthalmol Strabismus 23, 281-283.

Beckmann, L., Cai, Z., Cole, J., Miller, D.A., Liu, M., Grannonico, M., Zhang, X., Ryu, H.J., Netland, P.A., Liu, X., Zhang, H.F., 2021. In vivo imaging of the inner retinal layer structure in mice after eye-opening using visible-light optical coherence tomography. Exp Eye Res 211, 108756.

Bidou, L., Bugaud, O., Belakhov, V., Baasov, T., Namy, O., 2017. Characterization of new-generation aminoglycoside promoting premature termination codon readthrough in cancer cells. RNA Biol 14, 378-388.

Bobilev, A.M., McDougal, M.E., Taylor, W.L., Geisert, E.E., Netland, P.A., Lauderdale, J.D., 2016. Assessment of PAX6 alleles in 66 families with aniridia. Clin Genet 89, 669-677.

Bosco, A., Steele, M.R., Vetter, M.L., 2011. Early microglia activation in a mouse model of chronic glaucoma. J Comp Neurol 519, 599-620.

Campofelice, A., Lentini, L., Di Leonardo, A., Melfi, R., Tutone, M., Pace, A., Pibiri, I., 2019. Strategies against Nonsense: Oxadiazoles as Translational Readthrough-Inducing Drugs (TRIDs). Int J Mol Sci 20.

Castillo-Quan, J.I., Tain, L.S., Kinghorn, K.J., Li, L., Grönke, S., Hinze, Y., Blackwell, T.K., Bjedov, I., Partridge, L., 2019. A triple drug combination targeting components of the nutrient-sensing network maximizes longevity. Proc Natl Acad Sci U S A 116, 20817-20819.

Chang, B., Hawes, N.L., Hurd, R.E., Davisson, M.T., Nusinowitz, S., Heckenlively, J.R., 2002. Retinal degeneration mutants in the mouse. Vision Research 42, 517-525.

Chang, J.W., Kim, J.H., Kim, S.J., Yu, Y.S., 2014. Congenital aniridia: long-term clinical course, visual outcome, and prognostic factors. Korean J Ophthalmol 28, 479-485.

Chen, H., Wei, X., Cho, K.-S., Chen, G., Sappington, R., Calkins, D.J., Chen, D.F., 2011. Optic Neuropathy Due to Microbead-Induced Elevated Intraocular Pressure in the Mouse. Investigative Ophthalmology & Visual Science 52, 36-44.

Chen, H., Zhao, Y., Liu, M., Feng, L., Puyang, Z., Yi, J., Liang, P., Zhang, H.F., Cang, J., Troy, J.B., Liu, X., 2015. Progressive degeneration of retinal and superior collicular functions in mice with sustained ocular hypertension. Invest Ophthalmol Vis Sci 56, 1971-1984.

Chen, M., Zhang, L., Xu, J., Chen, X., Gu, Y., Ren, Y., Wang, K., 2019. Comparability of three intraocular pressure measurement: iCare pro rebound, non-contact and Goldmann applanation tonometry in different IOP group. BMC Ophthalmology 19, 225.

Chhabra, N.F., Amarie, O.V., Wu, M., Amend, A.L., Rubey, M., Gradinger, D., Irmler, M., Beckers, J., Rathkolb, B., Wolf, E., Feuchtinger, A., Huypens, P., Teperino, R., Rozman, J., Przemeck, G.K.H., Hrabě de Angelis, M., 2020. PAX6 mutation alters circadian rhythm and β cell function in mice without affecting glucose tolerance. Commun Biol 3, 628.

Churchill, A., Booth, A., 1996. Genetics of aniridia and anterior segment dysgenesis. Br J Ophthalmol 80, 669-673.

Cole, J.D., McHaney, K.M., Rabiee, B., Gao, J., Rodriguez, C., Miller, D.A., Liu, M., Grannonico, M., Norat, P., Zhang, H.F., Djalilian, A.R., Liu, X., 2022. Long-term retinal protection by MEK inhibition in Pax6 haploinsufficiency mice. Exp Eye Res 218, 109012.

Cole, J.D., Rodriguez, C., Norat, P., Gao, J., I., P., Netland, P.A., Liu, X., 2021. Neural damage and neuroprotection with glaucoma

development in aniridia. Current Neurobiology 12(1), 14-19.

Cvekl, A., Yang, Y., Chauhan, B.K., Cveklova, K., 2004. Regulation of gene expression by Pax6 in ocular cells: a case of tissue-preferred expression of crystallins in lens. Int J Dev Biol 48, 829-844.

Dabrowski, M., Bukowy-Bieryllo, Z., Zietkiewicz, E., 2018. Advances in therapeutic use of a drug-stimulated translational readthrough of premature termination codons. Molecular Medicine 24, 25.

Daruich, A., Duncan, M., Robert, M.P., Lagali, N., Semina, E.V., Aberdam, D., Ferrari, S., Romano, V., des Roziers, C.B., Benkortebi, R., De Vergnes, N., Polak, M., Chiambaretta, F., Nischal, K.K., Behar-Cohen, F., Valleix, S., Bremond-Gignac, D., 2022. Congenital aniridia beyond black eyes: From phenotype and novel genetic mechanisms to innovative therapeutic approaches. Progress in Retinal and Eye Research, 101133.

Alejandra Daruich, Alexandre Matet, Alexandre Moulin, Laura Kowalczuk, Michaël Nicolas, Alexandre Sellam, Pierre-Raphaël Rothschild, Samy Omri, Emmanuelle Gélizé, Laurent Jonet, Kimberley Delaunay, Yvonne De Kozak, Marianne Berdugo, Min Zhao, Patricia Crisanti, Francine Behar-Cohen, Mechanisms of macular edema: Beyond the surface, Progress in Retinal and Eye Research, Volume 63, 2018, Pages 20-68, ISSN 1350-9462,

de Hoz, R., Rojas, B., Ramírez, A.I., Salazar, J.J., Gallego, B.I., Triviño, A., Ramírez, J.M., 2016. Retinal Macroglial Responses in Health and Disease. Biomed Res Int 2016, 2954721.

de la Puente, P., Muz, B., Jin, A., Azab, F., Luderer, M., Salama, N.N., Azab, A.K., 2016. MEK inhibitor, TAK-733 reduces proliferation, affects cell cycle and apoptosis, and synergizes with other targeted therapies in multiple myeloma. Blood Cancer J 6, e399.

Dixon, M.A., Greferath, U., Fletcher, E.L., Jobling, A.I., 2021. The Contribution of Microglia to the Development and Maturation of the Visual System. Front Cell Neurosci 15, 659843.

Ellison-Wright, Z., Heyman, I., Frampton, I., Rubia, K., Chitnis, X., Ellison-Wright, I., Williams, S.C., Suckling, J., Simmons, A., Bullmore, E., 2004. Heterozygous PAX6 mutation, adult brain structure and fronto-striato-thalamic function in a human family. Eur J Neurosci 19, 1505-1512.

Feng, L., Chen, H., Suyeoka, G., Liu, X., 2013a. A laser-induced mouse model of chronic ocular hypertension to characterize visual defects. J Vis Exp.

Feng, L., Chen, H., Yi, J., Troy, J.B., Zhang, H.F., Liu, X., 2016. Long-Term Protection of Retinal Ganglion Cells and Visual Function by Brain-Derived Neurotrophic Factor in Mice With Ocular Hypertension. Investigative Ophthalmology & Visual Science 57, 3793-3802.

Feng, L., Puyang, Z., Chen, H., Liang, P., Troy, J.B., Liu, X., 2017. Overexpression of Brain-Derived Neurotrophic Factor Protects Large Retinal Ganglion Cells After Optic Nerve Crush in Mice. eNeuro 4.

Feng, L., Zhao, Y., Yoshida, M., Chen, H., Yang, J.F., Kim, T.S., Cang, J., Troy, J.B., Liu, X., 2013b. Sustained ocular hypertension induces dendritic degeneration of mouse retinal ganglion cells that depends on cell type and location. Invest Ophthalmol Vis Sci 54, 1106-1117.

Fernández-Sánchez, L., Lax, P., Campello, L., Pinilla, I., Cuenca, N., 2015. Astrocytes and Müller Cell Alterations During Retinal Degeneration in a Transgenic Rat Model of Retinitis Pigmentosa. Frontiers in Cellular Neuroscience 9.

Fischbach, B.V., Trout, K.L., Lewis, J., Luis, C.A., Sika, M., 2005. WAGR Syndrome: A Clinical Review of 54 Cases. Pediatrics 116, 984-988.

Free, S.L., Mitchell, T.N., Williamson, K.A., Churchill, A.J., Shorvon, S.D., Moore, A.T., van Heyningen, V., Sisodiya, S.M., 2003. Quantitative MR image analysis in subjects with defects in the PAX6 gene. Neuroimage 20, 2281-2290.

Gallego, B.I., Salazar, J.J., de Hoz, R., Rojas, B., Ramírez, A.I., Salinas-Navarro, M., Ortín-Martínez, A., Valiente-Soriano, F.J., Avilés-Trigueros, M., Villegas-Perez, M.P., Vidal-Sanz, M., Triviño, A., Ramírez, J.M., 2012. IOP induces upregulation of GFAP and MHC-II and microglia reactivity in mice retina contralateral to experimental glaucoma. J Neuroinflammation 9, 92.

Gao, J., Griner, E.M., Liu, M., Moy, J., Provencio, I., Liu, X., 2022a. Differential effects of experimental glaucoma on intrinsically photosensitive retinal ganglion cells in mice. J Comp Neurol 530, 1494-1506.

Gao, J., Provencio, I., Liu, X., 2022b. Intrinsically photosensitive retinal ganglion cells in glaucoma. Front Cell Neurosci 16, 992747.

Geng, Y., Schery, L.A., Sharma, R., Dubra, A., Ahmad, K., Libby, R.T., Williams, D.R., 2011. Optical properties of the mouse eye. Biomed Opt Express 2, 717-738.

Glaser, T., Jepeal, L., Edwards, J.G., Young, S.R., Favor, J., Maas, R.L., 1994. PAX6 gene dosage effect in a family with congenital cataracts, aniridia, anophthalmia and central nervous system defects. Nature Genetics 7, 463-471.

Goel, M., Picciani, R.G., Lee, R.K., Bhattacharya, S.K., 2010. Aqueous humor dynamics: a review. Open Ophthalmol J 4, 52-59.

Grannonico, M., Miller, D.A., Liu, M., Norat, P., Deppmann, C.D., Netland, P.A., Zhang, H.F., Liu, X., 2021. Global and Regional Damages in Retinal Ganglion Cell Axon Bundles Monitored Non-Invasively by Visible-Light Optical Coherence Tomography Fibergraphy. The Journal of Neuroscience 41, 10179-10193.

Graw, J., Löster, J., Puk, O., Münster, D., Haubst, N., Soewarto, D., Fuchs, H., Meyer, B., Nürnberg, P., Pretsch, W., Selby, P., Favor, J., Wolf, E., de Angelis, M.H., 2005. Three Novel

Pax6 Alleles in the Mouse Leading to the Same Small-Eye Phenotype Caused by Different Consequences at Target Promoters. Investigative Ophthalmology & Visual Science 46, 4671-4683.

Gregory-Evans, C.Y., Wang, X., Wasan, K.M., Zhao, J., Metcalfe, A.L., Gregory-Evans, K., 2014. Post-natal manipulation of Pax6 dosage reverses congenital tissue malformation defects. The Journal of Clinical Investigation 124, 111-116.

Gregory-Evans, K., Po, K., Chang, F., Gregory-Evans, C.Y., 2012. Pharmacological enhancement of ex vivo gene therapy neuroprotection in a rodent model of retinal degeneration. Ophthalmic Res 47, 32-38.

Haas, M., Vlcek, V., Balabanov, P., Salmonson, T., Bakchine, S., Markey, G., Weise, M., Schlosser-Weber, G., Brohmann, H., Yerro, C.P., Mendizabal, M.R., Stoyanova-Beninska, V., Hillege, H.L., 2015. European Medicines Agency review of ataluren for the treatment of ambulant patients aged 5 years and older with Duchenne muscular dystrophy resulting from a nonsense mutation in the dystrophin gene. Neuromuscul Disord 25, 5-13.

Hall, H.N., Williamson, K.A., FitzPatrick, D.R., 2019. The genetic architecture of aniridia and Gillespie syndrome. Hum Genet 138, 881-898.

Hanson, I.M., 2003. PAX6 and Congenital Eye Malformations. Pediatric Research 54, 791-796.

Hanson, I.M., Fletcher, J.M., Jordan, T., Brown, A., Taylor, D., Adams, R.J., Punnett, H.H., van Heyningen, V., 1994. Mutations at the PAX6 locus are found in heterogeneous anterior segment malformations including Peters' anomaly. Nature Genetics 6, 168-173.

Hickmott, J.W., Gunawardane, U., Jensen, K., Korecki, A.J., Simpson, E.M., 2018. Epistasis between Pax6(Sey) and genetic background reinforces the value of defined hybrid mouse models for therapeutic trials. Gene Ther 25, 524-537.

Hill, R.E., Favor, J., Hogan, B.L.M., Ton, C.C.T., Saunders, G.F., Hanson, I.M., Prosser, J., Jordan, T., Hastie, N.D., Heyningen, V.v., 1991. Mouse Small eye results from mutations in a paired-like homeobox-containing gene. Nature 354, 522-525.

Hingorani, M., Hanson, I., van Heyningen, V., 2012. Aniridia. European Journal of Human Genetics 20, 1011-1017.

Holmström, G., Eriksson, U., Hellgren, K., Larsson, E., 2010. Optical coherence tomography is helpful in the diagnosis of foveal hypoplasia. Acta Ophthalmol 88, 439-442.

Holst, B.D., Wang, Y., Jones, F.S., Edelman, G.M., 1997. A binding site for Pax proteins regulates expression of the gene for the neural cell adhesion molecule in the embryonic spinal cord. Proc Natl Acad Sci U S A 94, 1465-1470.

Hood, D.C., 2019. Does Retinal Ganglion Cell Loss Precede Visual Field Loss in Glaucoma? J Glaucoma 28, 945-951.

Jiang, S.M., Zeng, L.P., Zeng, J.H., Tang, L., Chen, X.M., Wei, X., 2015. β-III-Tubulin: a reliable marker for retinal ganglion cell labeling in experimental models of glaucoma. Int J Ophthalmol 8, 643-652.

Katagiri, S., Nishina, S., Yokoi, T., Mikami, M., Nakayama, Y., Tanaka, M., Azuma, N., 2017. Retinal Structure and Function in Eyes with Optic Nerve Hypoplasia. Sci Rep 7, 42480-42480.

Kinuthia, U.M., Wolf, A., Langmann, T., 2020. Microglia and Inflammatory Responses in Diabetic Retinopathy. Frontiers in Immunology 11.

Klimova, L., Kozmik, Z., 2014. Stage-dependent requirement of neuroretinal Pax6 for lens and retina development. Development 141, 1292-1302.

Krause, M.A., Trout, K.L., Lauderdale, J.D., Netland, P.A., 2023. Visual Acuity in Aniridia and WAGR Syndrome. Clin Ophthalmol 17, 1255-1261.

Kumari, A., Ayala-Ramirez, R., Zenteno, J.C., Huffman, K., Sasik, R., Ayyagari, R., Borooah, S., 2022. Single cell RNA sequencing confirms retinal microglia activation associated with early onset retinal degeneration. Sci Rep 12, 15273.

Lalitha, S., Basu, B., Surya, S., Meera, V., Riya, P.A., Parvathy, S., Das, A.V., Sivakumar, K.C., Nelson-Sathi, S., James, J., 2020. Pax6 modulates intra-retinal axon guidance and fasciculation of retinal ganglion cells during retinogenesis. Sci Rep 10, 16075.

Landsend, E.C., Lagali, N., Utheim, T.P., 2021. Congenital aniridia–A comprehensive review of clinical features and therapeutic approaches. Survey of ophthalmology 66, 1031-1050.

Latta, L., Ludwig, N., Krammes, L., Stachon, T., Fries, F., Mukwaya, A., Szentmáry, N., Seitz, B., Wowra, B., Kahraman, M., 2021. Abnormal neovascular and proliferative conjunctival phenotype in limbal stem cell deficiency is associated with altered microRNA and gene expression modulated by PAX6 mutational status in congenital aniridia. The Ocular Surface 19, 115-127.

Lee, H., Khan, R., O'Keefe, M., 2008. Aniridia: current pathology and management. Acta Ophthalmol 86, 708-715.

Leubitz, A., Frydman-Marom, A., Sharpe, N., van Duzer, J., Campbell, K.C.M., Vanhoutte, F., 2019. Safety, Tolerability, and Pharmacokinetics of Single Ascending Doses of ELX-02, a Potential Treatment for Genetic Disorders Caused by Nonsense Mutations, in Healthy Volunteers. Clin Pharmacol Drug Dev 8, 984-994.

Li, T., Lu, L., 2005. Epidermal growth factor-induced proliferation requires down-regulation of Pax6 in corneal epithelial cells. J Biol Chem 280, 12988-12995.

Lima Cunha, D., Arno, G., Corton, M., Moosajee, M., 2019. The Spectrum of PAX6 Mutations and Genotype-Phenotype Correlations in the Eye. Genes (Basel) 10.

LoRusso, P.M., Krishnamurthi, S.S., Rinehart, J.J., Nabell, L.M., Malburg, L., Chapman, P.B., DePrimo, S.E., Bentivegna, S., Wilner, K.D., Tan, W., Ricart, A.D., 2010. Phase I pharmacokinetic and pharmacodynamic study of the oral MAPK/ERK kinase inhibitor PD-0325901 in patients with advanced cancers. Clin Cancer Res 16, 1924-1937.

Luna, G., Lewis, G.P., Banna, C.D., Skalli, O., Fisher, S.K., 2010. Expression profiles of nestin and synemin in reactive astrocytes and Müller cells following retinal injury: a comparison with glial fibrillar acidic protein and vimentin. Mol Vis 16, 2511-2523.

Manuel, M., Pratt, T., Liu, M., Jeffery, G., Price, D.J., 2008. Overexpression of Pax6 results in microphthalmia, retinal dysplasia and defective retinal ganglion cell axon guidance. BMC Developmental Biology 8, 59.

Maulbecker, C.C., Gruss, P., 1993. The oncogenic potential of Pax genes. Embo j 12, 2361-2367.

Mayer, C.S., Hoffmann, A.M., Prahs, P., Reznicek, L., Khoramnia, R., 2020. Functional outcomes after combined iris and intraocular lens implantation in various iris and lens defects. BMC ophthalmology 20, 1-7.

McCulley, T.J., Mayer, K., Dahr, S.S., Simpson, J., Holland, E.J., 2005. Aniridia and optic nerve hypoplasia. Eye 19, 762-764.

Medeiros, F.A., Lisboa, R., Weinreb, R.N., Liebmann, J.M., Girkin, C., Zangwill, L.M., 2013. Retinal ganglion cell count estimates associated with early development of visual field defects in glaucoma. Ophthalmology 120, 736-744.

Meng, B., Wang, Y., Li, B., 2014. Suppression of PAX6 promotes cell proliferation and inhibits apoptosis in human retinoblastoma cells. Int J Mol Med 34, 399-408.

Mi, D., Huang, Y.-T., Kleinjan, D.A., Mason, J.O., Price, D.J., 2013. Identification of genomic regions regulating Pax6 expression in embryonic forebrain using YAC reporter transgenic mouse lines. PLoS One 8, e80208-e80208.

Miller, D.A., Grannonico, M., Liu, M., Kuranov, R.V., Netland, P.A., Liu, X., Zhang, H., 2020. Visible-light optical coherence tomography fibergram for monitoring retinal ganglion cell axon bundles in vivo. Investigative Ophthalmology & Visual Science 61, 2529-2529.

Mohanna, S.Z.M., Hickmott, J.W., Lam, S.L., Chiu, N.Y., Lengyell, T.C., Tam, B.M., Moritz, O.L., Simpson, E.M., 2020. Germline CRISPR/Cas9-mediated gene editing prevents vision loss in a novel mouse model of aniridia. Molecular Therapy-Methods & Clinical Development 17, 478-490.

Moosajee M, H., M., Moore, A, 2018. PAX6-Related Aniridia. GeneReviews.

Nelson, L.B., Spaeth, G.L., Nowinski, T.S., Margo, C.E., Jackson, L., 1984. Aniridia. A review. Surv Ophthalmol 28, 621-642.

Netland, P.A., 2015. Management of Glaucoma in Congenital Aniridia, in: Parekh, M., Poli, B., Ferrari, S., Teofili, C., Ponzin, D. (Eds.), Aniridia: Recent Developments in Scientific and Clinical Research. Springer International Publishing, Cham, pp. 27-37.

Netland, P.A., Scott, M.L., Boyle, J.W., Lauderdale, J.D., 2011. Ocular and systemic findings in a survey of aniridia subjects. Journal of American Association for Pediatric Ophthalmology and Strabismus 15, 562-566.

Ng, M.Y., Zhang, H., Weil, A., Singh, V., Jamiolkowski, R., Baradaran-Heravi, A., Roberge, M., Jacobson, A., Friesen, W., Welch, E., Goldman, Y.E., Cooperman, B.S., 2018. New in Vitro Assay Measuring Direct Interaction of Nonsense Suppressors with the Eukaryotic Protein Synthesis Machinery. ACS Medicinal Chemistry Letters 9, 1285-1291.

Nishina, S., Kohsaka, S., Yamaguchi, Y., Handa, H., Kawakami, A., Fujisawa, H., Azuma, N., 1999. PAX6 expression in the developing human eye. Br J Ophthalmol 83, 723-727.

Okamoto, F., Nakano, S., Okamoto, C., Hommura, S., Oshika, T., 2004. Ultrasound biomicroscopic findings in aniridia. Am J Ophthalmol 137, 858-862.

Ouyang, J., Shen, Y.-C., Yeh, L.-K., Li, W., Coyle, B.M., Liu, C.-Y., Fini, M.E., 2006. Pax6 overexpression suppresses cell proliferation and retards the cell cycle in corneal epithelial cells. Investigative ophthalmology & visual science 47, 2397-2407.

Pedersen, H.R., Baraas, R.C., Landsend, E.C.S., Utheim Ø, A., Utheim, T.P., Gilson, S.J., Neitz, M., 2020. PAX6 Genotypic and Retinal Phenotypic Characterization in Congenital Aniridia. Invest Ophthalmol Vis Sci 61, 14.

Pierce, J.E., Krafft, C.E., Rodrigue, A.L., Bobilev, A.M., Lauderdale, J.D., McDowell, J.E., 2014. Increased functional connectivity in intrinsic neural networks in individuals with aniridia. Front Hum Neurosci 8, 1013.

Prosser, J., van Heyningen, V., 1998. PAX6 mutations reviewed. Human Mutation 11, 93-108.

Puyang, Z., Feng, L., Chen, H., Liang, P., Troy, J.B., Liu, X., 2016. Retinal Ganglion Cell Loss is Delayed Following Optic Nerve Crush in NLRP3 Knockout Mice. Sci Rep 6, 20998.

Quigley, H.A., 1999. Neuronal death in glaucoma. Progress in Retinal and Eye Research 18, 39-57.

Quigley, H.A., 2005. New paradigms in the mechanisms and management of glaucoma. Eye (Lond) 19, 1241-1248.

Rabiee, B., Anwar, K.N., Shen, X., Putra, I., Liu, M., Jung, R., Afsharkhamseh, N., Rosenblatt, M.I., Fishman, G.A., Liu, X., Ghassemi, M., Djalilian, A.R., 2020. Gene dosage manipulation alleviates manifestations of hereditary PAX6 haploinsufficiency in mice. Sci Transl Med 12.

Rangarajan, K.V., Lawhn-Heath, C., Feng, L., Kim, T.S., Cang, J., Liu, X., 2011. Detection of Visual Deficits in Aging DBA/2J Mice by Two Behavioral Assays. Current Eye Research 36, 481-491.

Rashid, K., Akhtar-Schaefer, I., Langmann, T., 2019. Microglia in Retinal Degeneration. Front Immunol 10, 1975.

Raviv, S., Bharti, K., Rencus-Lazar, S., Cohen-Tayar, Y., Schyr, R., Evantal, N., Meshorer, E., Zilberberg, A., Idelson, M., Reubinoff, B., Grebe, R., Rosin-Arbesfeld, R., Lauderdale, J., Lutty, G., Arnheiter, H., Ashery-Padan, R., 2014. PAX6 Regulates Melanogenesis in the Retinal Pigmented Epithelium through Feed-Forward Regulatory Interactions with MITF. PLOS Genetics 10, e1004360.

Reinhard, T., Engelhardt, S., Sundmacher, R., 2000. Black diaphragm aniridia intraocular lens for congenital aniridia: long-term follow-up. Journal of Cataract & Refractive Surgery 26, 375-381.

Remez, L.A., Onishi, A., Menuchin-Lasowski, Y., Biran, A., Blackshaw, S., Wahlin, K.J., Zack, D.J., Ashery-Padan, R., 2017. Pax6 is essential for the generation of late-born retinal neurons and for inhibition of photoreceptor-fate during late stages of retinogenesis. Dev Biol 432, 140-150.

Rodriguez, A.R., de Sevilla Müller, L.P., Brecha, N.C., 2014. The RNA binding protein RBPMS is a selective marker of ganglion cells in the mammalian retina. J Comp Neurol 522, 1411-1443.

Saenz-Frances, F., Jañez, L., Borrego-Sanz, L., Berrozpe-Villabona, C., Martinez-de-la-Casa, J.M., Morales-Fernandez, L., Garcia-Sanchez, J., Santos-Bueso, E., Garcia-Feijoo, J., 2015. Correlations between corneal and optic nerve head variables in healthy subjects and patients with primary open angle glaucoma. Int J Ophthalmol 8, 1156-1161.

Samant, M., Chauhan, B.K., Lathrop, K.L., Nischal, K.K., 2016. Congenital aniridia: etiology, manifestations and management. Expert Rev Ophthalmol 11, 135-144.

Sanes, J.R., Masland, R.H., 2015. The types of retinal ganglion cells: current status and implications for neuronal classification. Annu Rev Neurosci 38, 221-246.

Sannan, N.S., Gregory-Evans, C.Y., Lyons, C.J., Lehman, A.M., Langlois, S., Warner, S.J., Zakrzewski, H., Gregory-Evans, K., 2017. Correlation of novel PAX6 gene abnormalities in aniridia and clinical presentation. Can J Ophthalmol 52, 570-577.

Savinova, O.V., Sugiyama, F., Martin, J.E., Tomarev, S.I., Paigen, B.J., Smith, R.S., John, S.W., 2001. Intraocular pressure in genetically distinct mice: an update and strain survey. BMC Genet 2, 12-12.

Shaham, O., Menuchin, Y., Farhy, C., Ashery-Padan, R., 2012. Pax6: a multi-level regulator of ocular development. Prog Retin Eye Res 31, 351-376.

Sheng, G., Thouvenot, E., Schmucker, D., Wilson, D.S., Desplan, C., 1997. Direct regulation of rhodopsin 1 by Pax-6/eyeless in Drosophila: evidence for a conserved function in photoreceptors. Genes Dev 11, 1122-1131.

Shiple, D., Finklea, B., Lauderdale, J.D., Netland, P.A., 2015. Keratopathy, cataract, and dry eye in a survey of aniridia subjects. Clin Ophthalmol 9, 291-295.

Shu, X., Beckmann, L., Zhang, H., 2017. Visible-light optical coherence tomography: a review. J Biomed Opt 22, 1-14.

Simpson, T.I., Price, D.J., 2002. Pax6; a pleiotropic player in development. Bioessays 24, 1041-1051.

Sisodiya, S.M., Free, S.L., Williamson, K.A., Mitchell, T.N., Willis, C., Stevens, J.M., Kendall, B.E., Shorvon, S.D., Hanson, I.M., Moore, A.T., van Heyningen, V., 2001. PAX6

haploinsufficiency causes cerebral malformation and olfactory dysfunction in humans. Nat Genet 28, 214-216.

Solberg, N.T., Melheim, M., Strand, M.F., Olsen, P.A., Krauss, S., 2019. MEK Inhibition Induces Canonical WNT Signaling through YAP in KRAS Mutated HCT-15 Cells, and a Cancer Preventive FOXO3/FOXM1 Ratio in Combination with TNKS Inhibition. Cancers (Basel) 11.

Stoykova, A., Götz, M., Gruss, P., Price, J., 1997. Pax6-dependent regulation of adhesive patterning, R-cadherin expression and boundary formation in developing forebrain. Development 124, 3765-3777.

Summers, M.A., Vasiljevski, E.R., Mikulec, K., Peacock, L., Little, D.G., Schindeler, A., 2018. Developmental dosing with a MEK inhibitor (PD0325901) rescues myopathic features of the muscle-specific but not limb-specific Nf1 knockout mouse. Mol Genet Metab 123, 518-525.

Tao, Y., Cao, J., Li, M., Hoffmann, B., Xu, K., Chen, J., Lu, X., Guo, F., Li, X., Phillips, M.J., Gamm, D.M., Chen, H., Zhang, S.C., 2020. PAX6D instructs neural retinal specification from human embryonic stem cell-derived neuroectoderm. EMBO Rep 21, e50000.

Tao, Y., Murakami, Y., Vavvas, D.G., Sonoda, K.H., 2022. Necroptosis and Neuroinflammation in Retinal Degeneration. Front Neurosci 16, 911430.

Tremblay, F., Gupta, S.K., De Becker, I., Guernsey, D.L., Neumann, P.E., 1998. Effects of PAX6 mutations on retinal function: an electroretinographic study. American Journal of Ophthalmology 126, 211-218.

Tyas, D.A., Pearson, H., Rashbass, P., Price, D.J., 2003. Pax6 Regulates Cell Adhesion during Cortical Development. Cerebral Cortex 13, 612-619.

Tzoulaki, I., White, I.M.S., Hanson, I.M., 2005. PAX6 mutations: genotype-phenotype correlations. BMC Genet 6, 27-27.

VanDevanter, D.R., Hamblett, N.M., Simon, N., McIntosh, J., Konstan, M.W., 2021. Evaluating assumptions of definition-based pulmonary exacerbation endpoints in cystic fibrosis clinical trials. J Cyst Fibros 20, 39-45.

Walther, C., Gruss, P., 1991. Pax-6, a murine paired box gene, is expressed in the developing CNS. Development 113, 1435-1449.

Walton, D.S., 1986. Aniridic glaucoma: the results of gonio-surgery to prevent and treat this problem. Trans Am Ophthalmol Soc 84, 59-70.

Wang, J., Li, B., Huang, D., Norat, P., Grannonico, M., Cooper, R.C., Gui, Q., Chow, W.N., Liu, X., Yang, H., 2021. Nano-in-Nano Dendrimer Gel Particles for Efficient Topical Delivery of Antiglaucoma Drugs into the Eye. Chem Eng J 425.

Wang, L., Liu, W., Huang, X., 2018. An approach to revolutionize cataract treatment by enhancing drug probing through intraocular cell line. Libyan J Med 13, 1500347-1500347.

Wang, W.-H., Millar, J.C., Pang, I.-H., Wax, M.B., Clark, A.F., 2005. Noninvasive Measurement of Rodent Intraocular Pressure with a Rebound Tonometer. Investigative Ophthalmology & Visual Science 46, 4617-4621.

Wang, X., Gregory-Evans, K., Wasan, K.M., Sivak, O., Shan, X., Gregory-Evans, C.Y., 2017. Efficacy of Post-natal In Vivo Nonsense Suppression Therapy in a Pax6 Mouse Model of Aniridia. Mol Ther Nucleic Acids 7, 417-428.

Warren, N., Caric, D., Pratt, T., Clausen, J.A., Asavaritikrai, P., Mason, J.O., Hill, R.E., Price, D.J., 1999. The transcription factor, Pax6, is required for cell proliferation and differentiation in the developing cerebral cortex. Cereb Cortex 9, 627-635.

Wawrocka, A., Krawczynski, M.R., 2018. The genetics of aniridia - simple things become complicated. J Appl Genet 59, 151-159.

Weber, A.J., Chen, H., Hubbard, W.C., Kaufman, P.L., 2000. Experimental glaucoma and cell size, density, and number in the primate lateral geniculate nucleus. Invest Ophthalmol Vis Sci 41, 1370-1379.

Welch, E.M., Barton, E.R., Zhuo, J., Tomizawa, Y., Friesen, W.J., Trifillis, P., Paushkin, S., Patel, M., Trotta, C.R., Hwang, S., Wilde, R.G., Karp, G., Takasugi, J., Chen, G., Jones, S., Ren, H., Moon, Y.C., Corson, D., Turpoff, A.A., Campbell, J.A., Conn, M.M., Khan, A., Almstead, N.G., Hedrick, J., Mollin, A., Risher, N., Weetall, M., Yeh, S., Branstrom, A.A., Colacino, J.M., Babiak, J., Ju, W.D., Hirawat, S., Northcutt, V.J., Miller, L.L., Spatrick, P., He, F., Kawana, M., Feng, H., Jacobson, A., Peltz, S.W., Sweeney, H.L., 2007. PTC124 targets genetic disorders caused by nonsense mutations. Nature 447, 87-91.

Whitson, J.T., Liang, C., Godfrey, D.G., Petroll, W.M., Cavanagh, H.D., Patel, D., Fellman, R.L., Starita, R.J., 2005. Central corneal thickness in patients with congenital aniridia. Eye Contact Lens 31, 221-224.

Wu, L., Ma, Q., Chen, Y., Wu, D.Z., Luo, T., 1991. Abnormalities of ERG in congenital aniridia. Yan Ke Xue Bao 7, 151-152, 119.

Wu, S.M., 2010. Synaptic organization of the vertebrate retina: general principles and species-specific variations: the Friedenwald lecture. Invest Ophthalmol Vis Sci 51, 1263-1274.

Yasue, A., Kono, H., Habuta, M., Bando, T., Sato, K., Inoue, J., Oyadomari, S., Noji, S., Tanaka, E., Ohuchi, H., 2017. Relationship between somatic mosaicism of Pax6 mutation and variable developmental eye abnormalities-an analysis of CRISPR genome-edited mouse embryos. Sci Rep 7, 53.

Yasuhara, O., Tooyama, I., Aimi, Y., Bellier, J.P., Hisano, T., Matsuo, A., Park, M., Kimura, H., 2003. Demonstration of cholinergic ganglion cells in rat retina: expression of an alternative splice variant of choline acetyltransferase. J Neurosci 23, 2872-2881.

Yeritsyan, N., Lehmann, K., Puk, O., Graw, J., Löwel, S., 2012. Visual capabilities and cortical maps in BALB/c mice. Eur J Neurosci 36, 2801-2811.

Yi, J., Puyang, Z., Feng, L., Duan, L., Liang, P., Backman, V., Liu, X., Zhang, H.F., 2016. Optical Detection of Early Damage in Retinal Ganglion Cells in a Mouse Model of Partial Optic Nerve Crush Injury. Invest Ophthalmol Vis Sci 57, 5665-5671.

Yogarajah, M., Matarin, M., Vollmar, C., Thompson, P.J., Duncan, J.S., Symms, M., Moore, A.T., Liu, J., Thom, M., van Heyningen, V., Sisodiya, S.M., 2016. PAX6, brain structure and function in human adults: advanced MRI in aniridia. Annals of Clinical and Translational Neurology 3, 314-330.

Yokoi, T., Nishina, S., Fukami, M., Ogata, T., Hosono, K., Hotta, Y., Azuma, N., 2016. Genotype-phenotype correlation of PAX6 gene mutations in aniridia. Hum Genome Var 3, 15052-15052.

Zakrzewska, A., Wiącek, M.P., Machalińska, A., 2019. Impact of corneal parameters on intraocular pressure measurements in different tonometry methods. Int J Ophthalmol 12, 1853-1858.

Zeng, H.-y., Zhu, X.-a., Zhang, C., Yang, L.-P., Wu, L.-m., Tso, M.O.M., 2005. Identification of Sequential Events and Factors Associated with Microglial Activation, Migration, and Cytotoxicity in Retinal Degeneration in rd Mice. Investigative Ophthalmology & Visual Science 46, 2992-2999.